The University of Nottingham
School of Physics & Astronomy

INVESTIGATION OF DEEP LEVEL DEFECTS IN ADVANCED SEMICONDUCTOR MATERIALS AND DEVICES

by

NOOR ALHUDA AHMED AL SAQRI

M. Sc (Physics)

Thesis submitted to the University of Nottingham

for the degree of Doctor of Philosophy

August 2016

ABSTRACT

This thesis reports an investigation of deep level defects in narrow bandgap semiconductors, namely GaAs and GaAsN, and wide-gap GaN materials and devices that have potential applications in photovoltaics and betavoltaic microbatteries. Indeed, for such applications it is of paramount importance to determine the characteristics of the defects present in the materials, which will help understand their effects on the quality of the materials and the performance of devices. In particular, the investigation is done on: (i) a set of GaAs (311)A solar cell structures gown by molecular beam epitaxy (MBE); (ii) dilute GaAsN epitaxial layers containing different nitrogen concentrations grown by MBE; and (iii) betavoltaic microbattery based on a GaN p–i–n homojunction structures grown by metal-organic vapour phase epitaxy (MOVPE) technique using current-voltage (I-V), capacitance-voltage (C-V), deep level transient spectroscopy (DLTS), and Laplace DLTS measurements.

The results of this study show that the defects affected significantly the electrical properties of different advanced semiconductor structures and devices. In particular, InGaAs Quantum Wires (QWr) Intermediate Band Solar Cells based nanostructures grown by MBE were studied. The DLTS and Laplace DLTS results showed that the efficiency measurements and external quantum efficiency (EQE) at different temperatures correlated with the appearance of defect peaks in QWr devices in the same temperature ranges. Additionally, this thesis reports the effect of a high dose of gamma (γ-) irradiation on MBE grown dilute GaAsN epilayers with nitrogen concentrations ranging from 0.2 to 1.2% with post-irradiation stability. The DLTS measurements revealed that after irradiation the number of

traps either decreased, remained constant, or new traps are created depending on the concentration of nitrogen. Moreover, this thesis reports the effect of beta particle irradiation on the electrical properties of a betavoltaic microbattery based on a GaN p–i–n homojunction with 200 nm and 600 nm thicknesses of undoped layer (i-GaN). The experimental studies demonstrate that, only the sample with thinner i-GaN layer shows the creation of new shallow donor traps upon irradiation on the p-side of the p-i-n junction. While the sample with thicker i-GaN is more resistant to irradiation.

PUBLICATIONS

1. Investigation of Electrically Active Defects in InGaAs Quantum Wires Intermediate-Band Solar Cells Using Deep Level Transient Spectroscopy (DLTS) Technique.
   Noor alhuda Al Saqri, Jorlandio F. Felix, Mohsin Aziz, Vasyl P. Kunets, Dler Jameel, David Taylor, Mohamed Henini, Mahmmoud S. Abd El-sadek, Colin. Furrow, Morgan E. Ware, Mourad Benamara, Mansour Mortazavi, Gregory Salamo
   Accepted for publication in Nanotechnology (2016)

2. Electrical performance of conducting polymer (SPAN) grown on GaAs with different substrate orientations.
   DA Jameel, M Aziz, JF Felix, **N Al Saqri**, D Taylor, H Albalawi, H Alghamdi, F Al Mashary, M Henini
   Applied Surface Science 387, 228 (2016)

3. Effect of ^{60}Co γ-ray irradiation on electrical properties of Ti/Au/$GaAs_{1-x}N_x$ Schottky diodes.
   A Teffahi, D Hamri, A Mostefa, A Saidane, **N Al Saqri**, JF Felix, M Henini
   Current Applied Physics 16 (8), 850 (2016)

4. Rapid thermal annealing: An efficient method to improve the electrical properties of tellurium compensated Interfacial Misfit GaSb/GaAs heterostructures.
   Mohsin Aziz, Jorlandio F Felix, Dler Jameel, **Noor Al Saqri**, Faisal S Al Mashary, Haifaa M Alghamdi, Hind MA Albalawi, David Taylor, Mohamed Henini
   Superlattices and Microstructures 88, 80 (2015)

5. Analysis of Deep Level Defects in GaN p-i-n Diodes after Beta Particle Irradiation.
   Sofiane Belahsene, **Noor Al Saqri**, Dler Jameel, Abdelmadjid Mesli, Anthony Martinez, Jacques de Sanoit, Abdallah Ougazzaden, Jean Paul Salvestrini, Abderrahim Ramdane, Mohamed Henini
   Electronics 4 (4), 1090 (2015)

6. Electrical Behavior of MBE Grown Interfacial Misfit GaSb/GaAs Heterostructures With and Without Te-Doped Interfaces.
   Mohsin Aziz, Jorlandio Francisco Felix, **Noor Al Saqri**, Dler Jameel, Faisal Saleh Al Mashary, Hind Mohammed Albalawi, Haifaa Mohammed Abdullah Alghamdi, David Taylor, Mohamed Henini

IEEE Transactions on Electron Devices 62 (12), 3980 (2015)

7. High-performance organic/inorganic hybrid heterojunction based on Gallium Arsenide (GaAs) substrates and a conjugated polymer.
   DA Jameel, JF Felix, M Aziz, **N Al Saqri**, D Taylor, WM de Azevedo, EF da Silva, H Albalawi, H Alghamdi, F Al Mashary, M Henini
   Applied Surface Science 357, 2189 (2015)

8. Investigation of the effects of gamma radiation on the electrical properties of dilute $GaAs_{1-x}N_x$ layers grown by Molecular Beam Epitaxy
   N Al Saqri, JF Felix, M Aziz, D Jameel, CIL de Araujo, H Albalawi, F Al Mashary, H Alghamdi, D Taylor, M Henini
   Current Applied Physics 15 (10), 1230 (2015)

9. Modeling the effect of deep traps on the capacitance–voltage characteristics of p-type Si-doped GaAs Schottky diodes grown on high index GaAs substrates.
   Nouredine Sengouga, Rami Boumaraf, Riaz H Mari, Afak Meftah, Dler Jameel, **Noor Al Saqri**, Mohsin Azziz, David Taylor, Mohamed Henini
   Materials Science in Semiconductor Processing 36, 156 (2015)

10. Effect of Post Growth Annealing Treatment on Interfacial Misfit GaSb/GaAs Heterostructures.
    M. Aziz, A. Mesli, J. F. Felix, D. Jameel, **N. Al Saqri**, D. Taylor, and M. Henini
    Journal of Crystal Growth 424, 5 (2015)

11. Deep Traps and Temperature Effects on the Capacitance of p-type Si-Doped GaAs Schottky Diodes on (211) and (311) Oriented GaAs Substrates.
    R. Boumaraf, N. Sengouga, R. Mari, A. Meftah, M. Aziz, D. Jameel, **N. Al Saqri**, D. Taylor, and M. Henini
    Superlattices and Microstructures 65, 319 (2014)

12. Deep-Level Transient Spectroscopy of Interfacial States in “Buffer-Free” Pin GaSb/GaAs Devices.
    M. Aziz, P. Ferrandis, A. Mesli, R. H. Mari, J. F. Felix, A. Sellai, D. Jameel, **N. Al Saqri**, A. Khatab D. Taylor, and M. Henini.
    Journal of Applied Physics 114 (13), 134507 (2013)

CONFERENCE PRESENTATIONS

ORAL TALKS

- "Deep Level Transient Spectroscopy of InGaAs Quantum Wire Intermediate-Band Solar Cells"
  3rd International Congress on Energy Efficiency and Energy Related Materials (ENEFM), Oludeniz, Fethiye/Mugla, Turkey, 19-23 October, (2015)

- "The Effect of the Deep Levels in the Efficiency of the Doped and Un-doped InGaAs Quantum Wire Intermediate Band Solar Cells"
  Nanostructure Materials for Photovoltaic Applications Workshop (NMPA-2015), SVU, Qena, Egypt, 21-26 November, (2015)

- "Influence of Deep Levels on the Efficiency of InGaAs Quantum Wire Intermediate-Band Solar Cells"
  The International Conference on Renewable Energy (INCORE2016) in celebration of the 5th anniversary of ANSOLE, Cairo, Egypt, 3-6 February, (2016)

- "Investigation of Deep Level Defects in GaN p-i-n Diodes After Beta Particle Irradiation Grown by Metal Organic Vapour Phase Epitaxy"
  The 40th WOCSDICE - Workshop on Compound Semiconductor Devices and Integrated Circuits held in Europe & 13th EXMATEC - Expert Evaluation and Control of Compound Semiconductor Materials and Technologies, Aveiro, Portugal, 6 -10 June, (2016)

- "Effect of Beta Particle Irradiation on Deep Level Defects in GaN p-i-n Diodes"
  Nano-semiconductors for Optoelectronics and Solar Cell Devices Workshop, Nottingham, UK, September, (2016)

POSTER PRESENTATIONS

- "Deep level Transient Spectroscopy (DLTS) Characterisation of Defects in AlGaN/Si Dual-band (UV/IR) Detectors Grown by MBE"
  The 17th European Molecular Beam Epitaxy Workshop, Levi, Finland, 10-13 March, (2013)

- "Electrical characterization of defects in InGaAs quantum wires intermediate-band solar cells using Deep Level Transient Spectroscopy (DLTS) technique"

15th International Conference on Defects Recognition, Imaging and Physics in Semiconductors, Warsaw, Poland, 15-19 September, (2013)

- "Effect of Gamma Irradiation on Deep Levels Detected by DLTS in $GaAs_xN_{1-x}$ with Different Nitrogen Concentration"
  Novel Gain Materials and Devices Based on III-V-N/Bi Compounds, Istanbul, Turkey 24-26 September, (2013)

- "Effect of Gamma Irradiation on Optical Properties in $GaAs_xN_{1-x}$ with Different Nitrogen Concentration"
  International Workshop on Materials Science & Modelling, Dubai, U.A.E, 25-29 May, (2014).

- "Investigation of Electrically Active Defects in InGaAs Quantum Wire Intermediate-Band Solar Cells"
  The 17th International Conference on Extended Defects in Semiconductors, Gottingen, Germany, 14-19 September, (2014)

- "Investigation of the effect of gamma irradiation on deep levels in $GaAs_xN_{1-x}$ with different nitrogen concentration using DLTS"
  28th International Conference on Defects in Semiconductors, Warsaw, Poland, 27 – 31 July, (2015)

- "Investigation of the effect of indium doping on the electrical and optical properties of TiO_2 thin films"
  The International Conference on Extended Defects in Semiconductors, Les Issambres, France, 25-29 September, (2016)

ACKNOWLEDGEMENTS

First of all, I would like to thank Allah Almighty for giving me the strength, knowledge, and for blessing me with the ability to proceed with this thesis and to persevere and complete it satisfactorily.

It is my great pleasure to thank those who made this thesis possible.

I owe my deepest gratitude and thanks to my supervisor, Prof. **M. Henini**, for his tremendous support, encouragements, patience, and guidance that enabled me to go forward during my research. Also I am extremely grateful to him for giving me numerous opportunities during my PhD including attendance at international conferences where I presented my work and explored collaborations independently and confidently with many groups around the world.

I would like to acknowledge the financial support which was provided by **Sultan Qaboos University**, Oman for my PhD studies.

I would like to thank all my collaborators; Drs **V. P. Kunets** (University of Arkansas, USA), **J. F. Felix** (University of Brasilia, Brazil), and **S. Belahsene** (National Centre for Scientific Research, France) for providing me with samples investigated in this thesis and useful discussions; Prof. **A. Mesli** (Aix-Marseille University, France) for his helpful support to learn DLTS technique; and all other collaborators named in the publications list.

I am grateful to Mr **D. Taylor** for his help in processing the devices investigated here. Also I would like to thank all my colleagues for their support and friendship.

I would like to thank all my friends and family for providing me infinite support, patience and understanding throughout my research. Without the love and care I was given, I would not have the ability to succeed. I cannot thank you enough for

always believing in my ability to succeed and encouraging me throughout this experience.

Finally, I wish to express my gratitude to each and every one who contributed in this thesis even with simple suggestions and advice.

TABLE OF CONTENTS

CHAPTER 1: INTRODUCTION ... 1
1.1 INTRODUCTION ... 1
1.2 MOTIVATION ... 4
1.3 SCHEME OF THE THESIS ... 5
REFERENCES ... 7
CHAPTER 2: FUNDAMENTAL CONCEPTS OF SEMICONDUCTORS ... 9
2.1 SEMICONDUCTORS ... 9
2.1.1 UNDOPED AND DOPED SEMICONDUCTORS ... 10
2.2 CRYSTAL STRUCTURES AND PROPERTIES ... 11
2.2.1 CRYSTAL STRUCTUREs ... 11
2.2.2 ENERGY BANDGAPS ... 15
2.2.3 DIRECT AND INDIRECT ENERGY BANDGAPS ... 16
2.2.4 TEMPERATURE DEPENDENT ENERGY BANDGAPS ... 17
2.2.5 QUANTUM CONFINEMENT ... 17
2.2.6 DENSITY OF STATES ... 19
2.3 HETEROJUNCTION STRUCTURES ... 21
2.3.1 LATTICE MISMATCH ... 22
2.3.2 ATOM SIZE AND ELECTRONEGATIVITY ... 23
2.3.3 BAND ALIGNMENTS ... 24
2.4. GENERAL PROPERTIES OF SELECTED SEMICONDUCTOR MATERIALS ... 26
2.4.1. GaAs ... 26
2.4.2. DILUTE GaAsN ... 28
2.4.2.1. THE BAND ANTICROSSING (BAC) MODEL ... 29
2.4.2.2. SOME IMPORTANT PROPERTIES OF GaAsN ... 31
2.4.3. GaN ... 31
REFERENCES ... 33
CHAPTER 3: SEMICONDUCTOR DEFECTS AND THEIR PROPERTIES ... 36
3.1 CLASSIFICATION OF DEFECTS ... 36
3.1.1 POINT DEFECTS ... 36
3.1.2 COMPLEXES OF POINT DEFECTS ... 37

3.1.3 LINEAR DEFECTS 39
3.2 DEFECTS AND THEIR CARRIER KINETICS 40
3.2.1 SHALLOW LEVELS AND DEEP LEVELS DEFECTS 40
3.2.2 SHOCLEY-READ-HALL THEORY 42
3.3 DEFECTS IN COMPOUND SEMICONDUCTORS 47
3.3.1 DEFECTS IN GaAs 47
3.3.2 DEFECTS IN DILUTES GaAsN 48
3.3.3 DEFECTS IN GaN 51
REFERENCES 53
CHAPTER 4: EXPERIMENTAL TECHNIQUES 57
4.1 P-N JUNCTION 57
4.1.1 P-N JUNCTION UNDER BIAS CONDITIONS 64
4.1.2 DEPLETION LAYER CAPACITANCE 66
4.2 CURRENT- VOLTAGE CHARACTERISATION 67
4.3 DEEP LEVEL TRANSIENT SPECTROSCOPY (DLTS) 69
4.3.1 CAPACITANCE TRANSIENTS 69
4.3.2 CONVENTIONAL DLTS 73
4.4 LAPLACE DLTS SPECTROSCOPY 76
4.5 SYSTEM HARDWARE IMPLEMENTATION 79
4.5.1 DESCRIPTION OF SYSTEM HARDWARE 79
4.5.1.1 CRYOSTAT AND TEMPERATURE CONTROLLER 80
4.5.1.2 CAPACITANCE METER 81
4.5.1.3 CURRENT-VOLTAGE SOURCE METER 82
4.5.1.4 DATA ACQUISITION AND BNC-2100 CONNECTOR 82
4.5.1.5 COMPUTER INTERFACE 82
4.6 SYSTEM SOFTWARE 82
4.6.1 CONVENTIONAL DLTS MEASUREMENTS MODE 83
4.6.2 LAPLACE TRANSIENT PROCESSING MODE 84
4.7. PHOTOVOLTAIC CELL AND BETAVOLTIC BATTERY 84
REFERENCES 87
CHAPTER 5: EXPERIMENTAL DETAILS 89
5.1 SAMPLES USED IN THIS STUDY 89
5.2 MEASUREMENT DETAILS 90
5.2.1 I-V MEASUREMENTS 90

5.2.2 C-V MEASUREMENTS 90
5.2.3 DLTS MEASUREMENTS 91
5.2.4 LAPLACE DLTS MEASUREMENTS 91
CHAPTER 6: INVESTIGATION OF ELECTRICALLY ACTIVE DEFECTS IN InGaAs QUANTUM WIRES INTERMEDIATE BAND SOLAR CELLS USING DEEP LEVEL TRANSIENT SPECTROSCOPY (DLTS) TECHNIQUE 92
6.1 INTRODUCTION 92
6.2 SAMPLE DETAILS 96
6.3 RESULTS AND DISCUSSION 99
6.3.1 INVESTIGATION OF THE CURRENT DENSITY (J) – VOLTAGE (V) CHARACTERISTICS AS FUNCTION OF TEMPERATURE 99
6.3.2 C-V CHARACTERISTICS 108
6.3.3 DLTS AND LAPLACE DLTS CHARACTERISTICS 115
6.4 CONCLUSION 123
REFERENCES 125
CHAPTER 7: INVESTIGATION OF THE EFFECTS OF GAMMA RADIATION ON THE ELECTRICAL PROPERTIES OF DILUTE $GaAs_{1-x}N_x$ LAYERS GROWN BY MOLECULAR BEAM EPITAXY 130
7.1 INTRODUCTION 130
7.2 SAMPLE DETAILS 132
7.3 RESULTS AND DISCUSSION 133
7.3.1 I-V CHARACTERISTICS 133
7.3.2 C-V CHARACTERISTICS 146
7.3.3 DLTS AND LAPLACE DLTS CHARACTERISTICS 149
7.4 CONCLUSION 158
REFERENCES 160
CHAPTER 8: ANALYSIS OF DEEP LEVEL DEFECTS IN GaN P-I-N DIODES AFTER BETA PARTICLE IRRADIATION GROWN BY METAL ORGANIC VAPOUR PHASE EPITAXY 165
8.1 INTRODUCTION 165
8.2 SAMPLE DETAILS 168
8.3 RESULTS AND DISCUSSION 170
8.3.1 I-V MEASUREMENTS 170
8.3.2 C-V MEASUREMENTS 174
8.3.3 DLTS CHARACTERISTICS 177

8.4 CONCLUSION..184
REFERENCES 185
CHAPTER 9: CONCLUSION AND FUTURE WORK 188
9.1 CONCLUSION..188
9.2 FUTURE WORK SUGGESTIONS 189
REFERENCES 191

CHAPTER 1: INTRODUCTION

1.1 INTRODUCTION

After the invention of the transistor, a revolution in semiconductor materials followed. This revolution has dramatically changed the electronics and optoelectronic industries.

Gallium arsenide (GaAs), a III–V compound semiconductor, has versatile properties which have made it a strong potential candidate for semiconductor-based technology. For example, this compound has a direct bandgap of 1.42 eV at room temperature with a direct bandgap nature and high carrier mobility which are prerequisites for a wide range of applications in the sector of optoelectronic and photovoltaic devices. For example, single and multi-junction solar cells [1] using GaAs semiconductor material have achieved record efficiencies of ~40%. For space applications, it has become very important to enhance further the performance of GaAs-based solar cells. One approach is to use semiconductor nanostructures, such as In(Ga)As Quantum dots (QDs) and quantum wires (QWRs), to implement what are called GaAs-based intermediate band solar cells (IBSC) [2-4] in order to enhance the solar efficiency. The main principle of these cells is to introduce one or more electronic bands (called intermediate bands or levels) inside the main bandgap of a conventional semiconductor. In this case, these nanostructures introduce additional energy bands that allow more absorptions, which in turn cause an increase of the short circuit current. However, it is found that for example the incorporation of QDs causes a reduction of the photoelectrical conversion efficiency of QD IBSC as a result of the formation of strain and resulting dislocations which lead to the deterioration of the open-circuit voltage,

V_{oc} [5-7]. Fig. 1.1 shows the bandgaps of the most common semiconductors with their lattice constants.

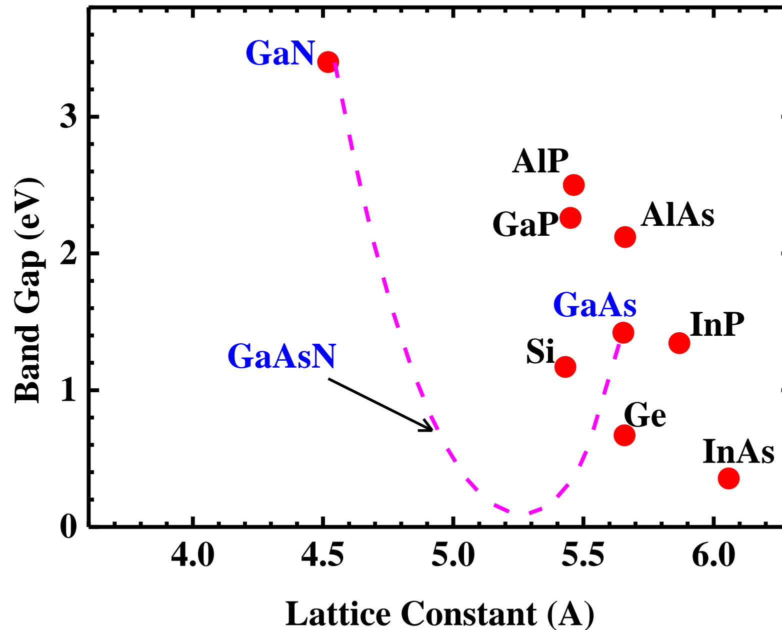

Fig. 1.1. Bandgaps of selected semiconductors as a function of lattice constant. The dashed line represents the effect of adding N into GaAs.

Another property of GaAs is that the bandgap energy of this material can be tuned by introducing a small fraction of nitrogen. This leads to the formation of dilute nitride GaAsN, a ternary III-V compound semiconductor. In particular, Kondow *et al.* [8] have found that when a small amount of nitrogen (N <4%) was incorporated into GaAs, dilute nitride GaAsN showed a smaller bandgap than GaAs. The reduction was approximately 0.1 eV for each percent of N in the alloy. Fig. 1.1 shows schematically this enormous bandgap bowing where the dashed line represents the bandgap bowing due to incorporation of N into GaAs. Therefore, GaAsN is a promising material for a wide variety of optoelectronic applications,

such as long wavelength lasers, high-efficiency photovoltaic devices, and optical amplifiers [9].

Gallium nitride (GaN), is another type of a III–V compound semiconductor which has a wide bandgap of 3.4 eV. Due to its wide bandgap this compound is considered as a promising candidate for durable devices in extreme environmental conditions such as high temperatures and voltages [10], and therefore it is a good choice for high power applications. Hence, the GaN industry has embarked on its journey in the micro-electro-mechanical system (MEMS) technology which requires small size and higher energy density power supplies to drive these devices. In addition, these power supplies need to be insensitive to climate and temperature changes, and should have long life time for long-term applications. GaN betavoltaic microbattery, which uses β-radiation, is one type of nuclear microbatteries that is considered to be a promising technology to satisfy the above requirements of the MEMS power supplies [11].

One of the fascinating technologically useful features of semiconductors is the possibility of changing their electronic and photonic properties by introducing small amounts of impurities in them. This process is known as doping. However, in reality semiconductors possess a wide range of intrinsic and extrinsic defects [20]. Defects introduce deep levels in the bandgap of semiconductors and have detrimental effects on the performance of the devices since they act as efficient recombination centres. Thus, great research efforts have been put towards understanding, improving and controlling the perfection of semiconductor crystals. Deep level transient spectroscopy (DLTS) is one of the most powerful technique used for characterising and identifying deep levels defects. Specifically,

fundamental defect parameters such as activation energy, capture cross-section and average concentration can be obtained from DLTS measurements [21].

The study presented in this thesis relates to the characterization of a range of different semiconductor materials systems namely GaAs, GaAsN and GaN which can be used in different applications such as photovoltaic devices and betavoltaic microbattery. Indeed, for such applications it is of paramount importance to determine the characteristics of the defects present in the materials, which will help understand their effects on the quality of the materials and the performance of devices.

1.2 MOTIVATION

The electrically active defects play a tremendous role in electronic and optoelectronic devices. The main motivation of this thesis is to study the electrical active defects present in different semiconductors systems and devices, and investigate their effects on the electrical properties using current-voltage (I-V), capacitance- voltage (C-V), DLTS, and Laplace DLTS methods.

I-V, C-V, conventional DLTS and Laplace DLTS characterisation techniques are applied to study the electrically active defects in GaAs p-n junctions, GaAs p-i-n junctions, undoped GaAs p-i-n diodes with one dimensional InGaAs quantum wires, and n-type Si δ- doped GaAs p-i-n diodes with one dimensional InGaAs quantum wires solar cell structures in order to understand the physical phenomena that affect the conversion efficiency. Additionally, the same methods are used to investigate the effect of a high dose of γ-irradiation on post-irradiation stability of dilute GaAsN samples with nitrogen concentrations ranging from 0.2 to 1.2%. Moreover, I-V, C-V and DLTS are used to examine the radiation damage of β-

particles in GaN p–i–n homojunction structures with undoped intrinsic layers (i-GaN) having thicknesses of 200 nm and 600 nm and their effect in the creation of both shallow and deep energy level defects.

1.3 SCHEME OF THE THESIS

This thesis is organised as follows:

Chapter 1 covers the research motivations and structure of the thesis.

Chapter 2 describes the fundamental concepts of semiconductors, crystal structure, the principles of heterostructure devices and quantum confinement. The properties of GaAs, GaAsN and GaN materials are covered in this chapter.

Chapter 3 gives information on the crystal defects and theoretical background of carrier kinetics.

Chapter 4 describes the experimental techniques used in this thesis including DLTS, Laplace DLTS, and solar cell and betavoltaic battery efficiencies. The hardware and software required to implement these methods are also presented.

Chapter 5 lists the samples used in this thesis and presents briefly the details of the measurements set up.

Chapter 6 discusses the effect of electrically active defects on the electrical properties of a set of GaAs (311)A solar cell structures grown by Molecular Beam Epitaxy (MBE) using I-V, C-V, DLTS and Laplace DLTS measurements.

Chapter 7 presents the effect of gamma (γ-) irradiation on the electrical properties of dilute GaAsN epilayers having nitrogen concentrations ranging from 0.2 to 1.2%.

Chapter 8 describes the effect of beta particles irradiation on the electrical properties of betavoltaic microbattery based on a GaN p–i–n homojunction

structure with the undoped layer (i-GaN) having thicknesses of 200 nm and 600 nm.

Chapter 9 gives an overall summary of the research work carried out in this thesis and offer suggestions for future work.

REFERENCES

[1] N. Ekins-Daukes, K. Barnham, J. Connolly, J. Roberts, J. Clark, G. Hill and M. Mazzer, Applied Physics Letters **75** (26), 4195 (1999).

[2] A. Luque and A. Martí, Physical Review Letters **78** (26), 5014 (1997).

[3] V. Kunets, C. Furrow, T. A. Morgan, Y. Hirono, M. Ware, V. Dorogan, Y. I. Mazur, V. Kunets and G. Salamo, Applied Physics Letters **101** (4), 041106 (2012).

[4] V. P. Kunets, C. Furrow, M. Ware, L. de Souza, M. Benamara, M. Mortazavi and G. Salamo, Journal of Applied Physics **116** (8), 083102 (2014).

[5] A. Luque and A. Martí, Advanced Materials **22** (2), 160 (2010).

[6] X. Shang, J. He, H. Wang, M. Li, Y. Zhu, Z. Niu and Y. Fu, Applied Physics A **103** (2), 335 (2011).

[7] A. Marti, N. Lopez, E. Antolin, E. Canovas, A. Luque, C. Stanley, C. Farmer and P. Diaz, Applied Physics Letters **90** (23), 233510 (2007).

[8] M. Kondow, K. Uomi, K. Hosomi and T. Mozume, Japanese Journal of Applied Physics **33** (8A), L1056 (1994).

[9] M. Shafi, R. Mari, M. Henini, D. Taylor and M. Hopkinson, physica status solidi (c) **6** (12), 2652 (2009).

[10] M. Trivedi and K. Shenai, Journal of Applied Physics **85** (9), 6889 (1999).

[11] Z. Cheng, Z. Zhao, H. San and X. Chen, presented at the Nano/Micro Engineered and Molecular Systems (NEMS), 2011 IEEE International Conference on IEEE, 1036, (2011).

[12] M. Ni, M. K. Leung, D. Y. Leung and K. Sumathy, Renewable and Sustainable Energy Reviews **11** (3), 401 (2007).

[13] Y. Xie, L. Wei, Q. Li, Y. Chen, S. Yan, J. Jiao, G. Liu and L. Mei, Nanotechnology **25** (7), 075202 (2014).

[14] A. Fujishima, Nature **238**, 37 (1972).

[15] Z. Li, D. Ding, Q. Liu, C. Ning and X. Wang, Nanoscale research letters **9** (1), 1 (2014).

[16] X. Li, S. Wu, P. Hu, X. Xing, Y. Liu, Y. Yu, M. Yang, J. Lu, S. Li and W. Liu, Journal of Applied Physics **106** (4), 043913 (2009).

[17] A. Ruiz, A. Cornet, G. Sakai, K. Shimanoe, J. Morante and N. Yamazoe, Chemistry letters (9), 892 (2002).

[18] X. Han and G. Shao, Physical Chemistry Chemical Physics **15** (24), 9581 (2013).

[19] J. Nowotny, A. Malik, M. A. Alim, T. Bak and A. J. Atanacio, ECS Journal of Solid State Science and Technology **3** (10), 330 (2014).

[20] P. Blood and J. W. Orton, Reports on Progress in Physics **41** (2), 157 (1978).

[21] D. Lang, Journal of Applied Physics **45** (7), 3023 (1974).

CHAPTER 2: FUNDAMENTAL CONCEPTS OF SEMICONDUCTORS

The fundamental properties of semiconductors are described in this chapter including crystal structures, energy gaps, direct and indirect energy gaps, temperature dependent energy gaps, quantum confinement and density of states. Heterostructures and their properties such as lattice mismatch, atom size and electronegativity and band alignment are also discussed. Some general properties of GaAs, dilutes GaAsN, and GaN are also presented.

2.1 SEMICONDUCTORS

During recent decades, semiconductors have become the heart of modern electronics and optoelectronics because they essentially serve as the basic building materials used to construct numerous electronic components in electrical and optical devices [1]. Good examples of these devices are computers (memories, CPUs), optical storage media (lasers for CDs and DVDs), communication infrastructure (laser and photo-detectors for optical-fiber technology), high efficiency solar cells , displays (thin film transistors, LEDs), projection (laser diodes), general lighting (LEDs) [2] etc. On the whole, semiconductor materials continue to be an attractive topic for fundamental research.

A semiconductor is a material whose electrical conductivity lies in between that of an insulator and a good conductor. It is normally defined as the material that has an electrical resistivity in the range of 10^{-2} to 10^{9} Ω.cm. Semiconductors are classified into elementary and compound semiconductors. An elementary semiconductor is made of only one element such as Si and Ge which belong to group IV elements of

the periodic table, while compound semiconductors are made of two or more than two elements from the periodic table such as elements from the groups III and V, and II and VI. Compound semiconductors which are made by two elements are known as binary compounds. A good example of these are GaAs and GaN. Those which have three elements are known as ternary compounds such as InGaAs and GaAsN.

2.1.1 UNDOPED AND DOPED SEMICONDUCTORS

Semiconductor materials also can be classified based on their type of doping. For example a pure semiconductor is known as an intrinsic or undoped semiconductor. This type of semiconductor is normally made of elemental (e.g. Si) or binary compound semiconductors (e.g. GaAs). Intrinsic semiconductors, which are considered to be very pure, have an insignificant amount of impurities that could affect their electrical properties. Alternatively, a pure semiconductor can also be defined as one in which the number of electrons in the conduction band is equal to the number of holes in the valence band. At zero absolute temperature, the intrinsic semiconductor behaves as an insulator because the valence band is completely filled and the conduction band is completely empty and hence there is no flow of free charge carriers to contribute to its conductivity. However, if a thermal or photo excitation is applied the conductivity of this type of semiconductor will increase.

In semiconductor materials the process of introducing small amounts of impurity atoms into a pure semiconductor is known as doping. When a semiconductor is doped with other atoms, it is called extrinsic or impurity semiconductor. In particular, when excess number of electrons are introduced by the dopant atoms, these create an n-type semiconductor. For example, in n-type doping process, a

pentavalent impurity material (group V in the periodic table) like As is added to pure Si. Si has four electrons in its outer electronic shell while As has five electrons. As a result of this, four electrons in As form bonds with the surrounding silicon atoms leaving one electron free for n type conduction. Similarly, when a trivalent impurity material (group III in the periodic table) like boron is added to a pure Si, the three valence electrons of boron atom form covalent bonds with four surrounding Si atoms leaving one hole free for p type conduction. When the dopant atoms produce an excess number of holes they create a p-type semiconductor.

2.2 CRYSTAL STRUCTURES AND PROPERTIES

The crystal structure plays an important role in the performance of semiconductor devices. In these materials the crystal structure depends on the arrangement of the atoms in the crystals.

2.2.1 CRYSTAL STRUCTUREs

The ideal crystal structure is composed of a unit cell, which includes a set of atoms arranged in an infinite periodically repetitive arrangement. Crystal structures can be found in different forms. Fig. 2.1 shows some examples of these structures, namely, simple cubic (sc), body-centred cubic (bcc), and face-centred cubic (fcc). The cubic lattice is the simplest crystal structure in which atoms are located at each corner of the cube (Fig. 2.1 (a)). The body centred cubic (bcc) lattice has atoms located at each corner of the cube and one atom at the centre of the cube as illustrated in Fig. 2.1 (b), while, as shown in Fig. 2.1 (c), in the face centred cubic lattice one atom is located at the centre of each face of the cube beside to the atoms located at each corner of the cube.

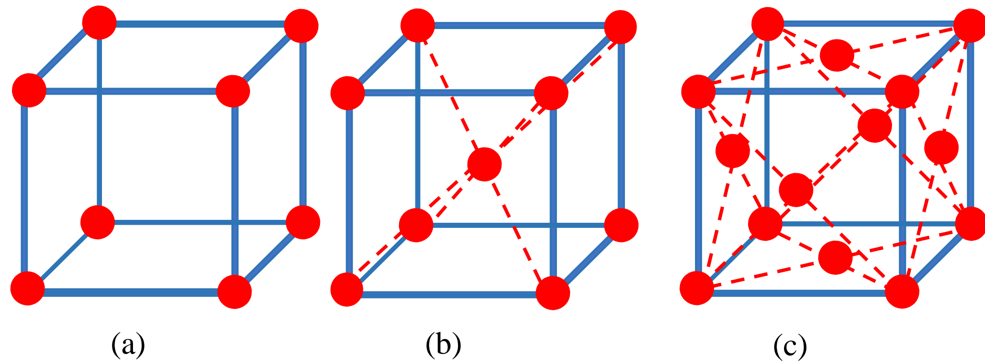

Fig. 2.1. Crystal structure of (a) simple cubic lattice (b) body centred cubic lattice and (c) face centred cubic lattice.

Diamond (Fig. 2.2 (a)) and zincblende structures (Fig. 2.2 (b)) are other most important crystal structure types in semiconductors. Each atom in these structures has covalent bonds with four neighbouring atoms of a regular tetrahedron and can be considered as two interpenetrating fcc lattices. All the sites in the diamond structure are occupied by the same kind of atoms. While the sites in the zincblende are occupied by two different types of atoms. Si, Ge and C elemental semiconductors are good examples of diamond structures, while GaAs, GaP, and InAs III-V compound semiconductors are good examples of zincblende structures.

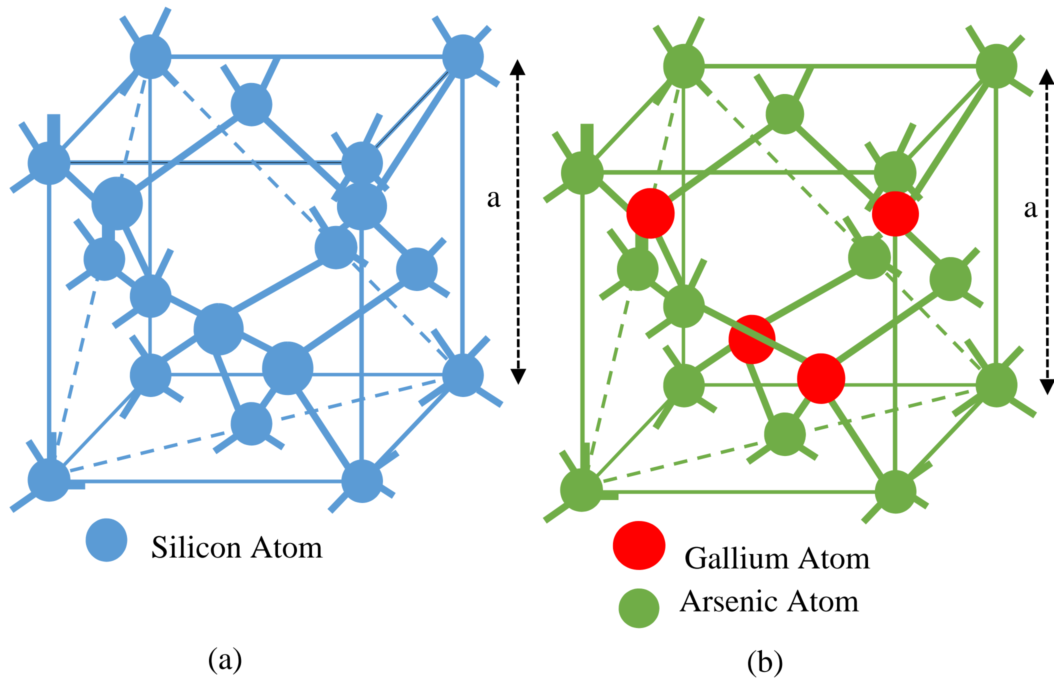

Fig. 2.2. Illustration of (a) diamond structure for Si where both types of atomic sites are occupied by Si and (b) zincblende structure for GaAs where the sites are occupied by Ga and As atoms, a is the lattice constant [3].

In order to fabricate semiconductor devices, information about the orientation of the semiconductor crystal and the properties of its surface are needed. Thus the Miller indices of a plane are generally used to get the information about the orientation of a semiconductor crystal. The Miller indices are determined by using three primitive basis vectors ***a***, ***b***, and ***c*** to describe the crystalline solid along the (**x**, **y**, **z**) directions. Fig. 2.3 illustrates an example of a plane with Miller indices (3, 2, 2).

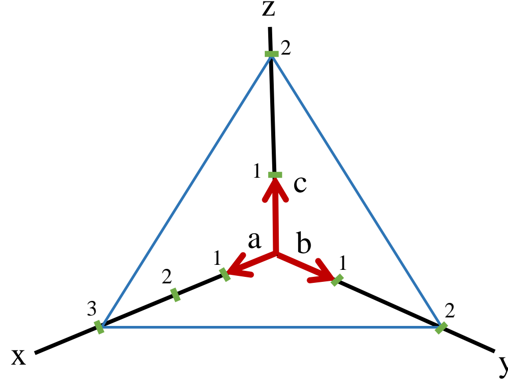

Fig. 2.3. Illustration of a plane having Miller indices (322).

For any choice of position vector $\boldsymbol{R}$, the crystal structure remains the same. Thus the translation vector $\boldsymbol{R}$ is defined as

$$\boldsymbol{R} = p\boldsymbol{a} + q\boldsymbol{b} + r\boldsymbol{c} \qquad (2.1)$$

where *p, q* and *r* are integers.

The relation between the reciprocal lattice basis vectors ($\boldsymbol{a}^*$, $\boldsymbol{b}^*$, and $\boldsymbol{c}^*$) and the primitive vectors ($\boldsymbol{a}, \boldsymbol{b},$ and $\boldsymbol{c}$) can be given as

$$\boldsymbol{a}^* = \boldsymbol{2\pi}\left[\frac{(\boldsymbol{b}\times\boldsymbol{c})}{\boldsymbol{a}.(\boldsymbol{b}\times\boldsymbol{c})}\right] \qquad (2.2)$$

$$\boldsymbol{b}^* = \boldsymbol{2\pi}\left[\frac{(\boldsymbol{a}\times\boldsymbol{c})}{\boldsymbol{a}.(\boldsymbol{b}\times\boldsymbol{c})}\right] \qquad (2.3)$$

$$\boldsymbol{c}^* = \boldsymbol{2\pi}\left[\frac{(\boldsymbol{a}\times\boldsymbol{b})}{\boldsymbol{a}.(\boldsymbol{b}\times\boldsymbol{c})}\right] \qquad (2.4)$$

where $\boldsymbol{a}^*.\boldsymbol{a} = 2\pi$ and $\boldsymbol{a}.\boldsymbol{b}^* = 0$ and so on.

The denominators in the above equations are the same because $\boldsymbol{a}.(\boldsymbol{b}\times\boldsymbol{c}) = \boldsymbol{b}.(\boldsymbol{c}\times\boldsymbol{a}) = \boldsymbol{c}.(\boldsymbol{a}\times\boldsymbol{b})$ and represent the volume enclosed by the vectors $(\boldsymbol{a}, \boldsymbol{b}, \boldsymbol{c})$.

The reciprocal lattice vector, **G** can be defined as

$$G = h\,\boldsymbol{a}^* + \boldsymbol{k}\,\boldsymbol{b}^* + l\,\boldsymbol{c}^* \qquad (2.5)$$

where *h, k, l* are integers.

The relationship between reciprocal lattice ($\boldsymbol{G}$) and direct lattice ($\boldsymbol{R}$) is given by

$$\boldsymbol{G} \cdot \boldsymbol{R} = 2\pi \times \text{integer} \qquad (2.6)$$

2.2.2 ENERGY BANDGAPS

In solid-state physics, the energy difference between the top of the valence band (VB) and the bottom of the conduction band (CB) is defined as the energy gap (E_g) or bandgap as illustrated in Fig. 2.4. Materials can be classified into three types depending on their energy gap, namely insulators, semiconductors and metals. In particular, E_g in metals is ~0 eV. While in semiconductors E_g is in the range ~0.17 eV (InSb) to ~ 6 eV (AlN) and in insulators E_g is very high (e.g. $E_g > \sim 6$ eV).

Fig. 2.4. Energy bands diagram of a semiconductor.

The band gap of a semiconductor is typically represented by the energy-wave vector (E-k) relationship as illustrated in Fig. 2.5. At k=0 the minima of conduction band and maxima of valence band have approximately parabolic shapes and their energy are given by

$$E_c = E_g + \frac{h^2 k^2}{8\pi^2 m_e^*}, E_v = -\frac{h^2 k^2}{8\pi^2 m_h^*} \qquad (2.7)$$

where E_c and E_v are the energy of conduction and valence bands, respectively. h, k, m_e^* and m_h^* are Plank's constant, Boltzmann constant, effective masses of electron and hole, respectively. At very low temperature (~0 K) the electrons in the valence band do not have enough energy to be excited to the conduction band and

thus they are confined in the valence band. As a result of this an intrinsic semiconductor behaves as an insulator at this low temperature.

2.2.3 DIRECT AND INDIRECT ENERGY BANDGAPS

In semiconductor physics, the band gap of a semiconductor can be classified into a direct band gap or an indirect band gap. This classification is based on the position of the top of the valence band and the bottom of the conduction band with respect to the wave vector (k). In a direct band gap semiconductor, the top of the valence band and the bottom of the conduction band take place at the same value of momentum, i.e. k=0. Whereas, in an indirect band gap semiconductor, these two bands take place at different values of momentum. GaAs and Si are the most common direct and indirect semiconductors, respectively. Fig. 2.5 illustrates the E (k) relationship of these two semiconductors.

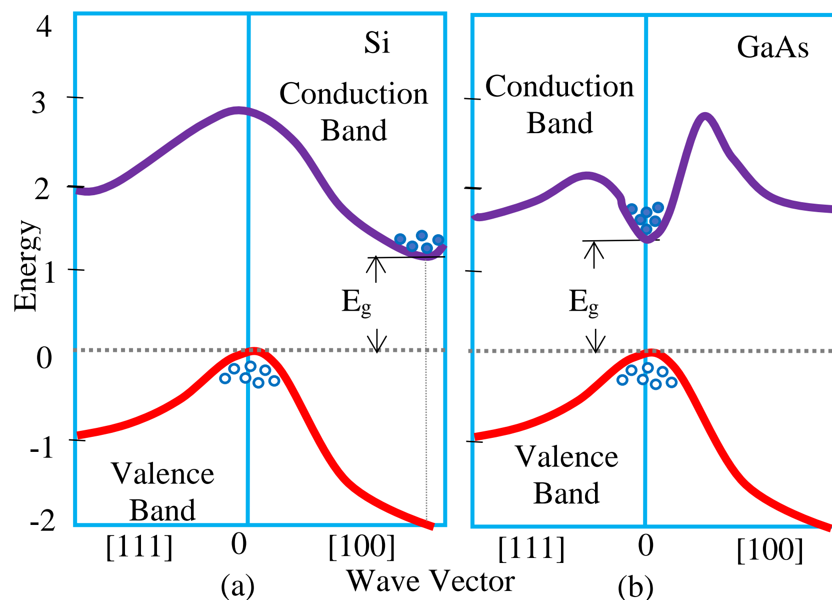

Fig. 2.5. Energy-band structures of (a) Si that has an indirect band gap and (b) GaAs that has a direct band gap [3]. The full and open circles represent electrons and holes, respectively.

2.2.4 TEMPERATURE DEPENDENT ENERGY BANDGAPS

In semiconductor materials, when the temperature increases, the energy bandgap decreases. In fact, when the temperature is increased, the thermal vibrational energy of the atoms and the amplitude of the atomic vibrations increase. Consequently, the interatomic spacing increases which leads to a reduction of the potential seen by electrons in the material. As a result of this the size of the energy gap is reduced.

The empirical relationship for the temperature dependence of energy band gap $E_g(T)$ was formulated by Varshni [4] and it is given by

$$E_g(T) = E_g(0) - \frac{\alpha T^2}{\beta} \qquad (2.8)$$

where $E_g(0)$ is the energy bandgap at 0 K, and α and β represent empirical parameters associated with the material. These empirical parameters are listed for GaAs, GaAsN with N=2.97% and GaN in Table 2.1.

Table 2.1. Empirical parameters for temperature dependency of GaAs, GaAsN and GaN bandgaps.

Parameter	GaAs [5]	GaAsN (N=2.97%) [6]	GaN [7]
α (meV/K)	0.5 meV/K	0.61	50.74
β (K)	220 K	560	600

2.2.5 QUANTUM CONFINEMENT

The nanostructured materials have unique optical and electronic properties compared to the bulk materials. In particular the variation of the size of the structure of these nano-systems makes their optical properties tunable. Hence, this allows the nanostructured materials to be used in many optoelectronic applications such as photovoltaic, LEDs, and lasers devices. These unusual properties of semiconductor

nanomaterials are due to the so-called quantum size effect or quantum confinement which occur when the size of the system is small in comparison with Bohr excitonic radius.

As illustrated in Fig. 2.7, semiconductor materials can be classified in terms of the material dimensions into four classes, namely, three-dimensional (3D) structure or bulk, two-dimensional (2D) structure or quantum well, one-dimensional structure (1D) or quantum wire and zero-dimensional structure (0D) or quantum dot. In particular, in bulk structure there is no quantisation of the particle motion, and therefore the particle is free to move in three dimensions. While in quantum well structure, quantisation of the particle motion occurs in one direction, while the particle is free to move in the other two directions. Thus, the continuous energy levels found in bulk material become discrete energy levels in these layers. On the other hand, in quantum wire structure, quantisation occurs in two directions, leading to free movement along only one direction. Moreover, in quantum dot structure, quantisation occurs in all three directions, i.e. the particle is confined in all three directions. Fig. 2.6 shows a typical diagram of quantum well which usually formed by growing a thin layer of a semiconductor material between two layers of another semiconductor material with a larger bandgap. An example of two materials that may be used to make a semiconductor quantum well is GaAs/AlGaAs where the quantum well is formed in the thin GaAs layer sandwiched between AlGaAs layers which have a larger band gap.

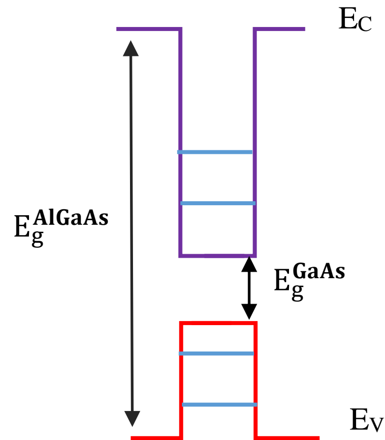

Fig. 2.6. A typical diagram of a single quantum well. The blue lines represent the allowed energy levels for an electron within the well.

2.2.6 DENSITY OF STATES

In order to determine the distribution of carriers in a semiconductor, the number of available states at each energy is an important to consider. Due to the close space between the atoms in solid materials, they interact with each other by means of their electric fields. Consequently this causes the energy levels to split into a finite number of electronic states [8].

Energy bands arise from their closely spaced sublevels as electrons tend to occupy all lower energy states available to them. As a result of this, two highest energy bands knowns as valence and conduction bands are created. During the conduction process the electrons are excited from the valence band to the conduction band of a semiconductor material. Consequently, this leads the creation of a local positive charge in the valence band known as a hole. The density of states (N(E)) of a semiconductor material is defined as the number of states at a certain energy level that are available to be occupied. N(E) depends on the confinement of charge carriers (e.g. electrons) and the degree of their freedom. The confinement of charge carriers depends on the material dimensions which facilitates the number of degrees

of freedom. N(E) in 3D systems has a square root dependence with energy as shown in Fig. 2.7(a), while in 2D systems N(E) has a step like function as a function of energy (Fig. 2.7(b)). On the other hand, N(E) is proportional to $(E)^{-1/2}$ in 1D systems and its independent of (delta function) energy in 0D systems as illustrated in Fig. 2.7(c) and Fig. 2.7(d), respectively.

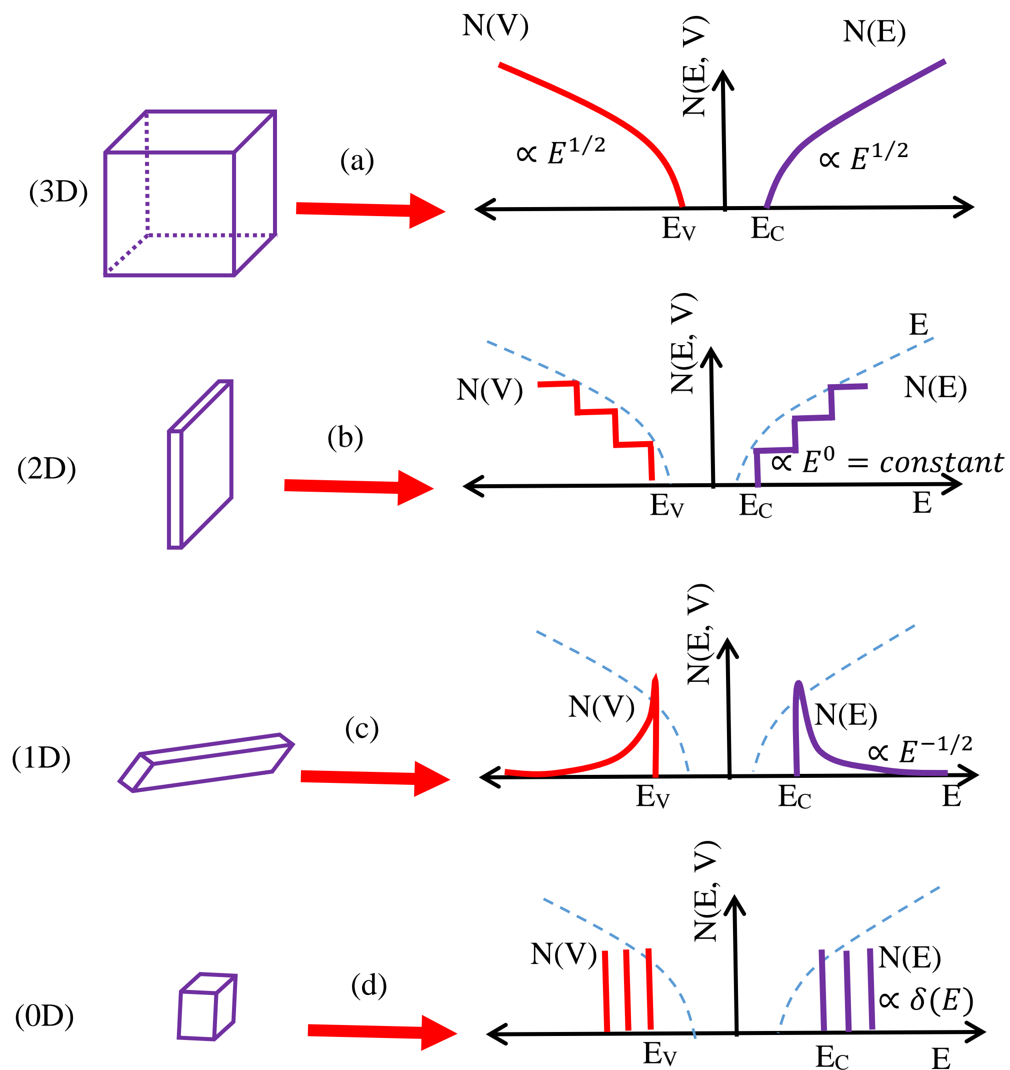

Fig. 2.7. Density of states for (a) bulk semiconductor or three dimensional system (3D), (b) two dimensional systems (2D), (c) one dimensional systems (1D), and (d) zero dimensional systems (0D) [3].

A simple effective-mass approximation model can be used to estimate the quantum confinement effect corresponding to the size of the nanostructure.

For the quantum well, the energy level can be written as:

$$E_{n_x}(k_{y,z}) = \frac{\hbar^2}{2m^*}\left(\frac{n_x\pi}{L_x}\right)^2 + \frac{\hbar^2 k_y^2}{2m^*} + \frac{\hbar^2 k_z^2}{2m^*} \qquad (2.9)$$

The energy levels of the quantum wire can be expressed as:

$$E_{n_x n_y}(k_x) = \frac{\hbar^2\pi^2}{2m^*}\left(\frac{n_y^2}{L_y^2} + \frac{n_z^2}{L_z^2}\right) + \frac{\hbar^2 k_x^2}{2m^*} \qquad (2.10)$$

While the energy levels of the quantum dot is

$$E_{n_x n_y n_z} = \frac{\hbar^2\pi^2}{2m^*}\left(\frac{n_x^2}{L_x^2} + \frac{n_y^2}{L_y^2} + \frac{n_z^2}{L_z^2}\right) \qquad (2.11)$$

where n_x, n_y and $, n_z = 1, 2 \ldots$ are the quantum confinement numbers, L_x, L_y and L_z are the confining dimension. k_x, k_y and k_z are the wavevectors along the x, y and z-axis, respectively.

2.3 HETEROJUNCTION STRUCTURES

Homojunction and heterojunction structures are two well-known types of structures. A homojunction structure is formed when layers of same semiconductor materials are grown on top of each other. Normally these materials have the same band gaps with different doping as shown in Fig. 2.8 (a). However, when two different crystalline semiconductor materials with different band gaps (and/or lattice constants) are grown on top of each other they form a heterojunction structure as illustrated in Fig 2.8 (b).

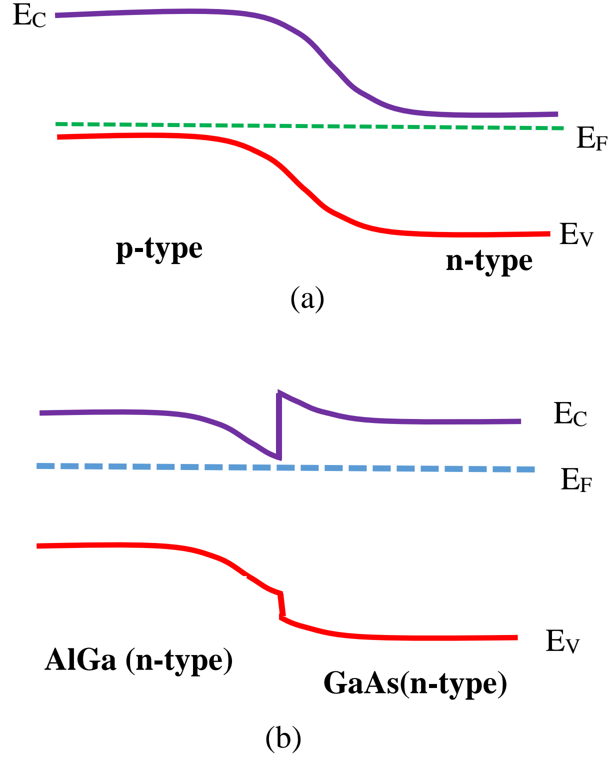

Fig. 2.8 Schematic illustration of (a) a homojunction structure and (b) a heterojunction structure.

2.3.1 LATTICE MISMATCH

A lattice-matched structure normally refers to a structure that has two materials featuring the same lattice constants and are grown on top of each other (Fig. 2.9 (a)). On the other hand, if two materials featuring different lattice constants are grown on top of each then the structure is called a lattice-mismatched structure. The lattice-mismatch can be given by

$$\frac{\Delta a}{a} = \frac{a_{layer} - a_s}{a_s} \qquad (2.12)$$

where a_{layer} and a_s are the lattice constants of layer and substrate, respectively.

In such a structure, defects are created at the interface of the heterojunction and as the lattice constants of the two materials are significantly different these defects tend to increase. Compressive and tensile are two types of strain involved in lattice-

mismatched systems. Fig. 2.9 (b) shows a compressive strain which normally forms when the lattice constant of the grown semiconductor layer is larger than that of the substrate. A tensile strain, on the other hand, forms when the lattice constant of the grown layer is smaller than that of the substrate (Fig. 2.9 (c)).

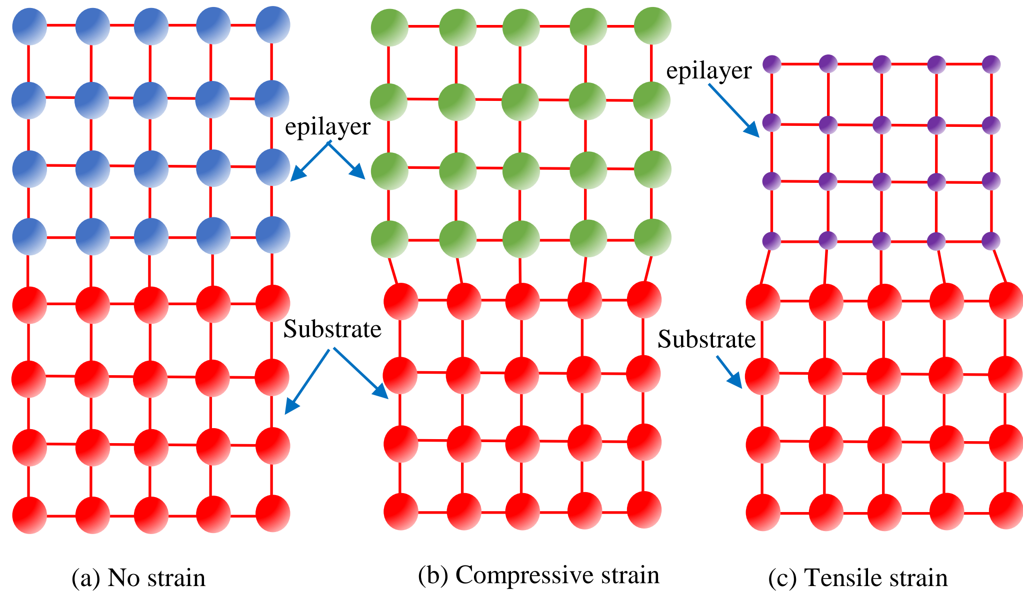

Fig. 2.9. Schematic illustration of (a) lattice matched structure, (b) Compression strain (lattice mismatched structure) and (c) Tensile strain (lattice mismatched structure).

2.3.2 ATOM SIZE AND ELECTRONEGATIVITY

The size of the atoms of two different materials, electronegativity (χ), and energy band alignment besides the lattice matching (mismatching) are the main factors which play essential roles in the growth of a heterojunction structure. In particular, the strain can be created during the growth process as a result of using two different materials having different sizes of atoms. The electronegativity (χ) normally is defined as the ability of an atom or molecule to attract an electron towards itself in order to form a chemical bond. χ is a unitless quantity but is generally referred to

as Pauling scale. In 1932 Linus Pauling carried out the first principal study of electronegativity [9]. Based on Pauling's theory, if A and B are two different semiconductor materials used to form a heterostructure, the difference in the electronegativity of these two materials ($\chi_A - \chi_B$) is given by

$$\chi_A - \chi_B = \left[(eV)^{\frac{-1}{2}}\right] \sqrt{E_D(AB) - \frac{[E_D(AA)+E_D(BB)]}{2}} \qquad (2.13)$$

where χ_A and χ_B are the electronegativity of A and B, respectively. While $E_D(AB)$, $E_D(AA)$ and $E_D(BB)$ are the dissociation energies in eV between the atoms AB, AA and BB, respectively. The factor $\left[(eV)^{\frac{-1}{2}}\right]$ is introduced to make the value of electronegativity unitless.

2.3.3 BAND ALIGNMENTS

The formation of heterojunctions is influenced by the band alignment between two semiconductor materials. Fig. 2.10 shows three different kinds of band alignments, namely, straddled alignment or type-I, staggered alignment or type-II and broken gap alignment or type-III. In type-I band alignment, the valence band of the smaller energy gap material (B) lies within the valence band of the larger energy gap material (A) and the conduction band of material (B) with the smaller energy gap lies within the conduction band of material (A) with the larger energy gap. Typical examples of such alignment are InGaAs/InP and AlGaAs/GaAs structures. While, if both conduction band edge and valence band edge of the larger bandgap material (A) are above the corresponding conduction and valence band edge of the smaller bandgap material (B), the alignment is known as type-II band alignment, such as GaSb/GaAs heterojunctions. On the other hand, if the conduction band edge of one material (B) is below the valence band edge of the other material (A), then the line-

up is known as type-III band alignment. The GaSb/InAs heterostructure is an example of such alignment.

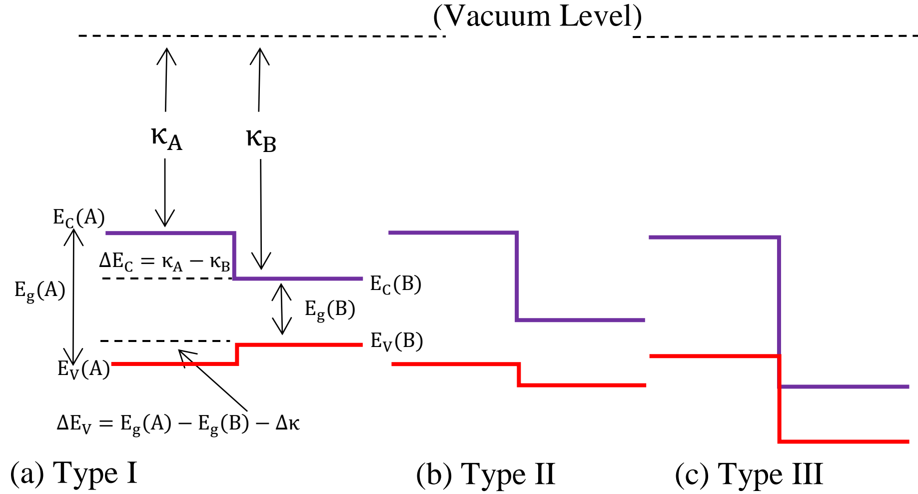

Fig. 2.10. Types of energy bands alignments in heterojunctions, where E_C, E_V, E_g, ΔE_C, ΔE_V are the conduction band, valence band, energy gap, conduction band offset, and valence band offset. κ_A and κ_B are electron affinity of materials A and B, respectively.

The electron affinity rule was the first theoretical model proposed in 1962 [10] by Anderson to calculate the band offset of an ideal semiconductor heterostructure. According to this model, the difference in electron affinities of two different materials ($\kappa_A - \kappa_B$) results in the additive offset of both conduction band (ΔE_C) and valence band (ΔE_V). These are given by

$$\kappa_A - \Delta E_C - \kappa_B = 0 \qquad (2.14)$$

$$\Delta E_V = \Delta E_g - \Delta E_C \qquad (2.15)$$

However, the electron affinity rule has some limitations. This is because it does not include defect states, surface interface states and dislocations. Also it considers intrinsic semiconductors so no donors/acceptors charges. It worth pointing out that a simple model for p-n junction is shown in Fig 4.1 (Chapter 4).

2.4. GENERAL PROPERTIES OF SELECTED SEMICONDUCTOR MATERIALS

In this section some of the important properties of the semiconductors studied in this thesis will be reviewed.

2.4.1. GaAs

Gallium arsenide (GaAs) is one of the most familiar and most important III-V compound semiconductor material. This compound is made by combining Gallium (Ga, group (III)) and Arsenic (As, group (V)) elements from the periodic table. Although Goldschmidt discovered this compound in 1920, its properties remained unknown until 1952. Fig. 2.11 illustrates the energy band diagram of GaAs. This diagram clearly shows that both the maxima of the valence band and the minima of the conduction band lie at the same value of wave vector at $k = 0$. Thus when an electron moves from the valence band to the conduction band, the momentum is conserved. Consequently, GaAs has a direct band gap which makes this compound suitable for optoelectronics devices compared to indirect band gap semiconductor such as Si.

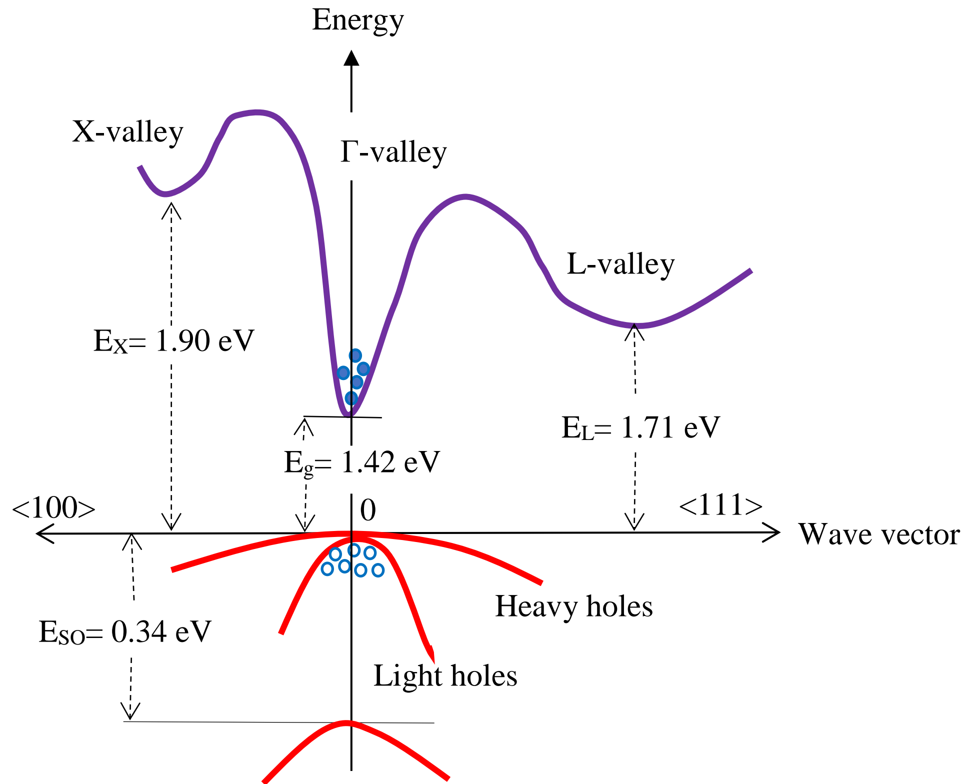

Fig. 2.11. Energy band diagram of GaAs. E_{SO}, E_X, E_L are energy of spin-orbital splitting, energy of X-valley and energy of L-valley, respectively.

GaAs is used as a semi-insulating substrate in high frequency integrated circuits because it has a very high resistivity (~ 10^8 Ω-cm) compared to Si (~ 6.4×10^2 Ω-cm) and hence parasitic capacitive effects are much less. Moreover, GaAs devices can operate at higher temperatures than Si devices due to their larger energy gap compared to Si. Key intrinsic GaAs properties at room temperature (300 K) are listed in Table 2.2.

Table 2.2. Some important properties of intrinsic GaAs at 300K. h_h and l_h represent heavy hole and light hole, respectively [11].

Parameter	GaAs
Crystal Structure	Zincblende
Lattice constant (Å)	5.6533
Crystal density (g/cm^3)	5.360
Energy band gap (eV)	1.42
Band type	Direct
Electron effective mass	0.063 m_0
Hole effective mass	0.51 m_0 (h_h) 0.082 m_0(l_h)
Dielectric constant (static)	12.85
Electron affinity (eV)	4.07

2.4.2. DILUTE GaAsN

The first epitaxial growth of a new family of III-V semiconductors known as the dilute nitride semiconductor materials was demonstrated in 1990s [12-14]. These materials have unusual physical properties which make them favourable for use in technological applications such as optical amplifiers, solar cells, and long wavelength lasers [15-18].

When isovalent impurity atoms substitute a host atom of the same valency, semiconductor alloys are formed and weak perturbations are produced in the host crystal band structure. The host band structure can be changed significantly when the isovalent impurity atoms and the host atoms have different properties such as electronegativity, atomic radii, etc.

For example, the band structure of GaAs changes slightly when an impurity atom such as phosphorus (P) substitutes As or indium (In) substitutes Ga in GaAs.

However, the band structure of GaAs changes significantly when nitrogen (N) atoms are incorporated due to the formation of single GaAsN crystal. For each percent of N in the alloy, the GaAs exhibits approximately 0.1eV reduction in its energy gap. In fact due to the large differences in atom size and electronegativity of N atoms and host anions [19], a significant local potential is produced. Consequently this leads to the creation of N-related localized states near the conduction band edge which causes the reduction in the band gap and other associated effects. Shan *et al.* [20] have introduced the band anticrossing model (BAC) that has been used extensively to explain the characteristics of GaAsN. This model is described briefly below.

2.4.2.1. THE BAND ANTICROSSING (BAC) MODEL

In the BAC model the interaction between the localized state of nitrogen and the extended conduction band states of the host semiconductor matrix [20, 21] is used to explain the electronic structure of N-alloys. This interaction causes the conduction band splitting into the E_- and E_+ bands, and a reduction of the fundamental band gap, which is enhanced as the N concentration increases.

Fig. 2.12 illustrates the anticrossing behaviour between the N-related state (E_N) and conduction band edge (E_{CB}) of GaAs. Because the N related states have localised nature, they are spread over the reciprocal space with constant energy. E_N and E_{CB} energy states are represented in Fig. 2.12 by dotted lines. According to the BAC model, the energy of these two states resulting from their interaction is given by

$$E_{\pm} = \frac{1}{2}\left(E_N + E_{CB} \pm \sqrt{(E_N - E_{CB})^2 + 4V_{CB,N}^2}\right) \quad (2.16)$$

where $V_{CB,N}$ is the coupling parameter describing the strength of interaction between the localized N states and extended CB states which is written as:

$$V_{CB,N} = C_N . x^{\frac{1}{2}} \tag{2.17}$$

where C_N is a constant whose value depends on the semiconductor host and x is the nitrogen fraction in the alloy.

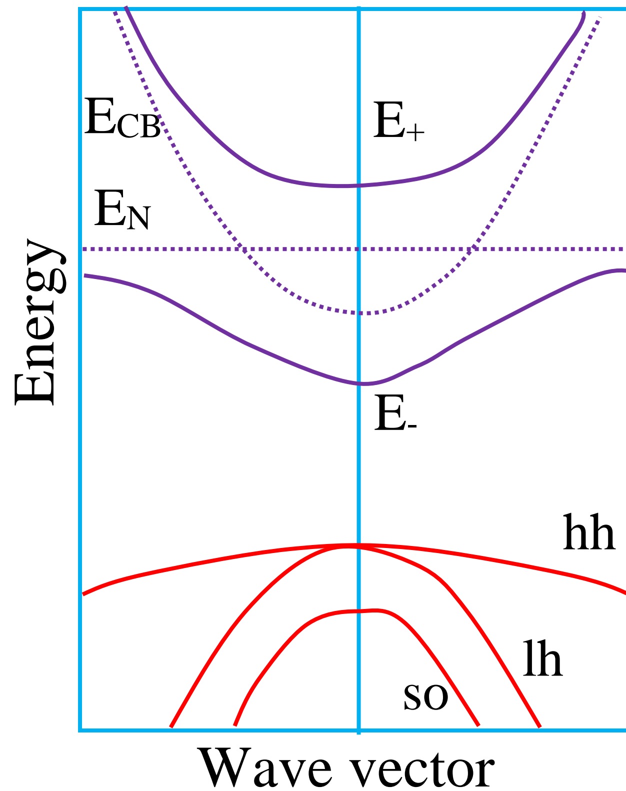

Fig. 2.12. Schematic diagram of band anticrossing model of GaAsN.

It worth pointing out that the BAC model is a non-ideal model because it does not consider the broadening of the energy levels or splitting of L-conduction band extrema, and only describes the interaction between a single isovalent impurity level and the conduction band edge. However, the BAC model has been a common and most cited model in dilute nitride literature because of its simplicity and satisfactory fit for many characteristics of the alloy.

2.4.2.2. SOME IMPORTANT PROPERTIES OF GaAsN

GaAsN has revealed uncommon properties such as a large band gap reduction, enhancement of the effective mass, small lifetime of the charge carriers, and low charge carrier mobility. Some of these properties are given below.

Many studies of dilute nitrides alloys reported a different set of values of the effective mass of the electron ranging from $m_e^* \sim 0.8m_o$ to $0.1m_o$ (m_o is the mass of the electron at rest). In dilute nitride materials the enhanced effective mass (GaAs: $m_e^* \sim 0.0663m_o$) and large alloy scattering lead to the degradation of mobility of electrons and holes. For example, Ptak *et al.* [22] observed a strong degradation of hole mobility in both molecular beam epitaxy (MBE) and metal organic chemical vapour deposition (MOCVD) grown GaAsN samples. Similarly a decrease in electron mobility is observed and is correlated to the enhancement of the electron effective mass [23].

For light emitting devices the lifetime of the charge carrier is considered to be an important parameter. Dilute nitride materials have smaller carrier lifetime because they have high defect densities. Ahrenkiel *et al.* [24] have reported less than 1ns lifetime of the carriers at room temperature in GaAsN with one percent nitrogen.

Undoped dilute nitrides materials grown by MBE or by MOCVD are normally p-type semiconductors [25]. However, Kurtz *et al*. [26] have observed the conversion of the type of conductivity when they annealed their samples. They have ascribed this transformation of conductivity type to nitrogen-hydrogen defects which were formed as a result of annealing.

2.4.3. GaN

Gallium nitride (GaN) is a direct bandgap semiconductor belonging to the III-V group. The compound is mechanically very hard, and usually crystallizes in the

wurtzite hexagonal close packed (HCP) and cubic zincblende crystal structures [27]. However, wurtzite has been found to be a more stable structure than the cubic zincblende.

Due to its many superior material properties, GaN has attracted a lot of attention and therefore has become a hot research topic. GaN has a wide band gap of 3.4 eV which makes this compound a good candidate for durable devices in extreme environmental conditions such as high temperatures and voltages [28], and therefore it is a good candidate for high power applications. Furthermore, GaN is a potential candidate for space and military applications because this compound has a higher radiation hardness than GaAs [29]. GaN has a significantly higher thermal conductivity than that of GaAs which makes this compound more applicable for higher power operation needs compared to GaAs power devices. For applications requiring high saturation currents and high frequencies, GaN is the preferred material of choice compared to Si, SiC and GaAs. This is due to the fact that GaN has higher saturated electron drift velocity than its competitors.

GaN can be deposited as a thin film on sapphire or SiC substrates [30]. To form n-type conductivity GaN is normally doped with Si or oxygen [31], while, to form p-type conductivity GaN is doped with Mg [32].

REFERENCES

[1] M. Grundmann, *The physics of semiconductors: an introduction including devices and nanophysics*. (Springer, 2006).

[2] B. Sapoval, C. Hermann and C. Hermann, *Physics of semiconductors*. (Springer, 2003).

[3] S. M. Sze and K. K. Ng, *Physics of semiconductor devices*. (John Wiley & Sons, 2006).

[4] Y. P. Varshni, Physica **34** (1), 149 (1967).

[5] P. Wang, S. Holmes, T. Le, R. Stradling, I. Ferguson and A. De Oliveira, Semiconductor science and technology **7** (6), 767 (1992).

[6] K. Uesugi, I. Suemune, T. Hasegawa, T. Akutagawa and T. Nakamura, Applied Physics Letters **76** (10), 1285 (2000).

[7] I. Vurgaftman and J. Meyer, Journal of Applied Physics **94** (6), 3675 (2003).

[8] D. Wood, *Optoelectronic semiconductor devices*. (Prentice Hall, 1994).

[9] L. Pauling, Journal of the American Chemical Society **54** (9), 3570 (1932).

[10] R. Anderson, IBM Journal of Research and Development **4** (3), 283 (1960).

[11] S. T. Thornton and A. Rex, *Modern physics for scientists and engineers*. (Cengage Learning, 2012).

[12] M. Weyers, M. Sato and H. Ando, Japanese Journal of Applied Physics **31** (7A), L853 (1992).

[13] M. Kondow, K. Uomi, A. Niwa, T. Kitatani, S. Watahiki and Y. Yazawa, Japanese Journal of Applied Physics **35** (2S), 1273 (1996).

[14] M. Kondow, K. Uomi, T. Kitatani, S. Watahiki and Y. Yazawa, Journal of Crystal Growth **164** (1), 175 (1996).

[15] S. R. Kurtz, A. Allerman, E. Jones, J. Gee, J. Banas and B. Hammons, Applied Physics Letters **74** (5) (1999).

[16] J. Wei, F. Xia, C. Li and S. R. Forrest, IEEE Photonics Technology Letters **14** (5), 597 (2002).

[17] M. Shafi, R. Mari, M. Henini, D. Taylor and M. Hopkinson, physica status solidi (c) **6** (12), 2652 (2009).

[18] P. J. Thijs, L. F. Tiemeijer, P. Kuindersma, J. Binsma and T. Van Dongen, IEEE Journal of Quantum Electronics **27** (6), 1426 (1991).

[19] H. P. Hjalmarson, P. Vogl, D. Wolford and J. D. Dow, Physical Review Letters **44** (12), 810 (1980).

[20] W. Shan, W. Walukiewicz, J. Ager III, E. Haller, J. Geisz, D. Friedman, J. Olson and S. R. Kurtz, Physical Review Letters **82** (6), 1221 (1999).

[21] A. Lindsay and E. O'Reilly, Solid State Communications **112** (8), 443 (1999).

[22] A. Ptak, S. Johnston, S. Kurtz, D. Friedman and W. Metzger, Journal of Crystal Growth **251** (1), 392 (2003).

[23] C. Skierbiszewski, P. Perlin, P. Wisniewski, T. Suski, W. Walukiewicz, W. Shan, J. Ager, E. Haller, J. Geisz and D. Friedman, physica status solidi (b) **216** (1), 135 (1999).

[24] R. Ahrenkiel, S. Johnston, B. Keyes, D. Friedman and S. Vernon, Applied Physics Letters **77** (23), 3794 (2000).

[25] J. Geisz and D. Friedman, Semiconductor science and technology **17** (8), 769 (2002).

[26] S. Kurtz, J. Geisz, D. Friedman, W. Metzger, R. King and N. Karam, Journal of Applied Physics **95** (5), 2505 (2004).

[27] M. Suzuki and T. Uenoyama, Japanese Journal of Applied Physics **34** (7R), 3442 (1995).

[28] M. Trivedi and K. Shenai, Journal of Applied Physics **85** (9), 6889 (1999).

[29] A. Ionascut-Nedelcescu, C. Carlone, A. Houdayer, H. Von Bardeleben, J.-L. Cantin and S. Raymond, IEEE Transactions on Nuclear Science **49** (6), 2733 (2002).

[30] I. Akasaki and H. Amano, Japanese Journal of Applied Physics **36** (9R), 5393 (1997).

[31] C. Wetzel, T. Suski, J. Ager III, W. Walukiewicz, S. Fischer, B. Meyer, I. Grzegory and S. Porowski, International conference on physics of semiconductors, Berlin, Germany, (1996).

[32] H. Amano, M. Kito, K. Hiramatsu and I. Akasaki, Japanese Journal of Applied Physics **28** (12A), L2112 (1989).

CHAPTER 3: SEMICONDUCTOR DEFECTS AND THEIR PROPERTIES

This chapter discusses various types of defects and their role as trapping and generation recombination centres. The deep level defects and their carrier kinetics processes are also described. In addition, the presence of defects in GaAs, dilutes GaAsN, and GaN, semiconductor materials and their properties will also be highlighted.

3.1 CLASSIFICATION OF DEFECTS

A perfect crystal is created by a periodic arrangement of unit cells along the crystal orientation. But in reality there are many types of defects ranging from point, complexes, and extended defects which make the crystal not perfect. In this section, a review of the most important defects will be discussed.

3.1.1 POINT DEFECTS

When an atom is missing or is located in an irregular place in the lattice structure, it is called a point defect or a zero dimensional defect. Therefore, a point defect interrupts the crystal arrangement at an isolated site. This kind of defect can be found in different forms such as vacancy, substitutional, interstitial and antisite impurities. Normally a vacancy defect is created as a result of a missing atom at a certain crystal lattice site in a crystal structure as illustrated in Fig. 3.1 (a). Another type of defect, the substitutional impurity, is formed when a foreign atom impurity replaces and occupies a regular lattice site of the host atom as shown in Fig. 3.1 (b). Similarly, an antisite is a special kind of substitutional defect which occurs when a host atom occupies the site of another host atom. An example of an antisite defect

in GaAs material is shown in Fig.3.1 (c) where a Ga atom occupies an As site [As antisite (Ga_{As})] and vice versa [Ga antisite (As_{Ga})]. Fig 3.1 (d) shows the fourth form of a point defect known as an interstitial impurity. This impurity is formed when an atom occupies the space between regular lattice sites. If this atom is the same as the host crystal then it is called self-interstitial. But if this atom is a foreign atom then it is called foreign-interstitial.

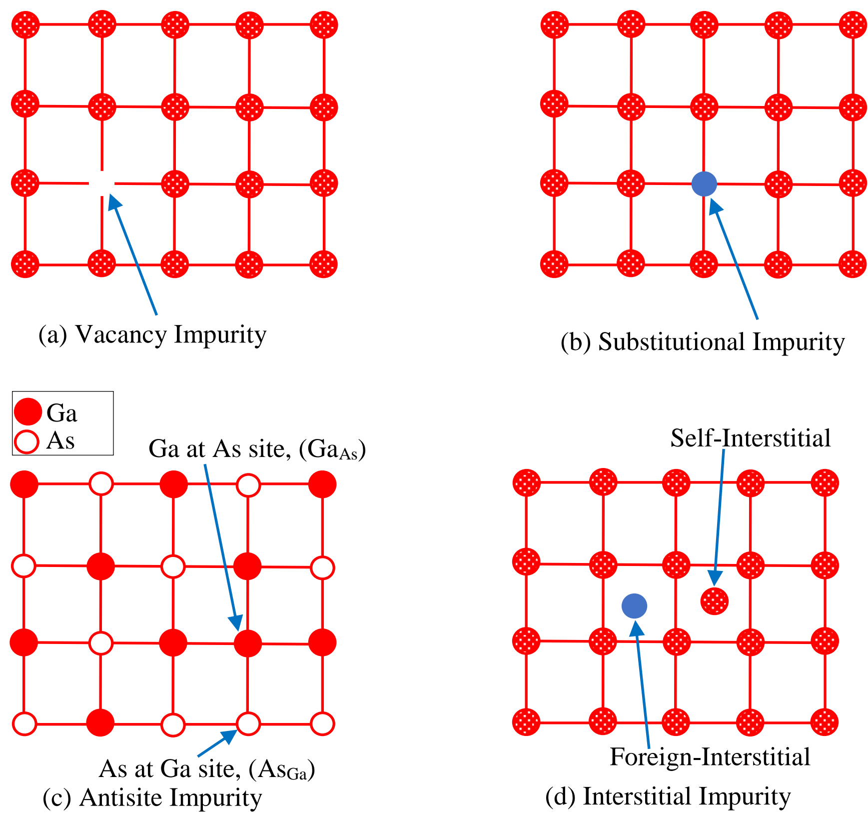

Fig. 3.1. Illustration of different forms of point defects in crystalline semiconductors: (a) Vacancy impurity; (b) Substitutional impurity; (c) Antisite impurity; and (d) Interstitial impurity.

3.1.2 COMPLEXES OF POINT DEFECTS

Point defects can be bounded to each other similar to the bounds between atoms in molecules. In the case of point defects, two or more point defects can interact with

each other and form pairs known as point complexes defects. For example, when two interstitials atoms form a pair, a complex defect is created and this is called split-interstitials defect as shown in Fig. 3.2 (a). These defects are formed by either a pair of two interstitial atoms of the same host material or by a pair of two impurity interstitials atoms. Vacancy defects also can form different kinds of complexes in a crystalline material as demonstrated in Fig. 3.2 (b). In particular, when two vacancies form a pair, the resultant complex is called a Di-vacancy. Furthermore, a Frenkel defect is created when a vacancy and a self-interstitial atom form a pair. Besides, a vacancy-impurity complex is formed when a pair of a vacancy and a foreign-interstitial interact with each other. In addition, when two vacancies and interstitial atom form a pair, a complex is created known as a split vacancy.

Fig. 3.2 (c) shows another type of complex defect known as impurity-pair which is created when a substitutional impurity atom forms a pair with an interstitial impurity atom.

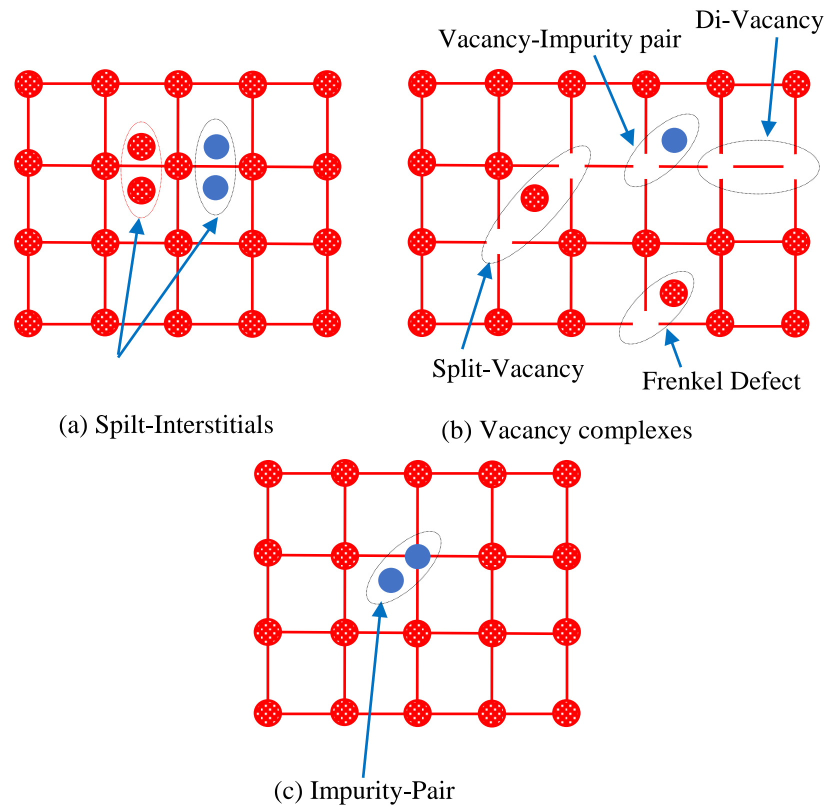

Fig. 3.2. Illustration of different forms of complex defects: (a) spilt-interstitials, (b) vacancy complexes, and (c) complexes of impurity-pair.

3.1.3 LINEAR DEFECTS

The linear defects (dislocations) are one-dimensional defects that normally occur when a line of atoms are out of their regular position in the crystal. Edge dislocations and screw dislocations are basic types of linear defects. As shown in Fig. 3.3 (a), when an extra half plane of atoms is inserted into the crystal lattice, distortion of nearby atoms occurs and this creates an edge dislocation. Moreover, a screw dislocation shown in Fig. 3.3 (b) is formed when one part of the crystal lattice is shifted with respect to the other crystal part.

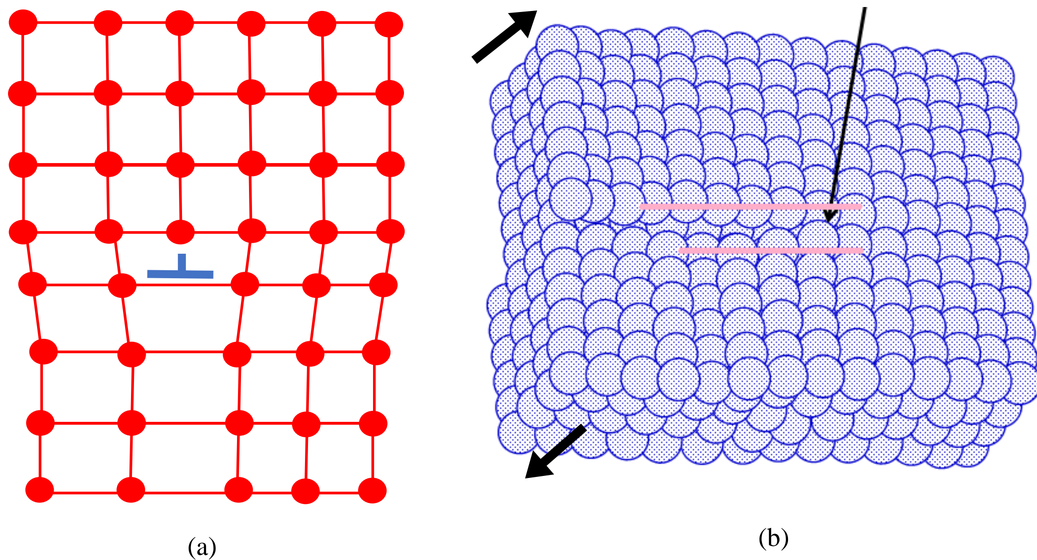

Fig. 3.3. Illustration of different forms of linear defects: (a) edge dislocations and (b) screw dislocations.

3.2 DEFECTS AND THEIR CARRIER KINETICS

3.2.1 SHALLOW LEVELS AND DEEP LEVELS DEFECTS

Defects can also be classified by the energy levels that they introduce within the bandgap of the material. In particular, shallow levels impurities (dopant impurities) represent the defects that are located near the valence band or conduction band as seen in Fig. 3.4. These defects, which are intentionally introduced as dopant atoms, are known as shallow donor levels if they donate an electron to the conduction band (E_C) and shallow acceptor levels if they donate a hole to the valence band (E_V) [1]. Shallow levels normally have low ionization energy varying between 5-10 meV and are ionized easily at room temperature so that they increase the electrical conductivity of the semiconductors.

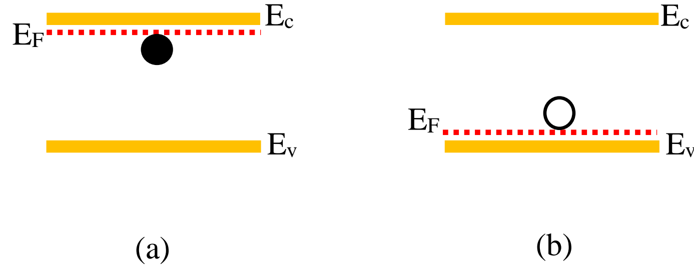

Fig. 3.4. Schematic diagram of (a) shallow donor level, and (b) shallow acceptor level. E_c, E_v and E_F represent conduction band energy, valence band energy and Fermi level, respectively.

As shown in Fig. 3.5, deep level defects are located far from the bandgap edges and have energies larger than 100 meV. These energy levels are also known as recombination-generation centres and they can play an important role in the electrical and optical properties of the materials. Consequently, it is becoming very essential to understand the conduction mechanism involving these impurities levels. Thus, in the next section, the conduction mechanism involving these impurities levels will be explained.

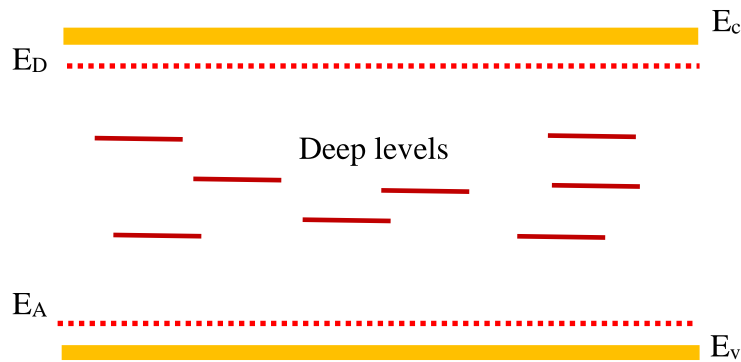

Fig. 3.5. Schematic diagram of deep level defects in semiconductors. E_D and E_A represent shallow donor level and acceptor donor level, respectively.

3.2.2 SHOCLEY-READ-HALL THEORY

Recombination phenomena occur when a free electron occupies a "vacant" location (i.e. a hole) in the covalent bond. Conversely, if an electron has enough energy to become free from a covalent bond, this creates a free hole in that process, which is called "generation of an electron-hole pair". At thermodynamic equilibrium, the equilibrium concentrations of electrons and holes remain constant with respect to time that leads to balance the rates of generation and recombination processes. However, if an external source of energy such as light is used, the carrier concentration will increase and therefore the generation and recombination processes occur at unequal rates. Thus the system will be under non-equilibrium conditions [2].

In order to determine the occupancy of recombination-generation centres (G-R centres) at equilibrium the emission and capture rates of charge carriers should be understood. If E_T is considered to be the energy of a defect laying within the forbidden bandgap of the semiconductor, then four sub-processes are possible [2]:

(i) Electron capture, c_n: in this process an empty trap captures an electron from the conduction band (Fig. 3.6 (a)).

(ii) Electron emission, e_n: in this process a trapped electron is emitted from level E_T to the conduction band (Fig. 3.6 (b)).

(iii) Hole capture, c_P: in this process a trapped electron captures a hole from the valence band (Fig. 3.6 (c)).

(iv) Hole emission, e_p: in this process an empty trap emits a hole from level E_T to the valence band (or an electron from the valence band is trapped leaving a hole in the valence band) (Fig. 3.6 (d)).

Fig. 3.6 shows the capture and emission processes of electron and hole. n is the electron density, p is the hole density, c_n is the electron capture coefficient, e_n is the electron emission rate, p_T is a G-R centre occupied by a hole, n_T is a G-R centre occupied by an electron, c_p is the hole capture coefficient and e_p is the hole emission rate.

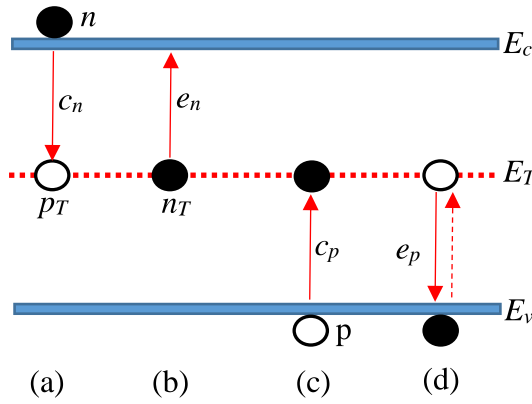

Fig. 3.6. Schematic diagram of capture and emission processes: (a) capture of electron (b) emission of electron (c) capture of hole and (d) emission of hole [2].

The state n_T is neutral when a G-R centre is a donor, while the state p_T is positively charged. On the other hand, if a G-R centre is an acceptor, then the state p_T is neutral and the state n_T is negatively charged. The total density of G-R centres, N_T, occupied by electrons n_T and holes p_T, is equal to:

$$N_T = n_T + p_T \quad (3.1)$$

When an electron or hole is generated by a centre or recombine in a centre the electron density in the conduction band (n), the hole density in valence band (p) and charge states of the centres n_T and p_T are changed with time. The rate of change of n with respect to time is given by the following relation:

$$\frac{dn}{dt}\Big|_{G-R} = (b) - (a) = e_n n_T - c_n n p_T \quad (3.2)$$

From Equation (3.2), one can realize that the emission rate, e_n, (i.e. the number of electrons per second emitted by G-R center to the conduction band) and the concentration of the traps that are occupied by electrons, n_T, are the only parameters that affect the electron emission. Also from this equation, it is clear that the electron capture process depends only on the presence of electrons in the conduction band, n, the electron capture rate, c_n, and the concentration of the traps that are occupied by holes p_T.

Similarly, the change of holes density with respect with time is mathematically expressed as:

$$\frac{dp}{dt}|_{G-R} = (d) - (c) = e_p p_T - c_p p n_T \qquad (3.3)$$

In fact, the electron capture coefficient c_n depends on the electron thermal velocity υ_{th} and the electron capture cross-section of the G-R center σ_n. c_n can be expressed as:

$$c_n = \upsilon_{th}\sigma_n \qquad (3.4)$$

The concentration of the G-R state changes as a function of time during the emission or capture process and this rate change can by calculated using Equations (3.2) and (3.3). This is given by:

$$\frac{dn_T}{dt}|_{G-R} = \frac{dp}{dt} - \frac{dn}{dt} = (c_n n + e_p)(N_T - n_T) - (c_p p + e_n)n_T \quad (3.5)$$

Since, $\frac{dn_T}{dt} = 0$ in the steady state condition, then Equation (3.5) can be rewritten and rearranged as:

$$n_T = \frac{e_p + c_n n}{e_n + c_n n + e_p + c_p p} N_T \qquad (3.6)$$

The detail balance principle states that the rate of creation and rate of absorption in semiconductors are the same when semiconductors are at thermal equilibrium. According to this principle;

$$e_n n_T = c_n n p_T \quad (3.7)$$

Substituting the electron capture coefficient c_n using Equation (3.4) into Equation (3.7) yields:

$$e_n n_T = v_{th} \sigma_n n p_T \quad (3.8)$$

Similarly,

$$e_p p_T = v_{th} \sigma_p p n_T \quad (3.9)$$

The total density of deep levels with respect to Fermi-Dirac distribution, f, is given by

$$N_T = n_T + p_T = N_T f + N_T(1 - f) \quad (3.10)$$

where f gives the probability of an electron occupying the energy level E_T and is given by

$$f = \left[\frac{1}{1+\exp\left(\frac{E_T - E_F}{k_B T}\right)}\right] \quad (3.11)$$

where E_F is the energy of the Fermi level, k_B is Boltzmann constant and T is temperature.

So by using Equations (3.10) and (3.11) in Equation (3.7), this gives

$$e_n = \sigma_n \langle v_n \rangle_{th} n \exp\left(\frac{E_T - E_F}{k_B T}\right) \quad (3.12)$$

where n is the electron density in conductance band and is given by

$$n = n_i \exp\left(\frac{E_F - E_i}{k_B T}\right) = N_c \exp\left(-\frac{E_c - E_F}{k_B T}\right) \quad (3.13)$$

where n_i is the intrinsic carrier concentration, $n_i = N_c \exp\left(\frac{E_i - E_c}{k_B T}\right)$.

Subsequently, by substituting Equation (3.13) in Equation (3.12), this gives:

$$e_n = \sigma_n \langle \upsilon_n \rangle_{th} N_c \exp\left(-\frac{E_c - E_T}{k_B T}\right) \qquad (3.14)$$

where N_c is the density of states in the conduction band, $N_c = 2\left(\frac{2\pi m_e^* k_B T}{h^2}\right)^{3/2}$ and $\langle \upsilon_n \rangle_{th}$ is the thermal velocity of electrons, $\langle \upsilon_n \rangle_{th} = \left(\frac{3k_B T}{m_e^*}\right)^{\frac{1}{2}}$ and m_e^* is the effective mass of electrons.

Similarly, substituting $p = N_\upsilon \exp\left(-\frac{E_F - E_\upsilon}{k_B T}\right)$ in Equation (3.9), gives:

$$e_p = \sigma_p \langle \upsilon_p \rangle_{th} N_\upsilon \exp\left(-\frac{E_T - E_\upsilon}{k_B T}\right) \qquad (3.15)$$

where N_υ is the density of states in the valence band, $N_\upsilon = 2\left(\frac{2\pi m_h^* k_B T}{h^2}\right)^{3/2}$ and $\langle \upsilon_p \rangle_{th}$ is the thermal velocity of holes, $\langle \upsilon_p \rangle_{th} = \left(\frac{3k_B T}{m_h^*}\right)^{\frac{1}{2}}$ and m_h^* is the effective mass of holes.

If the values of $\langle \upsilon_n \rangle_{th}$ and N_c, $\langle \upsilon_p \rangle_{th}$ and N_υ are substituted respectively in Equations (3.14) and (3.15) then one gets:

$$e_n = AT^2 \sigma_n \exp\left(-\frac{E_c - E_T}{k_B T}\right) \qquad (3.16)$$

$$e_p = AT^2 \sigma_p \exp\left(-\frac{E_T - E_\upsilon}{k_B T}\right) \qquad (3.17)$$

where A is a constant given by:

$$A = 2\left(\frac{2\pi m_e^* k_B}{h^2}\right)^{3/2} \left(\frac{3k_B}{m_e^*}\right)^{1/2} = 4m_e^* \frac{\sqrt{6\pi^3}(k_B)^2}{h^3}$$

The Arrhenius plot of $\left(\frac{e_{n,p}}{T^2}\right)$ versus $\left(\frac{1000}{T}\right)$ generates a straight line graph, and therefore the activation energy of the deep level can be extracted from the slope of this plot.

3.3 DEFECTS IN COMPOUND SEMICONDUCTORS

The use of semiconductor materials in most modern electronic devices has leads to a significant growth in the semiconductors industries. In these industries, the major hurdles and difficulties are to produce perfect crystals. In fact, all crystals have imperfections or defects since foreign atoms have the ability to enter the structure or/and some atoms can be missing in crystal structures or lattices [1]. Generally, the presence of defects in devices affects their performance by altering their electrical and optical properties. Therefore, in order to understand the performance of the devices, it is essential to identify and characterise the defects created during growth and processing of these materials and devices[2]. In the following section a brief literature review of defects in GaAs, GaAsN and GaN materials will be presented.

3.3.1 DEFECTS IN GaAs

The gallium arsenide compound is widely used in many applications in electronics and optoelectronics devices. This III-V semiconductor compound can have different types of native defects which are created in its structure during the growth process such as vacancies, interstitials, and antisite defects.

EL2 is considered as the most dominant intrinsic defect in GaAs. This defect typically has an energy in the range of 0.70 eV to 0.85 eV [3] with concentrations of ~ 10^{16} cm^{-3} and ~ 10^{14} cm^{-3} in bulk and epitaxially grown materials, respectively [4]. Its origin is assigned to the isolated Arsenic antisite defect (As_{Ga}) [5-7] or complex defect involving As_{Ga} and arsenic interstitial [7, 8]. *EL3* is another famous trap in GaAs and has an energy around ~0.575 eV [9]. This trap is commonly associated with complexes of off-center substitutional oxygen on arsenic sites (oc-

O_{As}) [10]. *EL5* having an energy ~0.43 eV is another defect found in GaAs and which was assigned to complexes involving As interstitials- Ga vacancies (As_iV_{Ga}) [11]. Yet another common intrinsic defect in GaAs with an activation energy of ~0.35 eV is *EL6* [9]. The nature of *EL6* is related to the complex defect involving arsenic antisite defect (As_{Ga}) and arsenic vacancy (V_{As}) [12]. Additionally, a low-energy trap, *EL10* (~0.18eV), is another intrinsic defect in GaAs [9] which was assigned to an arsenic vacancy (V_{As}) complex defect involving an impurity [13, 14].

3.3.2 DEFECTS IN DILUTES GaAsN

Due to the unique properties of dilute nitrides, there has been a growing interest in recent years in this material system due to the strong downward bowing of its bandgap when incorporating small amounts of nitrogen into GaAs [15]. Generally, a major perturbation in the electronic band structure is created when nitrogen atoms are incorporated into the GaAs crystal. In particular, when nitrogen atoms substitute As atoms, localised energy states are created near the conduction band edge. Consequently this leads to a large bowing of the bandgap of the semiconductors [16]. Hence the electrical and optical properties of the materials will be effected [17]. However, the quality of the crystal can degrade as a result of defects which are created by the occupation of N atoms in non-substitutional sites in the lattice of GaAs. Accordingly the optical efficiency and carrier lifetime will decrease [18-20]. This dilute nitride semiconductor can have different types of point defects such as N-interstitials, As-antisites and Ga-vacancies as reported by different studies. For example, from thermodynamic calculations Zhang and Wei [21] have reported the existence of substitutional N, N–N split interstitial and Ga vacancies. Such defects

can be found in GaAsN materials grown by MBE and MOVPE [22]. The illustrations of these defects are shown in Fig. 3.7. T. Ahlgren *et al.* [23] have reported that as the N contents increase in GaAsN, the N substitutional concentration increases. However, they have revealed that the N interstitials concentration remained unchanged (2.3×10^{19} cm^{-3}) although the contents of N increased from 0.7% to 3%. They concluded that these non-radiative recombination centres could play an important role in the reduction of the optical efficiency of nitride materials.

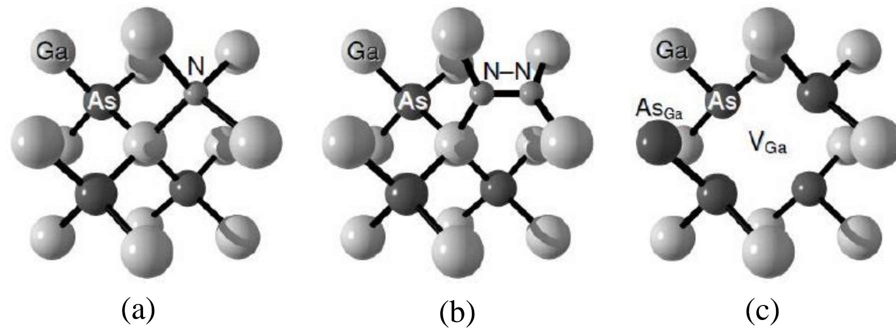

Fig. 3.7. Configurations of nitrogen in GaAsN; (a) substitutional N; (b) N–N split interstitial; (c) Ga vacancy and As antisite (after Zhang and Wei [21]).

It is worth pointing out that many scientists have deployed the DLTS technique to characterise the electrically active defects in GaAsN. For example, from DLTS measurements P. Krispin *et al.* [24] have found HK1 (0.16 eV), HK2 (0.39 eV), HK3 (0.35 eV), HK4 (0.45 – 0.55 eV) and HK5 (0.69 eV) hole traps in MBE grown p-type GaAsN samples. They reported that at the interface of GaAsN/GaAs, the HK1 trap has the highest concentration. Also they suggested that HK2 and HK5 traps can be correlated to Ga_{As} (Ga on As site) because they are comparable to the traps found in the GaAs grown by liquid phase epitaxy (LPE). HK3 trap has been

associated to copper impurities form N cell and HK4 trap has been assigned to iron impurities. Two N-related electron traps with thermal activation energies 0.8 eV and 1.1 eV above the valence band edge have been reported by P. Kripsin *et al.* [25] in Si-doped GaAsN samples and were correlated to (N-N) and (As-N) split interstitials, respectively. It is worth pointing out that the well-known defects in GaAs, EL2, EL3, EL6 and EN3, were also detected in GaAsN or GaInNAs structures [26].

A high energy irradiation of semiconductors can play an important role in the optical and electrical properties of the materials by introducing new defects or/and reducing or removing the existing defects. Normally, the irradiation induced defects are in the form of vacancies, defect clusters and dislocations in semiconductors [27]. Bouzazi *et al.* [28] studied the effect of different fluence doses of electron irradiation on GaAsN grown by chemical beam epitaxy using DLTS. In their measurements, they observed one dominant nitrogen related electron trap E1 with activation energy of 0.33 eV in all as-grown and electron irradiated samples and they tentatively inferred the origin of this defect to the split interstitial formed from one N atom and one As atom in single V-site [$(N\text{-}As)_{As}$]. However, they argued that the density of this detected level (E1) was enhanced when the fluence doses of irradiation were increased. Furthermore, they detected another level due to electron irradiation and they assigned it to EL2 native defect that is normally observed in GaAs. Recently, Klangtakai *et al.* [29] have investigated the effects of 0–2.0 MGy gamma-ray irradiation on the structural properties of $GaAs_{1-x}N_x$ films (x =1.9 and 5.1%) grown by metal organic vapour phase epitaxy using scanning electron microscopy (SEM), atomic force microscopy (AFM), high-resolution X-ray diffraction (HRXRD), and Raman spectroscopy. They clearly observed a

roughened surface with large number of holes and a surface with a cross-hatch pattern after irradiation for low and high content of N in GaAsN samples, respectively. In particular, from SEM and AFM measurements they have reported that as gamma irradiation increases, the hole density in the surface of GaAsN with low N content increased. They claimed that the partial strain relaxation at high N levels induced the creation of the cross-hatch pattern. This pattern line density varied as the irradiation dose changes. Additionally, from HRXRD and Raman spectroscopy they found that after irradiation N incorporation and strain relaxation are increased. They concluded that displacement damage and gamma-ray heating are the main sources of structural change in GaAsN samples.

3.3.3 DEFECTS IN GaN

Native defects are playing an important role in the optoelectronic and electronic properties of wide-bandgap semiconductor gallium nitride (GaN) devices.

In the early days of GaN growth, nitrogen vacancies (V_N) were implicitly assumed as the main source for as-grown material to have an unintentional n-type conductivity [30, 31]. But, later studies have concluded that other impurities such as oxygen [32] and Si [33] could explain this conductivity. However, in p-type GaN, the nitrogen vacancies are still considered as compensating centres [34].

Several groups have reported a number of deep centres in n-GaN using DLTS measurements. *E1* and *E2* are an example of these deep levels and they are normally found in unintentionally doped n-type GaN [31]. In particular, the deep level *E1*, with activation energy ranging from 0.18 eV to 0.27 eV was correlated to nitrogen vacancies [35] or line defects affected by different buffer growth conditions [36].

While *E2* level with activation energy in the range 0.50-0.60 eV is believed to originate from N antisites [37].

It is well–known that a high energy irradiation has strong effects on the electrical, optical and structural properties of semiconductor materials [38]. Thus, the investigation of a high energy radiation on the properties of GaN have been studied by different groups. Look *et al.* [39] have found that the electron mobility is degraded in n-GaN after high-energy (0.7–1 MeV) electron irradiation as a result of the creation of defects that act as scattering centres. In addition, Emtsev *et al.* [40] have reported that gamma irradiation induced point defects in silicon-doped n-GaN and the dopant concentration affects the production rate of these defects. Moreover, several groups used DLTS technique to characterise irradiation induced defects in GaN. Two distinct radiation-induced defects with thermal activation energies within the ranges of 0.13–0.20 eV and 0.76–0.90 eV have been consistently reported and are correlated to nitrogen vacancies (V_N) and nitrogen-interstitials (N_i), respectively [41-47].

REFERENCES

[1] M. D. McCluskey and E. E. Haller, *Dopants and defects in semiconductors*. (CRC Press, 2012).

[2] D. K. Schroder, *Semiconductor material and device characterization*. (John Wiley & Sons, 2006).

[3] J. Bourgoin and T. Neffati, Solid-State Electron. **43** (1), 153 (1999).

[4] H. Von Bardeleben, D. Stievenard, D. Deresmes, A. Huber and J. Bourgoin, Physical Review B **34** (10), 7192 (1986).

[5] J. Lagowski, M. Kaminska, J. Parsey Jr, H. Gatos and M. Lichtensteiger, Applied Physics Letters **41** (11), 1078 (1982).

[6] M. Baeumler, U. Kaufmann and J. Windscheif, Applied Physics Letters **46** (8), 781 (1985).

[7] A. Irvine and D. Palmer, Physical Review Letters **68** (14), 2168 (1992).

[8] M. Kaminska and E. R. Weber, Semiconductors and Semimetals **38**, 59 (1993).

[9] G. Martin, A. Mitonneau and A. Mircea, Electronics Letters **13** (7), 191 (1977).

[10] U. Kaufmann, E. Klausmann, J. Schneider and H. C. Alt, Physical Review B **43** (14), 12106 (1991).

[11] R. Yakimova, T. Paskova and C. Hardalov, Journal of Applied Physics **74** (10), 6170 (1993).

[12] K. Yokota, H. Kuchii, K. Nakamura, M. Sakaguchi, H. Takano and Y. Ando, Journal of Applied Physics **88** (9), 5017 (2000).

[13] D. V. Lang, A. Y. Cho, A. Gossard, M. Ilegems and W. Wiegmann, Journal of Applied Physics **47** (6), 2558 (1976).

[14] P. Blood and J. Harris, Journal of Applied Physics **56** (4), 993 (1984).

[15] A. Erol, Materials Science **105** (2008).

[16] L. Bellaiche, S.-H. Wei and A. Zunger, Physical Review B **54** (24), 17568 (1996).

[17] S. Ding, S. Barman, K. Horn, H. Yang, B. Yang, O. Brandt and K. Ploog, Applied Physics Letters **70**, 2407 (1997).

[18] I. Buyanova, W. Chen, B. Monemar, H. Xin and C. Tu, Applied Physics Letters **75** (24), 3781 (1999).

[19] S. R. Kurtz, J. Klem, A. Allerman, R. M. Sieg, C. Seager and E. Jones, Applied Physics Letters **80** (8), 1379 (2002).

[20] A. Fleck, B. Robinson and D. Thompson, Applied Physics Letters **78**, 1694 (2001).

[21] S. Zhang and S.-H. Wei, Physical Review Letters **86** (9), 1789 (2001).

[22] W. Li, M. Pessa, T. Ahlgren and J. Decker, Applied Physics Letters **79** (8), 1094 (2001).

[23] T. Ahlgren, E. Vainonen-Ahlgren, J. Likonen, W. Li and M. Pessa, Applied Physics Letters **80**, 2314 (2002).

[24] P. Krispin, S. Spruytte, J. Harris and K. Ploog, Journal of Applied Physics **89** (11), 6294 (2001).

[25] P. Krispin, V. Gambin, J. Harris and K. Ploog, Journal of Applied Physics **93** (10), 6095 (2003).

[26] N. Al Saqri, J. Felix, M. Aziz, D. Jameel, C. de Araujo, H. Albalawi, F. Al Mashary, H. Alghamdi, D. Taylor and M. Henini, Current Applied Physics **15** (10), 1230 (2015).

[27] S. K. Khamari, V. Dixit, T. Ganguli, S. Porwal, S. Singh, S. Kher, R. Sharma and S. Oak, Nuclear Instruments and Methods in Physics Research Section B: Beam Interactions with Materials and Atoms **269** (3), 272 (2011).

[28] B. Bouzazi, N. Kojima, Y. Ohshita and M. Yamaguchi, Current Applied Physics **13** (7), 1269 (2013).

[29] P. Klangtakai, S. Sanorpim, A. Wattanawareekul, P. Suwanyangyaun, P. Srepusharawoot and K. Onabe, Journal of Crystal Growth **418**, 145 (2015).

[30] H. P. Maruska and J. Tietjen, Applied Physics Letters **15** (10), 327 (1969).

[31] H. Cho, C. Kim and C. Hong, Journal of Applied Physics **94** (3), 1485 (2003).

[32] B. C. Chung and M. Gershenzon, Journal of Applied Physics **72** (2), 651 (1992).

[33] W. Götz, N. Johnson, C. Chen, H. Liu, C. Kuo and W. Imler, Applied Physics Letters **68** (22), 3144 (1996).

[34] C. G. Van de Walle, Physical Review B **56** (16), R10020 (1997).

[35] Z.-Q. Fang, D. C. Look, W. Kim, Z. Fan, A. Botchkarev and H. Morkoç, Applied Physics Letters **72** (18) (1998).

[36] H. Cho, K. Kim, C. Hong and H. Lee, Journal of Crystal Growth **223** (1), 38 (2001).

[37] D. Haase, M. Schmid, W. Kürner, A. Dörnen, V. Härle, F. Scholz, M. Burkard and H. Schweizer, Applied Physics Letters **69** (17), 2525 (1996).

[38] S. Goodman, F. Auret, F. Koschnick, J.-M. Spaeth, B. Beaumont and P. Gibart, Materials Science and Engineering: B **71** (1), 100 (2000).

[39] D. C. Look, D. Reynolds, J. W. Hemsky, J. Sizelove, R. Jones and R. J. Molnar, Physical Review Letters **79** (12), 2273 (1997).

[40] V. Emtsev, V. Y. Davydov, V. Kozlovskii, V. Lundin, D. Poloskin, A. Smirnov, N. Shmidt, A. Usikov, J. Aderhold and H. Klausing, Semiconductor science and technology **15** (1), 73 (2000).

[41] M. Asghar, P. Muret, B. Beaumont and P. Gibart, Materials Science and Engineering: B **113** (3), 248 (2004).

[42] F. Auret, S. Goodman, F. Koschnick, J.-M. Spaeth, B. Beaumont and P. Gibart, Applied Physics Letters **73**, 3745 (1998).

[43] S. Goodman, F. Auret, F. Koschnick, J.-M. Spaeth, B. Beaumont and P. Gibart, presented at the MRS Proceedings, 1998 (unpublished).

[44] N. Shmidt, D. Davydov, V. Emtsev, I. Krestnikov, A. Lebedev, W. Lundin, D. Poloskin, A. Sakharov, A. Usikov and A. Osinsky, physica status solidi (b) **216** (1), 533 (1999).

[45] Z. Fang, L. Polenta, J. Hemsky and D. Look, presented at the Semiconducting and Insulating Materials Conference, 2000. SIMC-XI. International, 2000 (unpublished).

[46] S. Goodman, F. Auret, M. Legodi, G. Myburg, B. Beaumont and P. Gibart, presented at the Semiconducting and Insulating Materials Conference, 2000. SIMC-XI. International, 2000 (unpublished).

[47] G. Umana-Membreno, J. Dell, G. Parish, B. Nener, L. Faraone and U. Mishra, Electron Devices, IEEE Transactions on **50** (12), 2326 (2003).

CHAPTER 4: EXPERIMENTAL TECHNIQUES

The ability of semiconductors to form different types of electrical junction leads to semiconductors being the base materials for a wide range of electronic and optoelectronic devices [1]. P-N junctions, P-I-N junctions and Schottky diodes are some examples of these junctions which are also the preferred structures for DLTS measurements. Understanding how these junctions operate is a first step to comprehend and interpret the physics of several semiconductor devices. Therefore, the basic characteristics of a p-n junction and a Schottky diode will be discussed in this chapter. Moreover, there are wide ranges of characterisation techniques available to investigate semiconductors diodes. In this study, current-voltage (I-V), capacitance-voltage (C-V), deep level transient spectroscopy (DLTS) and Laplace DLTS techniques are used to determine the electrical properties of the samples investigated. The principles and details of the hardware and software implemented by these techniques are also discussed in this chapter. Solar cell and betavoltaic battery efficiencies are covered in the last part of this chapter.

4.1 P-N JUNCTION

When p-type and n-type materials are joined together, they form a junction between them known as a p-n junction [2]. Particularly, this junction forms as a result of diffusion of electrons from the n-side to the p-side, and diffusion of holes form the p-side to the n-side, and consequently this process causes the creation of a depletion region that behaves as a barrier for further diffusion of mobile carriers from both sides of the junction.

Fig. 4.1 shows schematic illustrations of the energy band of a p-n junction before and after the formation of the junction under thermal equilibrium condition and in the absence of an applied bias. χ_s is the electron affinity of the semiconductor material. E_{Fn} and E_{Fp} represent electron and hole Fermi levels, respectively, and qV_{bi} is the built-in potential. E_c, E_v, and E_{Fi} represent conduction band energy, valence band energy and intrinsic Fermi level, respectively. The potential difference between Fermi level and intrinsic Fermi level in n-region and p-region are represented as V_n and V_p, respectively. x_n and x_p represent the depletion layer widths in the *n* and *p* regions, respectively [1, 3]. As shown in Fig. 4.1(b), the Fermi level (E_F) in the p-n junction is constant throughout the whole reign when the junction is at thermodynamic equilibrium [1]. Moreover, in Fig. 4.1(b), the n and p doped regions are considered to be uniformly doped and there is an abrupt transition between these two regions. Thus this leads to the formation of an abrupt junction (or step junction). In contrast, a linearly graded junction is formed when the doping concentration is not uniform across the p-n junction regions. Thus the change in the doping at the metallurgical junction is graded. Fig. 4.1(c) illustrates three separate regions in a p-n junction, which are the quasi-neutral p and n regions (QNR) away from the metallurgical junction, and the space-charge (or depletion) region (SCR), which is occupied by ionized shallow acceptors in the p-depletion region and ionized shallow donors in the n-depletion region.

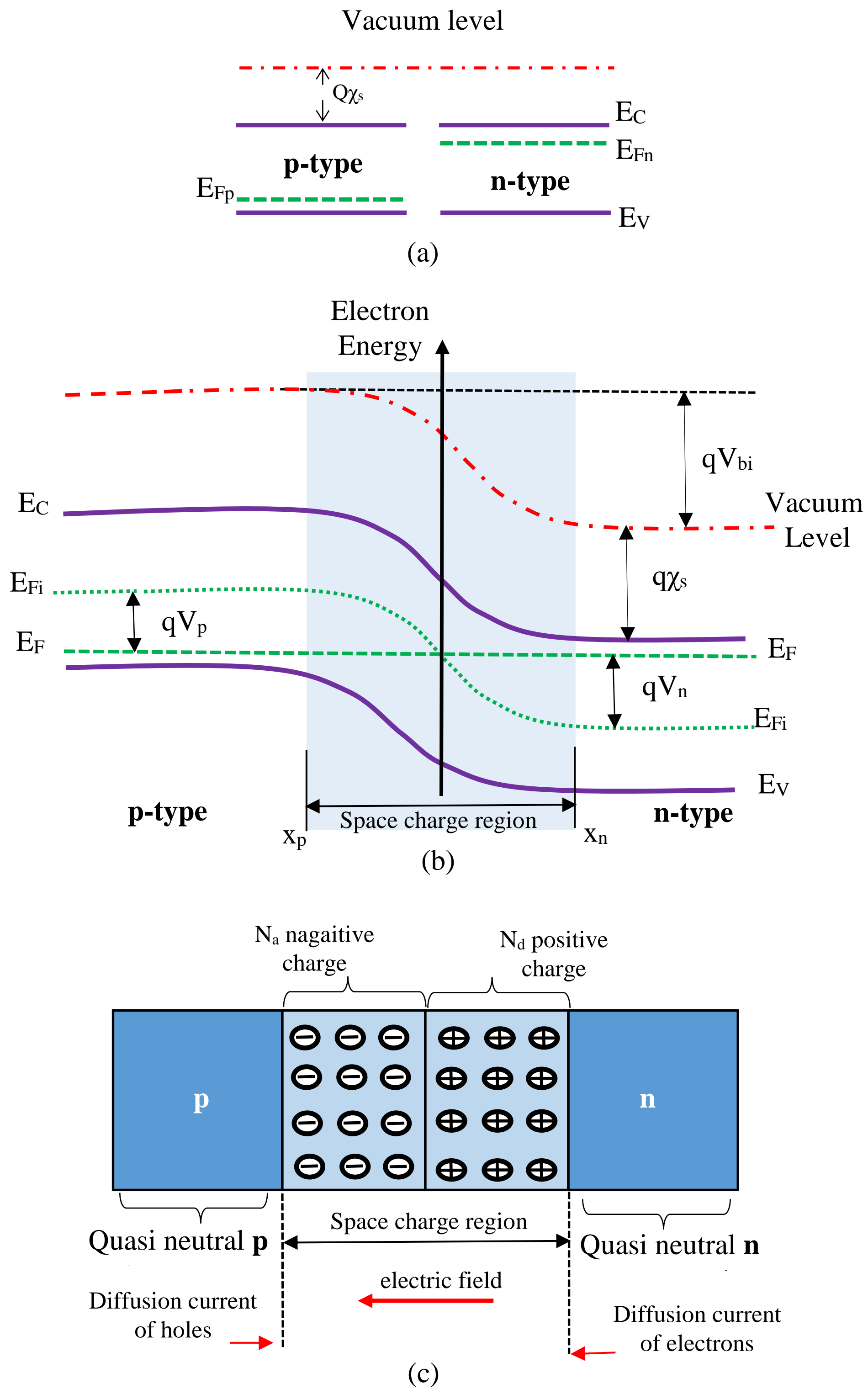

Fig. 4.1. Schematically diagram of a p-n junction: (a) the energy band structure of a p-type and n-type semiconductors before forming the junction (b) the energy band structure after the formation of the junction (c) p-n junction showing the depletion region (or space charge region).

Generally, the electron and hole concentrations in the n and p regions of a p-n junction are given by

$$n = n_i exp\left(\frac{V_n}{V_T}\right) \quad (4.1)$$

and

$$p = n_i exp\left(\frac{-V_p}{V_T}\right), \quad (4.2)$$

where n_i is the intrinsic carrier density, V_T is the thermal voltage and is equal to $\frac{k_B T}{q}$ (k_B is the Boltzmann constant, q is the electric charge, and T is the temperature), and V_n and V_p are the electrostatic potential in the n and p regions of the junction.

Poisson's equation and continuity equations are typically used to derive the carrier distribution, built-in potential, electric field, and potential profile in the junction space-charge region for abrupt and linear-graded p-n junctions.

In general, at equilibrium the relation between the charge distribution and the potential, *V* across the junction is given by the one dimensional Poisson's equation:

$$\frac{d^2V}{dx^2} = \left(\frac{dE}{dx}\right) = \frac{\rho(x)}{\varepsilon_s} = \frac{q}{\varepsilon_s}[N_D^+(x) - n(x) - N_A^-(x) + p(x)] = 0 \quad (4.3)$$

where E is the electric field, ρ is the charge density, ε_s is the permittivity of the semiconductor, *n(x)* and *p(x)* are the carrier densities at a distance *x* from the junction and $N_D^+(x)$ and $N_A^-(x)$ are uncompensated donor and acceptor ions.

In order to solve Equation (4.3), it is simplified by using the "depletion approximation". In this approximation it is assumed that: (i) there are only ionized doping impurities ($N_D^+$and N_A^-) in the SCR, (ii) the contribution of free carriers (*n*

and p) to the local charge is negligible, (iii) there are no free electrons and no free holes in the depletion region in the n-type side and in the p-type side, respectively. Therefore, in the depletion regions, the charge densities are equal to those in the n-type and p-type materials (the metallurgical junction is taken as the origin). Thus, the built-in potential, the electric field, and the charge distribution in the different regions of the p-n junction can be obtained by using appropriate boundary conditions and Equations (4.1) to (4.3). It is known that the total charge density is equal to zero in the quasi-neutral p and n regions (QNR). Consequently Equation (4.3) becomes (assuming complete ionization):

$$[n - p - N_D - N_A] = 0 \tag{4.4}$$

where N_A and N_D are the densities of holes and electrons in p-side and n-side, respectively. In the quasi-neutral n region, if one assumes that N_A to be zero (or N_A << N_D), p << n and $N_A = p = 0$, then the electrostatic potential V_n at the edge of the depletion layer can be obtained by substituting the above assumptions in Equations (4.4) and (4.1), which yield:

$$n = N_D \tag{4.5}$$

$$N_D = n_i exp\left(\frac{V_n}{V_T}\right) \tag{4.6}$$

Thus by taking the natural log of both sides of Equation (4.6) and solving for the potential, yields:

$$V_n = V_T ln\left(\frac{N_D}{n_i}\right) \tag{4.7}$$

Similarly for the p quasineutral region, the electrostatic potential V_p at the edge of depletion layer can be written as:

$$V_p = -V_T ln\left(\frac{N_A}{n_i}\right) \tag{4.8}$$

Finally, the internal built-in potential V_{bi}, which forms as a result of the charge displacement, can be calculated by subtracting Equation (4.8) from Equation (4.7):

$$V_{bi} = \mathrm{V}_n - \mathrm{V}_p = V_T ln\left(\frac{N_A N_D}{{n_i}^2}\right) \tag{4.9}$$

For simplicity, inside the depletion region it is assumed that *n=p=0*, meaning that it is completely ionised. Therefore, from Equation (4.3) the following expression can be derived:

$$\frac{d^2V}{dx^2} = \left(\frac{dE}{dx}\right) = \begin{cases} \frac{qN_A}{\varepsilon_s} & -x_p \leq x \leq 0 \\ -\frac{qN_D}{\varepsilon_s} & 0 \leq x \leq x_n \\ 0 & x \leq x_n \; and \; x \geq \; x_n \end{cases} \tag{4.10}$$

where x_n and x_p represent the depletion layer widths in the *n* and *p* regions, respectively (as shown in Fig. 4.1(b)). By integrating Equation (4.10), the electrical field is given by:

$$E(x) = -\frac{qN_A\left(x_p + x\right)}{\varepsilon_s} \qquad for \; -x_p \leq x \leq 0 \tag{4.11}$$

$$E(x) = -\frac{qN_D(x_n - x)}{\varepsilon_s} \qquad for \; 0 \leq x \leq x_n \tag{4.12}$$

The electrical field can be related to the potential, *V,* since $E(x) = -\frac{dV}{dx}$. Thus, by integrating Equations (4.11) and (4.12), one gets:

$$V(x) = \frac{qN_A}{2\varepsilon_s}\left(x_p + x\right)^2 \qquad for \; -x_p \leq x \leq 0 \tag{4.13}$$

$$V(x) = V(0) + \frac{qN_D}{\varepsilon_s}\left(x_n x - \frac{x^2}{2}\right) \qquad for \; 0 \leq x \leq x_n \tag{4.14}$$

So from Equation (4.13), the potential across the p-region can be expressed as:

$$\mathrm{V}_p = \frac{qN_A {x_p}^2}{2\varepsilon_s} \tag{4.15}$$

and from Equation (4.14), the potential across n-region can be expressed as:

$$|V_n| = \frac{qN_D {x_n}^2}{2\varepsilon_s} \quad (4.16)$$

Hence, the built-in potential is given by:

$$V_{bi} = V_p + |V_n| = V(x_n) = \frac{E_m}{2}(x_p + x_n) \quad (4.17)$$

where

$$|E_m| = \sqrt{\frac{2qN_A V_p}{\varepsilon_s}} = \sqrt{\frac{2qN_D |V_n|}{\varepsilon_s}} \quad (4.18)$$

Due to the continuity of the electric field at the junction interface the following relation will be held:

$$N_A x_p = N_D x_n \quad (4.19)$$

The depletion width on either side (x_p and x_n) can be calculated by using Equations (4.17) and (4.19). Thus:

$$x_p = \left(\frac{2\varepsilon_s V_{bi}}{q} \frac{N_D}{N_A(N_A + N_D)}\right)^{\frac{1}{2}} \quad (4.20)$$

and

$$x_n = \left(\frac{2\varepsilon_s V_{bi}}{q} \frac{N_A}{N_D(N_A + N_D)}\right)^{\frac{1}{2}} \quad (4.21)$$

Consequently, the space charge width, *W*, in the p-n junction is

$$W = x_p + x_n = \left(\frac{2\varepsilon_s V_{bi}}{q} \frac{N_A + N_D}{N_A N_D}\right)^{\frac{1}{2}} \quad (4.22)$$

This equation shows that the depletion width depends on the doping density of lightly doped side. For example, if $N_A >> N_D$, thus $W \approx \left(\frac{2\varepsilon_s V_{bi}}{qN_D}\right)^{\frac{1}{2}}$. This leads to the conclusion that a larger fraction of the depletion region takes place on the side of the junction with the lower doping (for this example, in the n-side of the junction).Such a structure is known as a one-sided abrupt p–n junction [1, 2].

4.1.1 P-N JUNCTION UNDER BIAS CONDITIONS

If an external bias is applied between p and n regions, a p-n junction will be no longer in the equilibrium condition and current starts to flow through the junction. The flow of this current depends on the polarity of the applied external biases, which are either forward bias or reverse bias conditions. When a reverse bias voltage is applied, the charge carriers (electrons and holes) are pushed away from the junction, and therefore it is difficult for them to cross the depletion region. Thus, as can been seen in Fig. 4.2 (c), in the reverse-bias voltage condition, the potential barrier across the junction is increased to $(V_{bi} + V)$. In addition, the depletion width increases and consequently the current flow through the junction becomes very small. This leads to conclude that, in a reverse-bias condition, the current flows only by thermal effects. On the other hand, as can be seen from Fig. 4.2 (b), the application of a forward bias voltage lowers the potential barrier across the junction to $(V_{bi} - V)$ and decreases the depletion width. Hence, the current flow through the junction becomes very large. Moreover, Fig. 4.2 (a) illustrates that with a zero bias, the Fermi level is constant throughout the junction while when a forward bias voltage (Fig. 4.2 (b)) is applied to the diode, E_{Fn} shifts down to the half occupancy equilibrium level for holes in the p side and E_{Fp} does the reverse. Also, when a reverse bias voltage is applied to the diode, the Fermi level on the n-side of the junction is lower than the Fermi level on the p-side.

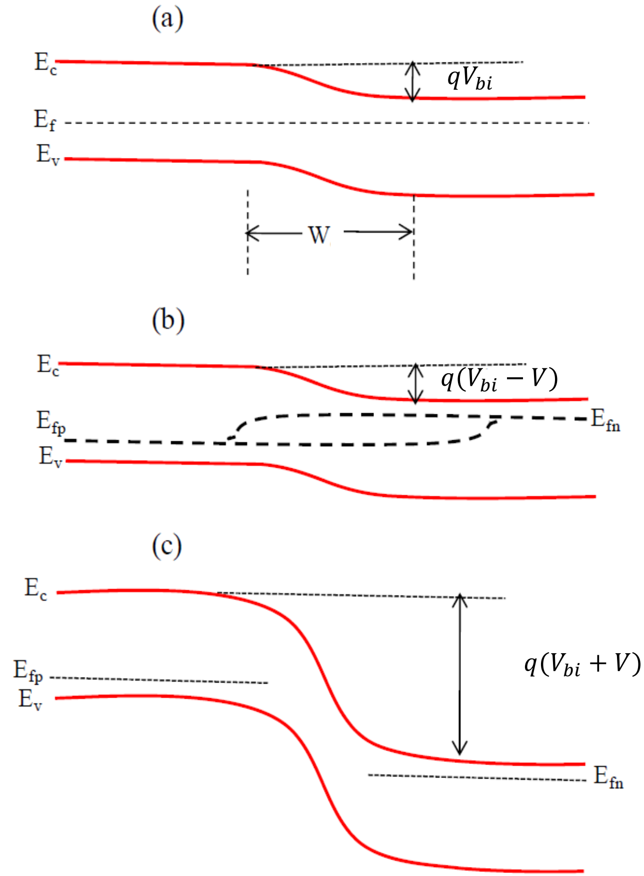

Fig. 4.2. Schematically diagram of the energy band structure of a p-n junction under (a) a zero-bias, (b) a forward bias, and (c) a reversed bias conditions [4].

By neglecting the voltage drop in p and n quasi-neutral regions and modifying the solution of the Poisson's equation at zero bias (Equation (4.22)) with $(V_{bi} \pm V)$ instead of V_{bi}, one can get the depletion width for abrupt junction under bias condition to be:

$$W = \left(\frac{2\varepsilon_s(N_A + N_D)}{qN_A N_D}(V_{bi} \pm V)\right)^{\frac{1}{2}} \qquad (4.23)$$

It is worth mentioning that, the plus and minus signs are used for reverse and forward bias conditions, respectively.

4.1.2 DEPLETION LAYER CAPACITANCE

The depletion capacitance of the space charge region is one of the most important parameter that helps to characterise and understand the p-n junction.

The measurements of the capacitance of a device as a function of reverse-bias voltages help to determine the built-in potential of a junction. Moreover, the capacitance-voltage analysis is a standard method used to estimate the carrier density profile of a Schottky diode or p-n junction [3]. The p-n junction is a double layer of positively charged donors and negatively charged acceptors. Therefore, its associated capacitance is given by [3]

$$C = \frac{dQ}{dV} = \frac{d(qN_A x_p)}{dV} = \frac{d(qN_D x_n)}{dV} \qquad (4.24)$$

where dQ is the charge in the depletion region and dV is the applied voltage. Also this capacitance can be given as a function of the junction depletion width, W , as:

$$C = \frac{A\varepsilon_s}{W} \qquad (4.25)$$

where A is the area of the junction and ε_s the permitivity of the semiconductor.

Thus by assuming $N_A \gg N_D$ and using Equations (4.24) and (4.25), the one side abrupt junction capacitance can be written as:

$$C = \frac{dQ}{dV} = \frac{A}{2}\left[\frac{2\varepsilon_s q N_D}{V_{bi} \pm V}\right]^{1/2} \qquad (4.26)$$

From Equation (4.26), it is clear that the capacitance of the diode decreases as the applied reverse bias is increased. Therefore, if the inverse of the capacitance square, ($1/C^2$) is plotted as a function of applied voltage, V , a linear relationship results as shown in Fig. 4.3. The slope of the line gives the doping concentration of the lightly doped semiconductor and the x-intercept of this plot (at $1/C^2 = 0$) yields the built-in-potential across the junction [3, 4].

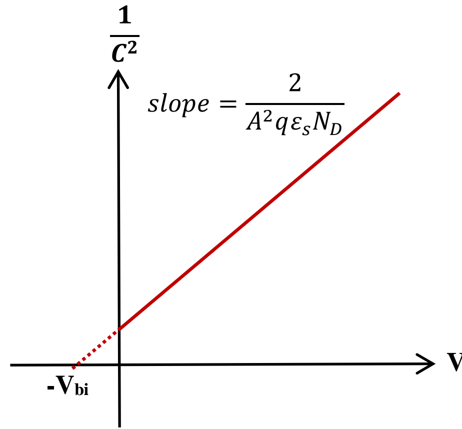

Fig. 4.3. A typical plot of $1/C^2$ versus applied reverse-bias voltage for a one step-junction diode [4].

4.2 CURRENT- VOLTAGE CHARACTERISATION

Schottky diodes or p-n junction current-voltage (I-V) characteristics can be described by the thermionic emission model with a series resistance (R_s) [4]:

$$I = I_s \left[exp \left(\frac{q(V - IR_s)}{nkT} \right) - 1 \right] \quad (4.27)$$

where q is the electronic charge, V is the applied voltage, k is the Boltzmann constant, n is the ideality factor, I_s the saturation current, and T is the absolute temperature in Kelvin. The values of n and I_s are determined from experimental data. The saturation current I_s is given by:

$$I_s = AA^{**}T^2 exp \left(\frac{-q\phi_B}{kT} \right) \quad (4.28)$$

where A is the diode area and A^{**} is the effective Richardson's constant for a semiconductor material, and ϕ_B is the barrier height.

Under forward bias for $V - IR_s >> kT$, the thermionic diode current is given by

$$I = I_s exp \left(\frac{q(V - IR_s)}{nkT} \right) \quad (4.29)$$

By taking the first derivative of I with respect to V (Equation (4.29)) will give:

$$dI/dV = I\left(\frac{q}{nkT} - \frac{\frac{qR_s}{nkT}dI}{dV}\right) \quad (4.30)$$

By rearranging the above equation and substituting dI/dV with the conductance (G) the following expression is obtained:

$$\frac{G}{I} = \frac{q}{nkT} - \frac{qR_s}{nkT}G \quad (4.31)$$

Thus by plotting the conductance divided by current (G/I) versus conductance (G) (as shown in Fig. 4.4), n and R_S can be extracted from the y-intercept and the slope, respectively.

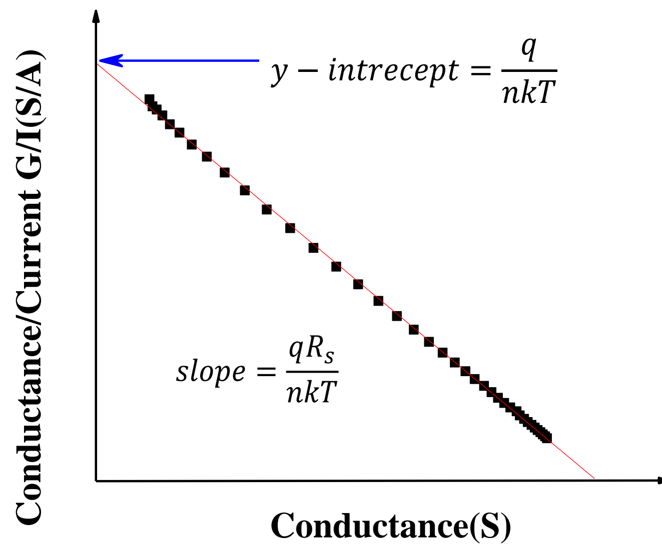

Fig. 4.4. A typical plot of G/I versus G used for extracting the I-V characteristics parameters.

For the determination of I_S and ϕ_B, the natural logarithm (ln) of Eq (4.27) is taken:

$$\ln(I) = \ln(I_s) + \frac{q(V - IR_s)}{nkT} \quad (4.32)$$

Then, by plotting $\ln(I)$ versus $(V - IR_s)$, one can get I_S from the y-intercept. Subsequently, by substituting the I_S value in Equation (4.28), ϕ_B can be calculated.

4.3 DEEP LEVEL TRANSIENT SPECTROSCOPY (DLTS)

The most widely used techniques in the study of deep level defects in semiconductors are based on microscopic defect analysis [5]. One of these techniques is deep level transient spectroscopy (DLTS), which is the most powerful microscopic tool used to characterise deep levels in semiconductors via the observation of charge carriers emission [6]. DLTS was first discovered by Lang in 1974 [7]. This technique is based on the variation of the depletion width as a function of temperature using the concept of space charge capacitance in order to find the activation energies and capture cross-sections of defects.

4.3.1 CAPACITANCE TRANSIENTS

Since the DLTS method measures the capacitance transients arising from the change in the space charge region, a junction like a Schottky diode or a p-n junction device is needed to perform such measurements. Fig. 4.5 shows the charge occupancy changes of the defect level at various bias conditions in a Schottky diode. Bias pulses are periodically applied to the diode at a fixed repetition frequency to disturb the occupancy of the defects. These pulses are repeated between reverse bias V_R and filling bias V_P (where $V_P < V_R$) with a certain filling pulse width t_p.

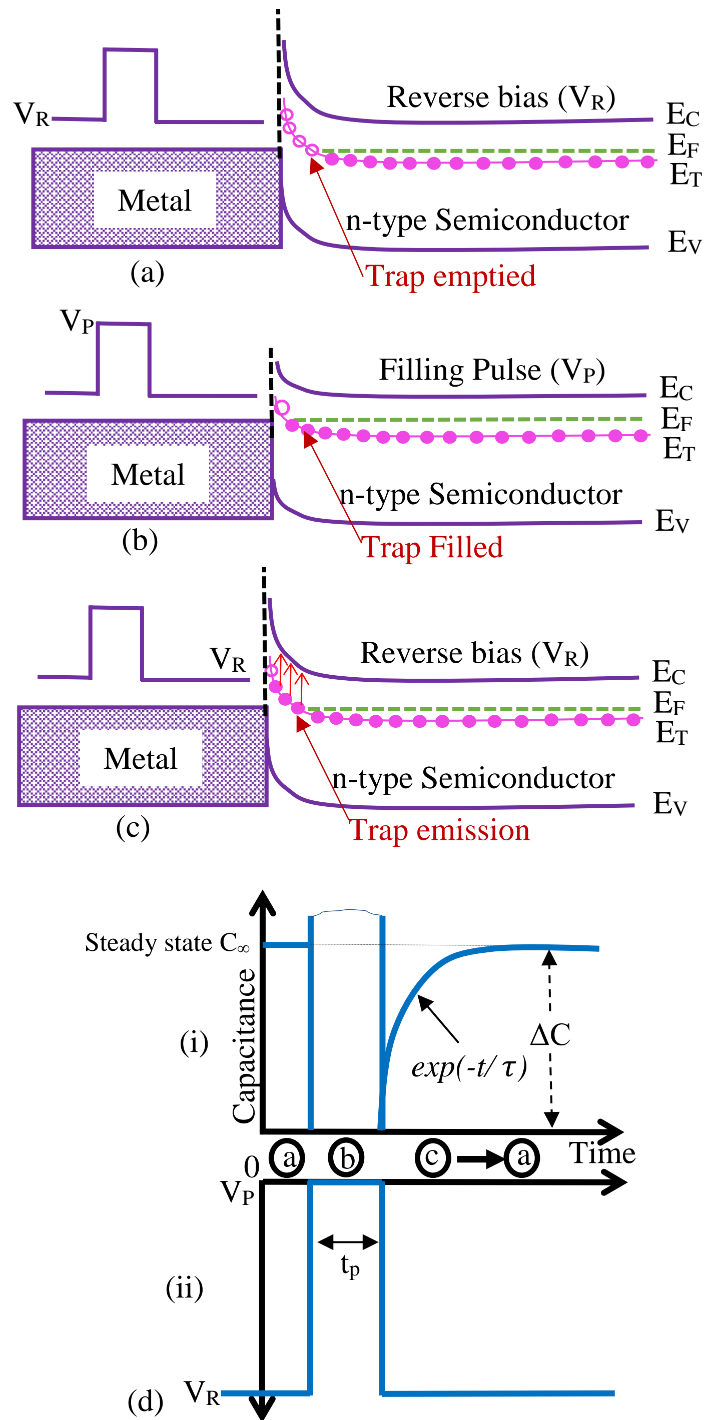

Fig. 4.5. Energy band diagrams of a Schottky diode illustrating the charge occupancy changes of the defects level during (a) emptying of traps at $V=V_R$ bias condition, (b) filling of traps with filling pulse $V=V_P$, and (c) thermal emission of electrons due to the increase in the temperature at $V=V_R$. (d) DLTS pulse and the corresponding capacitance transient. t_p and E_T represent a pulse width and a trap energy level.

Considering Fig. 4.5, at a stage (a), initially when the junction is exposed to a reverse bias V_R, a space charge region is established. The traps above the Fermi level are empty without any charge carriers. While at stage (b), when a filling pulse V_P is applied, the depletion region width decreases. Thus the electrons from the conduction band will flow to the region that was previously depleted of carriers and the traps within this region will start to capture these electrons (filled by carriers). By assuming a pure capturing processes of electrons (no emission of charge carriers) from the kinetics of capture process (Equation 3.5, Chapter 3), the rate equation for the density of filled traps is given by:

$$\frac{dn_T}{dt} = c_n(N_T - n_T) \tag{4.33}$$

where c_n, N_T and n_T represent the capture coefficient of electrons, total number of available trap states and number of trap states occupied by electrons, respectively. The electron capture coefficient is expressed by the following mathematical relation:

$$c_n = \sigma_n < v_{th} > n \tag{4.34}$$

where σ_n is the electron capture cross-section, $< v_{th} >$ is the mean thermal velocity of the electrons, and $n = N_D - N_T \approx N_D$ is the effective doping concentration.

When a long enough duration filling pulse (t_p) is applied, the traps will completely be filled by electrons so that $n_T = N_T$. However, at stage (c), after the reverse bias is re-established the depletion region moves back to its original width, and the filled traps will start to emit the carriers. The corresponding emission rate can be given from the kinetics of emission process by:

$$\frac{dn_T}{dt} = e_p N_T - n_T(e_n + e_p) \tag{4.35}$$

where e_n and e_p are electron emission and hole emission, respectively.

If the deep level is assumed to be only an electron interacting centre, then the time dependences of n_T during capture (Equation (4.33)) and emission (Equation (4.35)) processes are given, respectively, by [8],

$$n_T(t) = N_T\{1 - \exp(-c_n t)\}, \;\; c_n \gg e_n, e_p, c_p \tag{4.36}$$

and

$$n_T(t) = N_T \exp\left(\frac{-t}{\tau}\right), \;\; e_n \gg c_n, e_p, c_p \tag{4.37}$$

Where c_p is the capture coefficient of holes and τ is the inverse of the electron emission rate, i.e. $\tau = \frac{1}{e_n}$.

Thus from the above equation, the reduction of the filled trap concentration has an exponential trend with a time constant τ and gives rise to a capacitance transient as illustrated schematically in Fig. 4.5 (d).

The variation of occupancy of traps can be measured indirectly by monitoring the capacitance changes of the junction. Thus by adding the filled traps contribution, $n_T(t)$ in the space charge region, Equation (4.26) can be rewritten as

$$C = \frac{dQ}{dV_R} = \frac{A}{2}\left[\frac{2\varepsilon_s q N_D^*}{V_{bi} + V_R}\right]^{1/2} \tag{4.38}$$

where $N_D^* = N_D - n_T$.

Equation (4.38) can be expanded when $n_t \ll N_d$, as follows

$$\Delta C = C_\infty\left(1 - \frac{\mathrm{n}_T}{2N_D}\right) \tag{4.39}$$

where ΔC is the amplitude of the capacitance transient and C_∞ is the steady state capacitance that is expressed as $C_\infty = \frac{A}{\sqrt{2}}\left[\frac{2\varepsilon_s q N_D^*}{V_{bi}+V_R}\right]^{1/2}$.

By substituting Equation (4.37) into Equation (4.39), the information about the time dependence of the capacitance for majority carrier traps emission can be found from:

$$\Delta C = C_{\infty}\left[1 - \frac{N_T}{2N_D}\exp\left(-\frac{t}{\tau}\right)\right] \qquad (4.40)$$

Consequently, the amplitude of the capacitance transient and the time constant can be used to determine the deep level trap concentration and the emission rate of electrons, respectively. The trap emission process and corresponding change in the capacitance in time scale is presented in Fig. 4.5 (d).

It is worth to mention that, for minority carriers traps, the sign of the capacitance transient is opposite to the majority carrier traps.

4.3.2 CONVENTIONAL DLTS

The conventional DLTS technique principle [7] is based on perturbing the occupancy of the deep states and observing the output signal of the change of the capacitance, ΔC, between two points in time t_1 and t_2 ($t_2 > t_1$) as a result of capture and emission of carriers. Then, this transient is measured as function of temperature, T, so that a DLTS spectrum is produced, which allows the determination of the trap parameters such as its activation energy, E_T, capture cross section, σ, and density, N_T.

In particular, using Equation (4.40) the DLTS output signal as function of temperature, $S(T)$, can mathematically be expressed as:

$$S(T) = C(t_1) - C(t_2) = \Delta C_{\circ}\left[exp\left(-\frac{t_2}{\tau}\right) - exp\left(-\frac{t_1}{\tau}\right)\right] \qquad (4.41)$$

where $\Delta C_{\circ}$ is the change in the capacitance at time $t = 0$, and is given by:

$$\Delta C_{\circ} = \frac{C_{\infty} N_T}{2N_D} \qquad (4.42)$$

where N_T is the trap concentration and C_∞ is the capacitance at a maximum reverse bias (when the trap is empty). *S(T)* changes as the emission rate e_n changes with temperature as shown in Fig. 4.6 (a).

For the cases when $\tau \ll (t_1 - t_2)$ and $\tau \gg (t_1 - t_2)$, the DLTS signal will be small, while when $\tau \approx (t_1 - t_2)$ the DLTS signal will be maximum. The maximum signal of *S(T)* (maximum emission) corresponding to the maximum amplitude of the DLTS signal can be found by using $\frac{dS(T)}{d\tau} = 0$, which yields the rate window equation,

$$\tau = \tau_{max} = \frac{(t_1 - t_2)}{ln\left({}^{t_1}/_{t_2}\right)} \tag{4.43}$$

So by changing the value of the rate window τ, i.e. by changing the values of two measurement times t_1 and t_2, the DLTS peaks shift to higher temperatures as shown in Fig. 4.6 (b). Typical rate windows values are from 5 s^{-1} to 5000 s^{-1}. Consequently, a set of data of [T_{max}, e(T_{max})] is obtained to construct an Arrhenius plot as shown in Fig. 4.6 (c). The activation energy, E_T, and apparent capture cross-section, σ_n, of the trap can be extracted from the slope and intercept of the Arrhenius plot, respectively. Moreover, the trap concentration, N_T can be calculated using Equation (4.42), where $\Delta C_\circ$ corresponds to the conventional DLTS peak amplitude. It is worth pointing out that the maximum peak height of DLTS signal does not depend on the absolute value of t_1 and t_2 as clearly expressed by Equations (4.42) and (4.43), but it depends on the ratio (t_2/t_1).

In the transient process, the change in capacitance is usually very small so the DLTS measurements will be very sensitive to noise. Therefore, in order to improve the signal-to-noise ratio, the capacitance measurements are generally averaged over a number of transients.

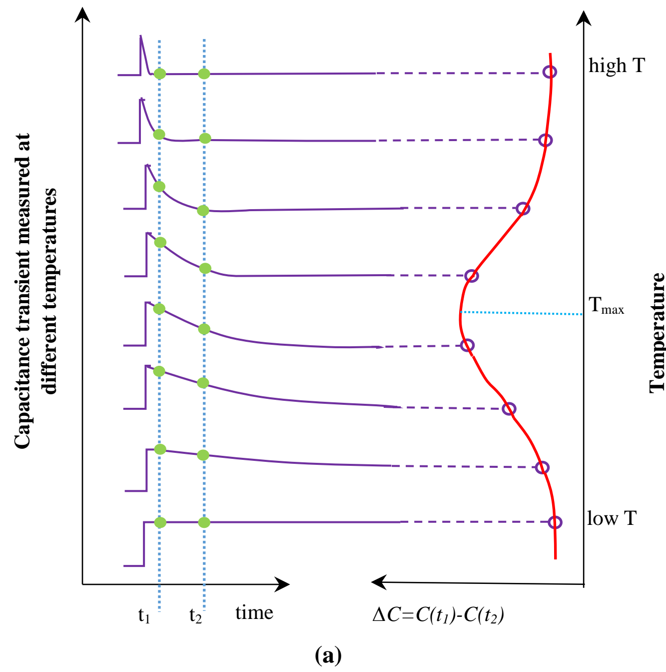

Fig. 4.6. Schematic diagram of the DLTS signal generation process: (a) the left-hand side shows capacitance transients at different temperatures, while the right-hand side shows a consistent DLTS signal resulting from the capacitance transient between the capacitance at time t_1 and time t_2 as a function of temperature, (b) signal of DLTS at different rate windows and (c) the Arrhenius plot for the calculation of trap activation energy (E_T) [7].

4.4 LAPLACE DLTS SPECTROSCOPY

Conventional DLTS technique is commonly used to characterise the deep levels in semiconductor materials [7]. It is based on producing a sequence of peaks as function of temperature. These peaks are created as a result of the exponential behaviour of the emission transient of the deep levels. However, there are many issues associated with the resolution of DLTS which arise from the scanning nature of the temperature. The accuracy of the temperature measurements associated with the thermal scanning technique is one of these issues, since the temperature of the diode changed continuously. Therefore, the accuracy of determining the activation energies will decrease. Another issue is the difficulty of separating the time constants of exponential emission transient from different defect states which leads to a broadening of the DLTS spectra peaks [9].

Thus, to overcome these limitations of the Conventional DLTS, mathematical methods have been established known as Laplace Inversion to extract the whole emission spectrum F(s) from the capacitance transient. The type of DLTS using these mathematical methods is known as Laplace DLTS (LDLTS). In this technique, the capacitance transient is averaged and measured at a fixed temperature, which makes the LDLTS to be an isothermal technique [9, 10]. Moreover, in this technique the DLTS signal is converted from time domain (conventional DLTS mode) to the frequency domain. In order to increase the signal to noise ratio, different digital schemes are used to digitize and to average the analogue transient output of the capacitance meter during the emission process [11]. The mathematical description of the LDLTS transient can be expressed using the Laplace equation:

$$f(t) = \int_0^\infty F(s)e^{-st}ds \tag{4.44}$$

where $f(t)$ is the recorded transient and $F(s)$ is the spectral function. So $f(t)$ is the Laplace transform of the true spectral function $[F(s)]$. Fig. 4.7 (a) shows an example of the capacitance transient that can be obtained from Laplace DLTS. In order to get a real spectrum of the emission rates present in the transient, $f(t)$, mathematical algorithms which apply the inverse Laplace transform for the function $f(t)$ are selected. FLOG, CONTIN and FTIKREG are the three mathematical algorithms implementations of Laplace Inversion that have been used in the Laplace technique. Only one routine is used to analyse the data. All of these algorithms are based on the Tikhonov regularisation method. However, each one of them has a different principle to find and define the regularisation parameters. The first algorithm (CONTIN) [12] and the second algorithm (FTIKREG) [13, 14] codes are obtained from The Computer Physics Communication (CPC) Program Library at the Queen's University of Belfast. Both of these algorithms have been modified for use in Laplace DLTS system. However, the last algorithm (FLOG) has been specifically established for the system. It is worth to mention that the parallel use of the three numerical algorithms increase the confidence level in the spectra obtained. Furthermore, the output of this technique gives a very well-defined, delta-like peaks spectra for multi-exponential transients as a function of emission rates as shown in Fig. 4.7 (b). Also, the trap concentration can be found from the area under the peaks of LDLTS signal. Hence, the precision of the characterization of defects increases [10].

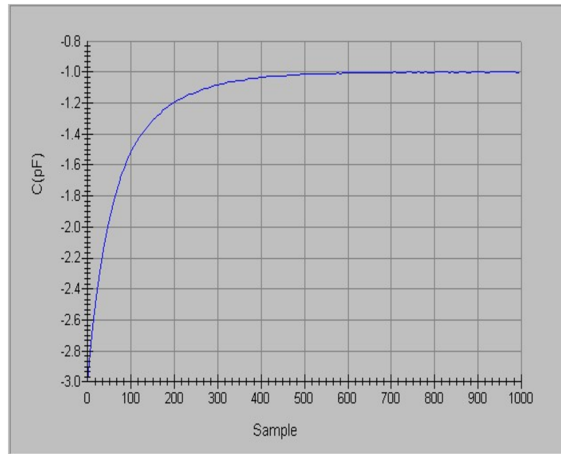

(a)

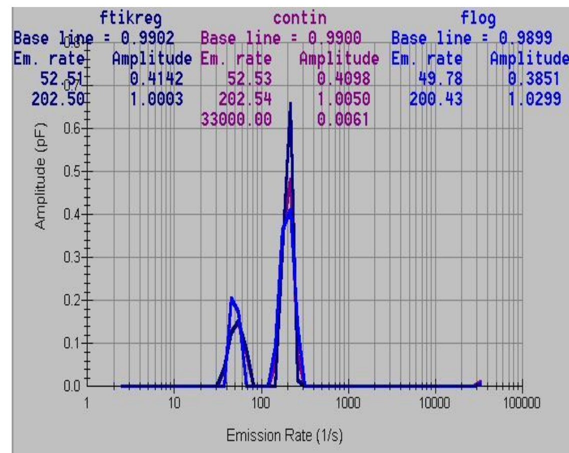

(b)

Fig. 4.7. (a) Diagram of the capacitance transient using Laplace DLTS at fixed temperature; (b) delta-like peaks spectra output obtained from the capacitance transient with the use of three numerical routines.

Fig. 4.8 shows the ability of the high resolution LDLTS technique to resolve the signal of conventional DLTS for very closely spaced defects. In this figure, conventional DLTS reveals the present of only one broad peak in hydrogenated Si sample containing gold [15]. However, the LDLTS measurements reveal two well resolved peaks correlated to hydrogen and gold related defects.

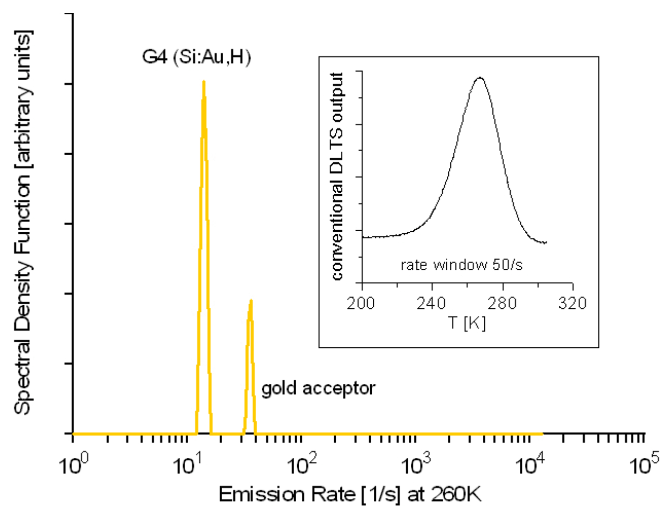

Fig. 4.8. LDLTS spectra of hydrogenated Si containing gold at 260 K. The inset shows the conventional DLTS spectrum at a rate window of 50 s^{-1} [15].

4.5 SYSTEM HARDWARE IMPLEMENTATION

4.5.1 DESCRIPTION OF SYSTEM HARDWARE

This section covers the main experimental setup used to perform the conventional DLTS and Laplace DLTS measurements. Fig. 4.9 illustrates the block diagram of DLTS and Laplace DLTS setup which consists of (I) Janis cryostat and temperature controller, (II) capacitance meter, (III) Current-Voltage meter, (IV) data acquisition and BNC connectors box for analogue Input (I)/Output (O). A computer is used to control all these equipment via a GPIB interface.

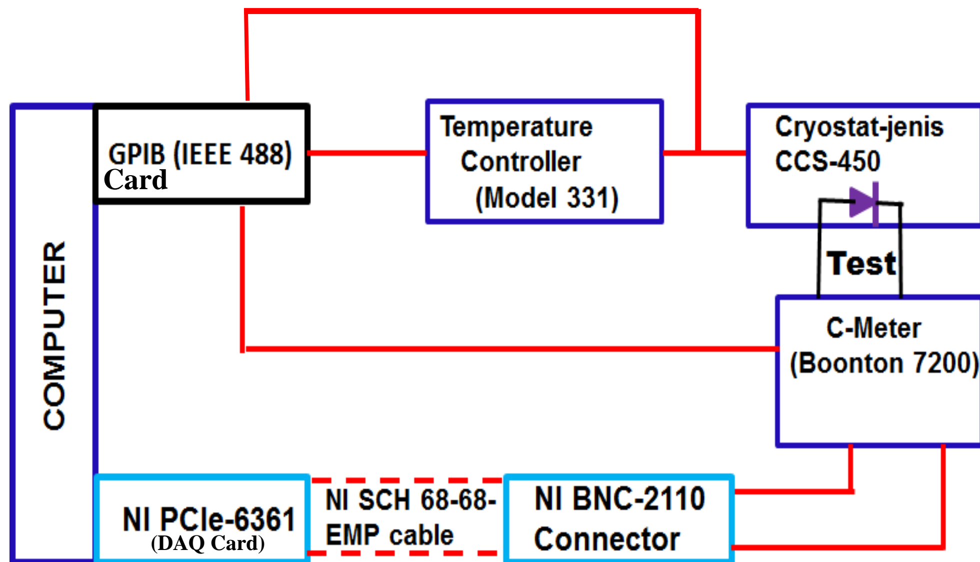

Fig. 4.9. Block diagram of DLTS and Laplace DLTS system.

4.5.1.1 CRYOSTAT AND TEMPERATURE CONTROLLER

The process of emitting charge carriers from the traps depend on the thermal energy. Thus, in DLTS and Laplace DLTS measurements a cryostat (model Janis CCS-450) and a temperature controller (Model Lake Shore 331) are used to control and to monitor the sample temperature.

Fig. 4.10 illustrates the internal structure of the cryostat system. In particular, this system consists of a sample holder connected to a cold finger, thermal sensors, electrical ports for sample contacts, a radiation shield and aluminium vacuum shroud. This cryostat operates with a compressor that has a closed cycle refrigeration system with a continuous flow of helium gas (He) through a high efficiency flexible six feet cryogen transfer line. The cryostat, which is controlled by Lake Shore 331, operates over the temperature range 10 K - 450 K with a good stability of ±1 K. Lake Shore 331 is connected to a temperature sensor located very close to the sample for high temperature accuracy.

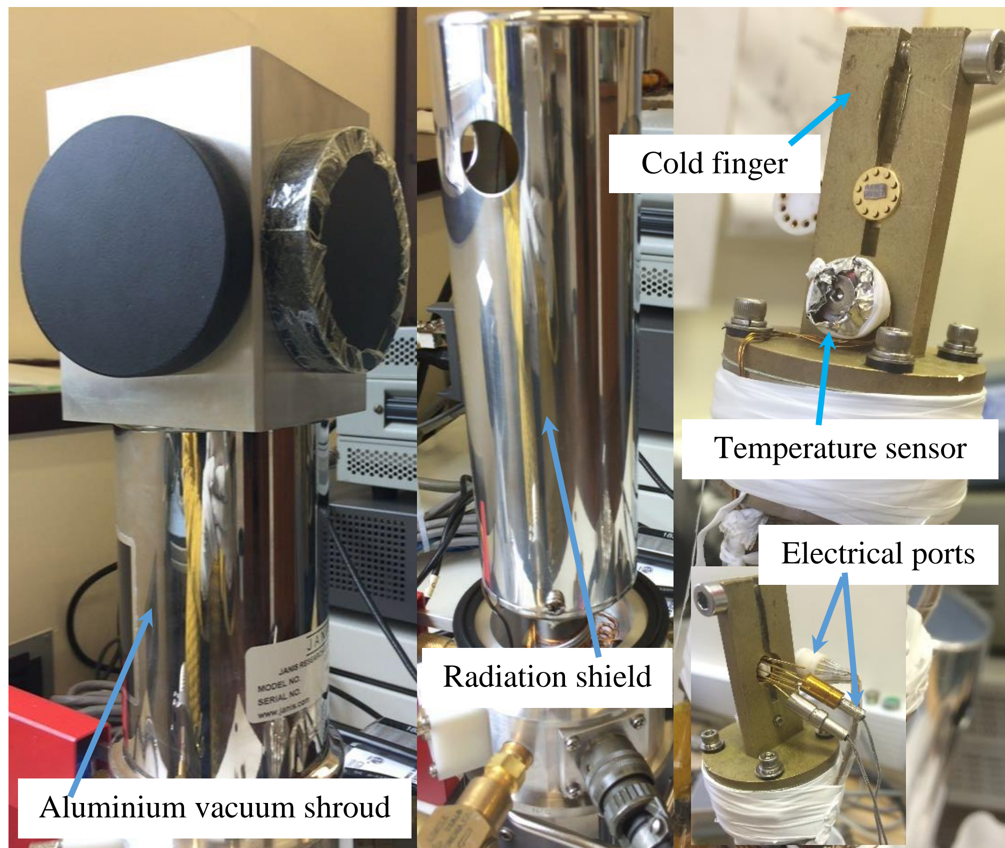

Fig. 4.10. Photograph of the external and internal structure of the cryostat system (model Janis CCS-450) used for the DLTS experiments.

4.5.1.2 CAPACITANCE METER

In order to measure the capacitance transient in DLTS measurements, a high response time capacitance meter is needed. The capacitance Boonton 7200 meter has a response time of ~120 μs that makes this meter a good choice for these measurements. Moreover, this meter is used for normal C-V measurements at different temperatures. It is worth to mention that this meter has only 1 MHz sampling frequency.

4.5.1.3 CURRENT-VOLTAGE SOURCE METER

Capacitance-based DLTS and Laplace DLTS techniques require samples with low leakage currents in the range of μA. The current-voltage (I-V) measurements are performed using Keithley 236 current meter which is controlled by a computer software via GPIB interface. This meter provides a source voltage in the range of 100 μV to 110 V with a sensitivity of ±10 μV and a source current in the range of 100 fA to 100 mA, with a sensitivity of 10 fA.

4.5.1.4 DATA ACQUISITION AND BNC-2100 CONNECTOR

In order to bias and pulse the diodes, a National Instruments (NI) data acquisition (DAQ) card is used. Through this card an input voltage up to ± 10.0 V and with pulse width from 0.5 μs can be applied to the samples. The SHC68-68-EPM matching cable is used to interface the DAQ card with the BNC-2110 connector which connected to the computer.

4.5.1.5 COMPUTER INTERFACE

High speed general-purpose interface bus (GPIB) is used to connect all the experimental equipment with the computer to control them remotely through software.

4.6 SYSTEM SOFTWARE

Laplace DLTS software is developed under the joint project *"Copernicus Project CIPA CT-94-0172 and The Foundation for Polish Science Serial No: C3.2.041"* between Institute of Physics Polish Academy of Sciences, Warsaw, Poland (the late Prof. L. Dobaczewski) and University of Manchester (Prof. A. R. Peaker). This

software can work in conventional DLTS and Laplace DLTS modes as describe below.

4.6.1 CONVENTIONAL DLTS MEASUREMENTS MODE

In conventional DLTS measurements mode, the sample is scanned by continuously varying the temperature. The temperature is set normally in a determined range between two points with increasing steps of 2K/minute. The measurement can be performed using Multi-Rate Window, TrapView and Exponential Fitting modes. All these modes run on the principle of rate window and are discussed briefly below.

In the "Multi-Rate" mode nine different rate windows can be used, namely 5 s^{-1}, 10 s^{-1}, 20 s^{-1}, 50 s^{-1}, 100 s^{-1}, 200 s^{-1}, 500 s^{-1}, 1000 s^{-1} and 2000 s^{-1}. In the "TrapView" mode, one pair out of 5 different pairs of rate windows can be selected at a time: (4, 10 s^{-1}), (20, 50 s^{-1}), (80, 200 s^{-1}), (400, 1000 s^{-1}) and (2000, 5000 s^{-1}). On the other hand, only one rate window can be used in the "Exponential Fitting" mode. When the measurement is run in "Exponential Fitting" mode, the Arrhenius plot is established. Thus, defects activation energies and capture cross-section can be estimated. In addition, this mode can be also work in lock-in mode which has a better resolution than the rate window mode. However, lock-in mode has a poor signal to noise ratio.

It is worth to mention that the DLTS experiment parameters such as the reverse bias, forward bias, duration of pulses and temperature range can be set remotely in all these three modes.

4.6.2 LAPLACE TRANSIENT PROCESSING MODE

In order to increase the S/N ratio, the Laplace DLTS is used. As discussed before in section 4.4 this measurement is performed at constant temperature. In order to determine the Laplace DLTS peaks FLOG, CONTIN and FTIKREG algorithms are used.

4.7. PHOTOVOLTAIC CELL AND BETAVOLTIC BATTERY

In a photovoltaic cell or a solar cell, the energy of sunlight is converted directly into electricity as illustrated in Fig. 4.11 (a). In particular when photons strike a semiconductor p-n junction, electron-hole pairs (EHPs) will be generated causing an electrical current to flow.

In betavoltaic (β) battery, the energy of beta radiation of a radioactive material is converted into electricity. It is worth to mention that a betavoltaic battery has a similar operation principle to that of a photovoltaic cell. In betavoltaic cells, when energetic beta electrons emitted from the radioactive source strike the p-n junction diode, EHPs are generated as shown in Fig 4.11 (b). Hence causing an electrical current to flow [16].

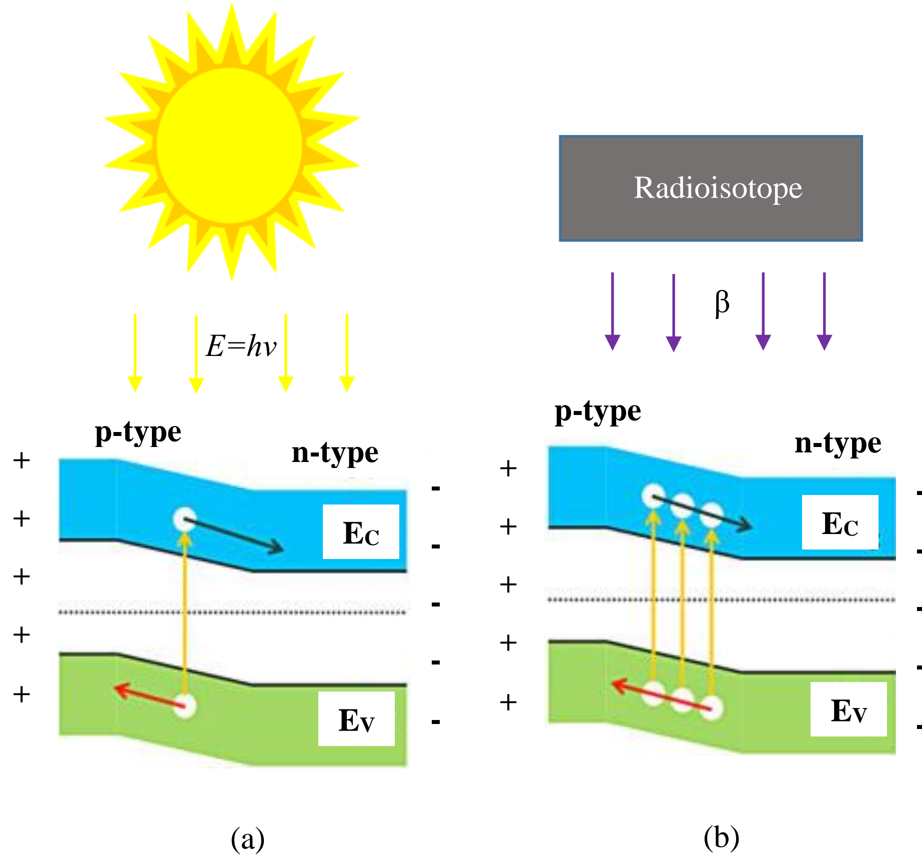

Fig. 4.11. Operation principle of (a) a solar cell and (b) a betavoltaic battery. *E and ν* are energy and frequency of the photon. β is beta radiation of a radioactive material [16].

The power conversion efficiency (η) of a solar cell and a betavoltaic battery is defined as the fraction of incident power which is converted to electricity and is calculated by:

$$\eta = \frac{FF\times V_{OC}\times I_{SC}}{P_{in}}\times 100\% \quad (4.45)$$

where FF,V_{OC}, I_{SC} are the fill factor, open-circuit voltage, and the short-circuit current, respectively. These parameters are extracted from the cell output current-voltage curve as shown in Fig. 4.12. P_{in} in a solar cell is the power density of incident light and it is defined as

$$P_{in} = E\times A_C \quad (4.46)$$

where E and A_C are incident radiation flux (W/m^2) and area of cell (m^2), respectively. While, P_{in} in a betavoltaic battery is calculated by using the following equation.

$$P_{in} = qN_0E_\beta \qquad (4.47)$$

where N_0 and E_β represent, respectively, the number of beta particles emitted by the source per cm^2 of the device area and the average beta particle energy [17].

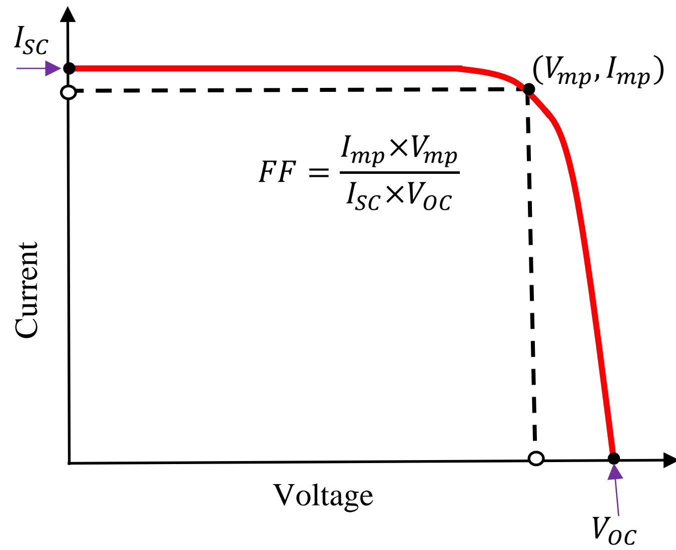

Fig. 4.12. Cell output current as function of voltage. (V_{mp}, I_{mp}) is the maximum power point.

REFERENCES

[1] B. G. Yacobi, *Semiconductor materials: an introduction to basic principles*. (Springer, 2003).

[2] J.-P. Colinge and C. A. Colinge, *Physics of semiconductor devices*. (Springer, 2002).

[3] D. A. Neamen and B. Pevzner, *Semiconductor physics and devices: basic principles*. (McGraw-Hill New York, 2003).

[4] S. M. Sze and K. K. Ng, *Physics of semiconductor devices*. (John Wiley & Sons, 2006).

[5] S. Pandey, P. Middelkamp, Z. Li and V. Eremin, Nuclear Instruments and Methods in Physics Research Section A: Accelerators, Spectrometers, Detectors and Associated Equipment **426** (1), 109 (1999).

[6] A. Peaker and M. Brozel, III-Vs Review **12** (1), 44 (1999).

[7] D. Lang, Journal of Applied Physics **45** (7), 3023 (1974).

[8] D. K. Schroder, *Semiconductor material and device characterization*. (John Wiley & Sons, 2006).

[9] L. Dobaczewski, I. Hawkins and A. Peaker, Materials Science and Technology **11** (10), 1071 (1995).

[10] L. Dobaczewski, A. Peaker and K. B. Nielsen, Journal of Applied Physics **96** (9), 4689 (2004).

[11] L. Dobaczewski, P. Kaczor, I. Hawkins and A. Peaker, Journal of Applied Physics **76** (1), 194 (1994).

[12] S. W. Provencher, Computer Physics Communications **27** (3), 213 (1982).

[13] J. Weese, Computer Physics Communications **69** (1), 99 (1992).

[14] J. Weese, Computer Physics Communications **77** (3), 429 (1993).

[15] P. Deixler, J. Terry, I. Hawkins, J. Evans-Freeman, A. Peaker, L. Rubaldo, D. Maude, J. Portal, L. Dobaczewski and K. B. Nielsen, Applied Physics Letters **73** (21), 3126 (1998).

[16] V. Bormashov, S. Troschiev, A. Volkov, S. Tarelkin, E. Korostylev, A. Golovanov, M. Kuznetsov, D. Teteruk, N. Kornilov and S. Terentiev, physica status solidi (a) **212** (11), 2539 (2015).

[17] L. C. Olsen, (1993).

CHAPTER 5: EXPERIMENTAL DETAILS

The purpose of this chapter is to give a brief description of the samples used in this study. The experimental setup and equipment used for the measurements carried out for the electrical and optical characterization of semiconductor materials will be briefly presented.

5.1 SAMPLES USED IN THIS STUDY

The main motivation of this thesis is to investigate the electrical active defects present in different materials and devices for photovoltaic and betavoltaic applications and to study the effect of these defects on the electrical properties of these devices.

In this thesis three different kinds of materials have been investigated using different structures:

(i) GaAs p-n, GaAs p-i-n, undoped GaAs p-i-n with one dimensional InGaAs quantum wires, and n-type Si δ- doped GaAs p-i-n with one dimensional InGaAs quantum wires solar cell structures are used to investigate the electrically active defects in order to understand the physical phenomena that affect the conversion efficiency.

(ii) Dilute GaAsN samples with nitrogen concentrations ranging from 0.2 to 1.2% are irradiated with a gamma (γ-) cell Cobalt Irradiator (dose rate of 5.143 KGy/hour) at a high dose of 50 kGy to observe the effect of γ-irradiation on post-irradiation stability.

(iii) GaN p–i–n homojunction structures with the undoped intrinsic layer (i-GaN) having thicknesses of 200 nm and 600 nm are used to study the

effect of beta particle irradiation (electron energy 0.54 MeV) on the electrical properties of these devices.

The growth details of each set of samples are given in each associated experimental chapter.

5.2 MEASUREMENT DETAILS

This section gives the details of the experimental setup and equipment used for the measurements in this thesis.

5.2.1 I-V MEASUREMENTS

For this study, the devices should have low leakage currents in the range of μA or below to perform DLTS and Laplace DLTS measurements because these techniques are based on the transient of the capacitance. The I-V characteristics for the devices are measured by using a Keithley 236 source measure unit which is controlled by a computer software via GPIB interface. The current values are measured in reverse biases voltages ranging from -1 to -5 V depending on the diode quality with an increment of 10 mV.

5.2.2 C-V MEASUREMENTS

In order to determine the built-in voltage, the background doping concentration, depletion layer, interface states and concentration depth profile of the semiconductor materials, the C-V characteristics are obtained using a Boonton 7200 capacitance meter which operates at a fixed frequency of 1MHz and controlled by a computer. Moreover, as described in Chapter 4, the C-V characteristics are used to calculate the trap concentration.

5.2.3 DLTS MEASUREMENTS

The electrical active defects present in the material systems investigated in this thesis are characterised by DLTS and Laplace DLTS techniques, which are discussed in Chapter 4. In this section a brief description of the experimental procedures are presented. Firstly, the samples are processed in the form of circular mesas with different diameters, and mounted on a 12 pins TO5 headers which are fixed into a holder inside a closed cycle cryodyne refrigerator, model number CCS-450 cryostat. The samples are cooled down to a temperature of 10 K and the DLTS measurements start by increasing the temperature at a rate of 2 K/min up to 450 K. A National Instrument Box generates a sequence of electrical pulses that are applied to the samples, and a Boonton 7200 capacitance meter is used to monitor the transient capacitance. At selected reverse bias (V_R) and filling pulse (V_P), the change in capacitance transient is recorded in the form of DLTS signal and stored in computer.

5.2.4 LAPLACE DLTS MEASUREMENTS

In order to resolve the broad feature detected in the conventional DLTS peaks, high resolution Laplace DLTS measurements were carried out. The temperature of the sample is fixed during the Laplace DLTS measurements as it is an isothermal process. Within the temperatures range of the conventional DLTS peak, the Laplace DLTS measurements are performed. Further details of these measurements are explained in Chapter 4.

CHAPTER 6: INVESTIGATION OF ELECTRICALLY ACTIVE DEFECTS IN InGaAs QUANTUM WIRES INTERMEDIATE BAND SOLAR CELLS USING DEEP LEVEL TRANSIENT SPECTROSCOPY (DLTS) TECHNIQUE

This Chapter presents a detailed study of the effect of electrically active defects on the electrical properties of a set of GaAs (311)A solar cell structures gown by molecular beam epitaxy (MBE) using Current - Voltage (I-V), Capacitance - Voltage (C-V), conventional Deep Level Transient Spectroscopy (DLTS) and Laplace DLTS measurements in the temperature range from 10 K to 450 K.

6.1 INTRODUCTION

In a photovoltaic semiconductor device, the inability to absorb light with energy less than the bandgap and the energy loss of photons with energies exceeding the bandgap as heat are considered to be the main fundamental effects that limit its efficiency [1].

Recently, the social interest in exploiting solar energy using the photovoltaic effect has led to a tremendous increase in the demand for solar cells. Therefore, it is essential to develop new technologies and concepts of producing solar cells in order to increase their efficiency. In 1961, William Shockley and Hans Queisser calculated the maximum theoretical efficiency limit of a p-n junction based photovoltaic solar cells to be 30% for an optimized semiconductor bandgap of 1.1 eV. This limit is known as Shockley–Queisser limit or the detailed balance limit of efficiency [2]. This formalism has been used by many authors to model solar cells

[1]. Consequently, different approaches have been proposed and attempted in order to exceed the efficiency of solar cells above that limit. Tandem solar cells, multiband solar cells, hot carriers solar cells, intermediate level solar cells, impurity level solar cells, and quantum well solar cells are all good examples of these approaches [3].

In 1997, Luque *et al.* [4] theoretically predicted the intermediate band solar cells (IBSC) to increase the efficiency of solar cells up to 63.1% under maximum concentrated sunlight. As shown in Fig. 6.1 (a), the main principle of these cells is to introduce one or more electronic bands (called intermediate bands or levels) inside the main bandgap of a conventional semiconductor. This band should be half-filled with electrons so that it supplies both electrons to be pumped to the conduction band (CB) and empty states to receive electrons from the valence band (VB) [5]. Thus, extra absorption of photons will be created in addition to the absorption of conventional photons (transition (III) in Fig. 6.1 (a)). These extra absorptions occur through transitions from the VB to the intermediate band (IB) [transition I in Fig. 6.1 (a)] and from the IB to the CB transition II in Fig. 6.1 (a)]. Hence, the intermediate band solar cells are expected to have an increase in photocurrent [6] without voltage degradation [5].

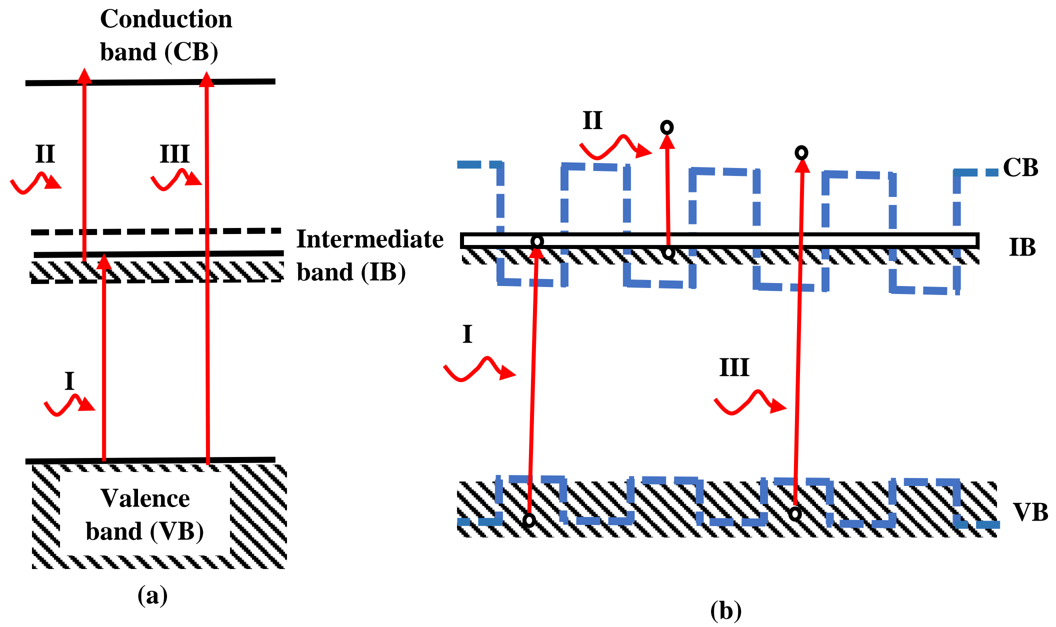

Fig. 6.1. Illustrations of (a) the principle of an intermediate band solar cell (IBSC) showing different optical transitions; (b) Basic structure of the QD-IBSC [5].

The fabrication and investigation of IBSC-based devices have received considerable interest worldwide because of their relevance in enhanced efficiency solar cells [7]. One approach to implement IBSCs is to incorporate QDs into a standard solar cell as shown in Fig. 6.1 (b). In this technique, a layer of QDs is inserted between the bandgap of the conventional semiconductor so that charge carriers are quantum confined in three directions. Consequently, this allows QDs, which have a discrete delta-like density of states, to create the required intermediate band that has a separate quasi-Fermi level from the conduction and valence band of the semiconductor [8]. However, the incorporation of QDs leads to a reduction of the photoelectrical conversion efficiency (PCE) of QD IBSC due to the formation of strain and resulting dislocations which lead to the deterioration of the open-circuit voltage, V_{oc} [9-11]. To increase the PCE of QD IBSC, insertion of δ-dopants into the QDs was proposed [12, 13]. By using n-type δ- dopants, the

electron intersubband quantum dot transitions will be increased, the recombination losses through QDs will be decreased as a result of the reduction of electron capture processes, and the deterioration of V_{oc} will be inhibited. Hence, this will enhance the infrared (IR) absorption and the photocurrent in QD IBSC [12, 13].

Kunets *et al.* [7, 14] used the above principle to fabricate an IBSC device consisting of one dimensional InGaAs quantum wires (QWRs) structure instead of using zero-dimensional quantum dots (QDs) or two-dimensional quantum wells (QWs). The QWRs were inserted into a GaAs p-i-n junction. The QWRs structure has a good configuration that allow the device to have more efficient light absorption compared to zero-dimensional systems [7]. Moreover, photocurrent can be generated in the plane of the QWRs [15, 16]. In addition, QWRs are expected to have appropriate life-time of photo-generated carriers [7]. Kunets *et al.* [7, 14] also studied the effects of n-type Si delta doping on the external efficiency of this QWRs-based IB solar cell structure. They observed that at room temperature the solar energy conversion efficiency of a reference p-i-n solar cell sample was 4.5%, whereas samples which incorporated QWRs and delta doping showed an increase of the efficiency up to 5.1% and 5%, respectively. However, they reported that the short circuit current increases and causes a comparatively lower open circuit voltage, V_{oc} (20-50 mV) which results in a severe degradation of the performance of the solar cell.

In this chapter, a detailed investigation is carried out on electrically active defects in a set of (311)A GaAs solar cell structures gown by molecular beam epitaxy (MBE) in collaboration with Kunets *et al.* [7, 14]. The devices investigated are p-n (labelled PN, first reference sample), p-i-n (labelled PIN, second reference sample), undoped p-i-n with InGaAs quantum wires consisting of closely packed QDs

aligned along the [-233] (labelled QWR undoped) and Si δ- doped p-i-n with InGaAs quantum wires (labelled QWR doped). This study will help to get a better understanding of the physical phenomena that affect the efficiency of the above solar cell structures using current density-voltage (J-V), capacitance-voltage (C-V), conventional DLTS and Laplace DLTS characterisation techniques.

6.2 SAMPLE DETAILS

The detail of samples growth is given elsewhere [7]. In summary, a solid source MBE 32P Riber system was used to grow the devices on semi-insulating (311)A GaAs substrates. It is well known that the high index (311)A plane is a good template for the growth of QWRs. Also, in this plane a strong built-in piezoelectric field can be generated in the presence of strain [17]. The first GaAs p-n reference device (PN device, SE159) consisted of a 400 nm undoped GaAs buffer layer grown at a growth temperature of 580 ºC. Then the growth temperature was decreased to 540 ºC and a 1 µm thick GaAs layer doped with Si was deposited with high V/III flux ratio (V/III=20). This low growth temperature and high V/III flux ratio make the GaAs layer achieve a high n-type doping efficiency on the (311)A surface. This was followed by a 1 µm thick p-type GaAs layer doped with Si grown at a higher growth temperature (580 ºC) and low V/III flux ratio (V/III=7) to achieve p-type conductivity. The second reference device (PIN device, SE164), which was grown using the same growth conditions and consisted of the same layers as the PN device, has an additional 330 nm thick GaAs intrinsic region grown at 540 ºC and sandwiched between the p and n layers. The third device (QWR undoped device, SE160) which was grown by incorporating an intermediate band in the GaAs i-region without any intentional doping. The i-region consisted of 10

periods of 11 monolayers of $In_{0.4}Ga_{0.6}As$ QWRs separated by a 30 nm GaAs barriers. The InGaAs quantum wires were grown at 540 ° C. Finally, the fourth device is similar to the third device structure, but in the middle of each 30 nm thick GaAs barrier, a Si n-type δ-doping with a sheet concentration $N_{2D}=1x10^{11}$ cm^{-2} (QWR doped, SE162) was inserted. In all the above structures, the doping concentration of n-type and p-type GaAs layers was 5x 10^{17} cm^{-3} and 1x 10^{17} cm^{-3}, respectively. The samples were processed in circular mesas having diameters of 900 µm, 400 µm, 549 µm and 400 µm for PN, PIN, QWR undoped and Doped QWR devices, respectively. These mesas were formed by wet chemical etching down to the n-type GaAs contact layer and 75nm AuGe/15nm Ni/200nm Au was deposited to form an O-ring shaped n-type contact. The top circular mesa p-type contact consisted of 100nm AuZn/200nm Au. The n and p contacts were annealed at 420 ºC for 2 minutes and 350 ºC for 30 seconds, respectively, using Rapid Thermal Annealing (RTA) technique. The schematic diagrams of the solar cell devices investigated in this study are shown in Fig. 6.2.

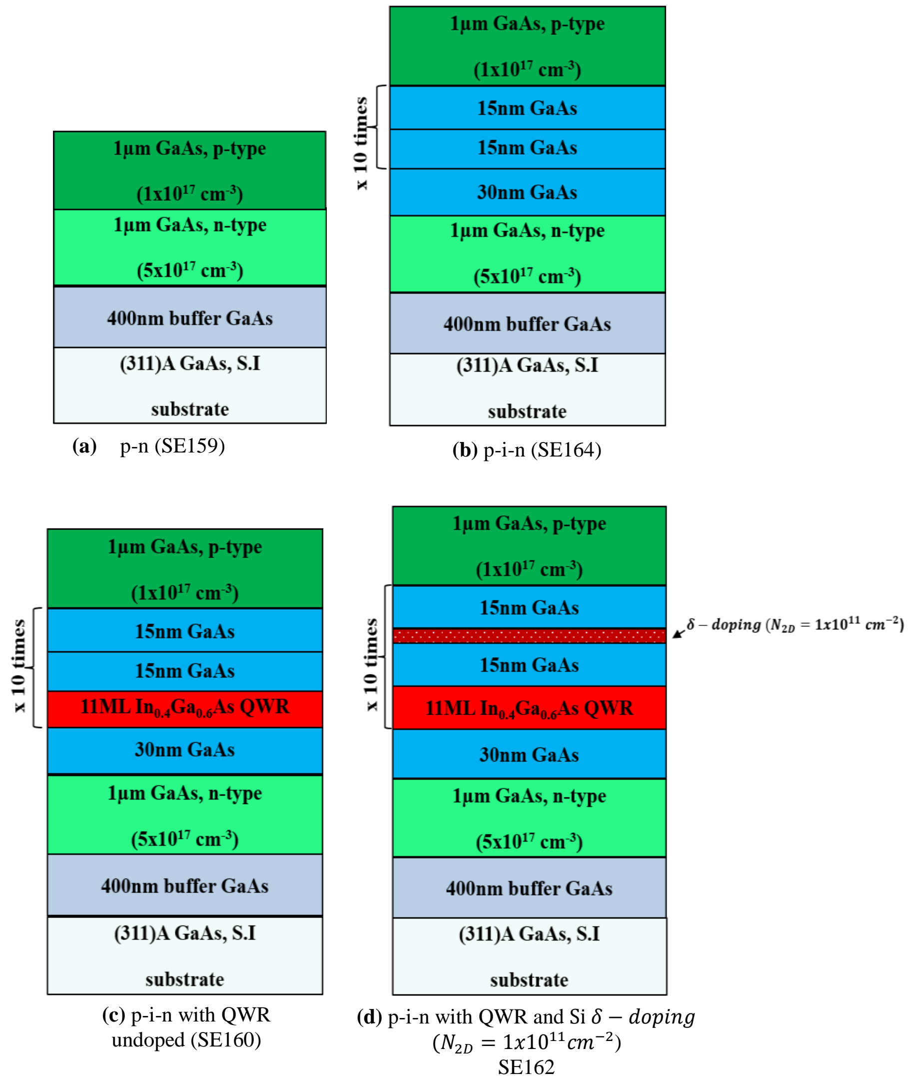

Fig. 6.2. Schematic diagram of the solar cell structures (a) Reference p-n device (PN); (b) p-i-n device (PIN); (c) undoped p-i-n with QWR device (QWR); (d) n-type Si δ-doped p-i-n with QWR (QWR Doped).

Atomic-force microscopy (AFM) was used by Kunets *et al.* [7, 14] to investigate the structural quality of the QWRs. Fig.6.3 (a) illustrates an AFM topography image showing that the InGaAs wires are aligned along the $[\bar{2}33]$ crystallographic direction. A cross-sectional surface profile was measured across the wires (along the crystallographic direction $[01\bar{1}]$) to determine the height of the wires which was to be ~ 4 nm (see Fig. 6.3 (a)).

Fig. 6.3 (b) shows the energy band diagram of a p-i-n GaAs junction at thermal equilibrium with 10 periods of InGaAs QWRs inserted in the GaAs i-region (spacer).

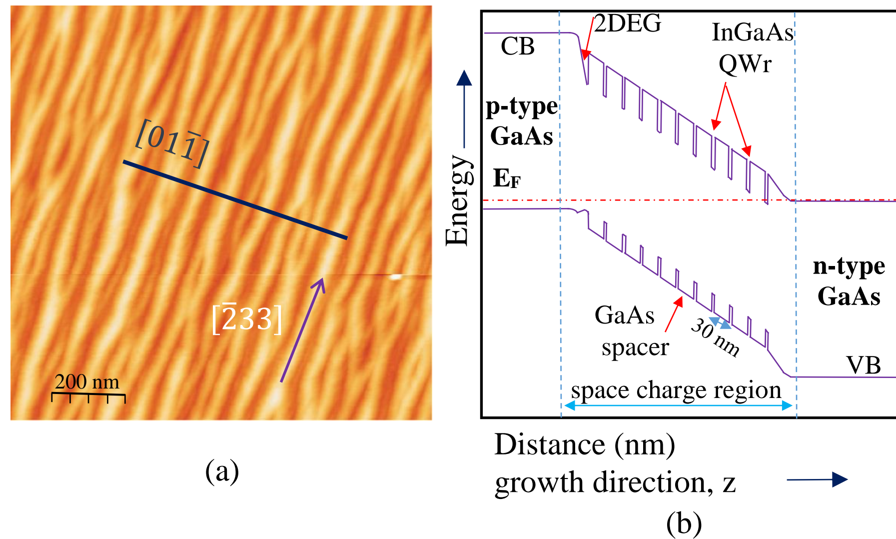

Fig. 6.3. (a) AFM topography image of the $In_{0.4}Ga_{0.6}As$ QWRs grown on the (311)A GaAs plane [7] and (b) energy band diagram of a p-i-n junction with 10 periods of QWRs at thermal equilibrium [14].

6.3 RESULTS AND DISCUSSION

I-V, C-V, DLTS and Laplace DLTS techniques were performed in order to investigate the electrically active defects present in the GaAs based solar cells described in Fig. 6.2.

6.3.1 INVESTIGATION OF THE CURRENT DENSITY (J) – VOLTAGE (V) CHARACTERISTICS AS FUNCTION OF TEMPERATURE

Fig. 6.4 (a) and Fig. 6.4 (b) show the room temperature semi-logarithmic and linear *J-V* plots of all devices, respectively. From the room temperature *J-V* characteristics

it is clear that the inclusion of an i- region (PIN) and undoped InGaAs wires (QWR undoped) enhance the performance of the devices as compared to the reference PN devices. On the other hand, introducing n-type Si δ–doping (QWR doped) leads to a deterioration of the performance of the devices. As shown in Fig. 6.4 (a), at a reverse bias of -4 V, there is one order magnitude reduction in the leakage current density in the QWR undoped devices compared to the PIN devices and two orders of magnitude when compared to the reference PN devices. However, the QWR doped samples have the highest dark current density at all reverse bias voltages amongst all devices. The decrease or increase in the leakage current, which could be attributed to a decrease or increase of the number of defects and their concentrations, will be further investigated using DLTS experiments. Furthermore, the QWR undoped devices have the lowest forward current density as compared to all the other devices. However, Hao Feng Lu *et al.* [18] reported an increase of the forward current density at 310 K when incorporating $In_{0.5}Ga_{0.5}As$ quantum dots to GaAs p-i-n solar cells grown on n^+ GaAs (001) substrates by metal organic chemical vapour deposition. They related this behaviour to the creation of additional recombination paths via QD states as a result of the presence of QDs in the depletion region. Moreover, as can be seen from Fig. 6.4 (b), the QWR undoped devices have a turn-on voltage (V_{on}) of 0.77 V, which is higher than the V_{on} of the PIN devices (V_{on} ~ 0.68 V). This behaviour can be explained by the creation of new defects states in the undoped i-region where the QWRs are incorporated. However, the QWR doped samples have the lowest V_{on} at around 0.51 V, while the reference PN devices have V_{on} around 0.57 V.

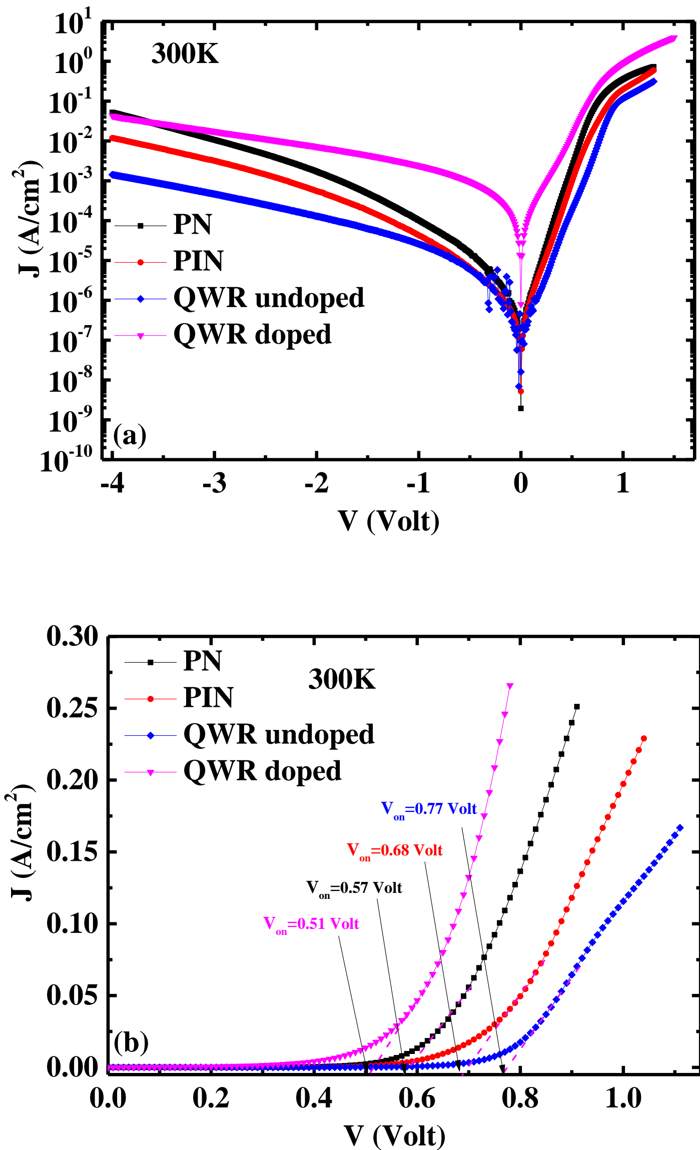

Fig. 6.4. (a) Semi-log plots of dark J-V characteristics at T=300 K for PN, PIN, QWR undoped and QWR doped devices; (b) The corresponding linear plots.

In order to get more insight in the functioning of the p-i-n devices, the dark J-V measurements as a function of temperature (20K-340K at 20 K intervals) were carried out for all devices, however, for clarity purposes, only selected presentative curves (20–320 K at 40 K intervals) are shown in Fig. 6.5. The steady increase in the forward dark current with temperature for PIN devices (Fig. 6.5 (b)) is normally

attributed to the exponential change of the concentration of the intrinsic carrier, n_i, in the depletion region with temperature [19]. The forward-biased dark current density transport characteristics of the QWR undoped devices have more pronounced temperature dependence as compared to the reference devices, i.e. PN and PIN. While the forward dark current density for the QWR doped devices have less noticeable temperature dependence as compared to the PIN and QWR undoped devices. Additionally, at low temperatures the QWR undoped devices exhibit an oscillation in the forward dark currents (see Fig. 6.6 for a temperature of 20K). The same behaviour was also observed at low temperatures (T<70 K) by Hao Feng Lu *et al.* [18] in QDs based solar cell devices. They suggested that these complicated dark current behaviours need to be interpreted by developing a new physical model for QDs solar cells rather than using the conventional diode model. In contrast, the forward dark current of the QWR doped devices follows a trend similar to that of the reference PN device.

Normally, the forward bias dark current is produced in a standard p-i-n solar cell via two mechanisms, namely, recombination current in the space charge region (SCR) and diffusion current through the SCR. Moreover, the change in the shape of the dark J-V curves as a function of temperature depends on the temperature dependence of the concentration and carrier capture cross-sections of different types of defects, as well as tunneling effects [20]. Besides, for the QWR devices there are additional recombination paths that are created via QWRs states and subsequently they will contribute to the dark current. The carrier capture and recombination processes under different voltage biases and temperatures are the main parameters that control the amount of additional dark current.

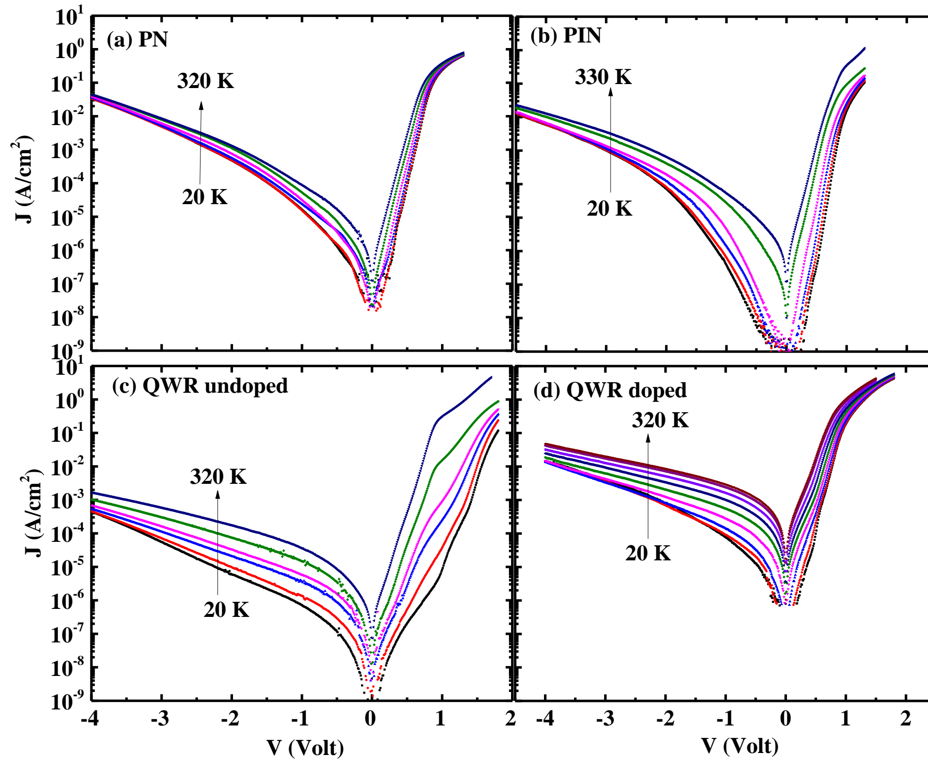

Fig. 6.5. Semi-logarithmic plots of dark I–V characteristics (a) PN; (b) PIN; (c) QWR undoped and (d) QWR doped devices in the temperature range of 20–340 K.

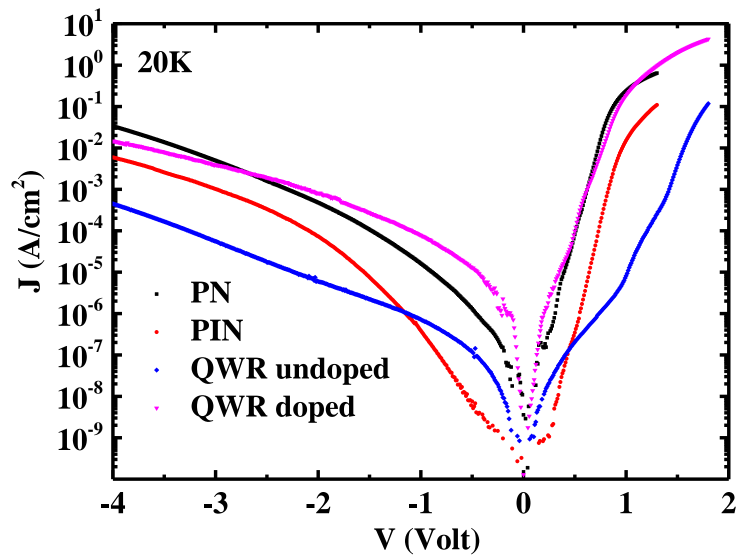

Fig. 6.6. Semi-log plots of dark J-V characteristics at T=20 K for PN, PIN, Undoped QWR and Doped QWR devices.

The J-V characteristics for all devices are analysed further to understand their properties by calculating the local ideality factor, n(V), using the following approximated equation [18, 21],

$$n(V) = \frac{d(V/V_t)}{d[ln(I)]} \qquad (6.1)$$

where V_t is the thermal voltage.

V_t is given by $V_t = k_B T/q$. The local ideality factors for all devices are calculated at room temperature and their values change with voltage as shown in Fig. 6.7. Three different regions generally appear around 0.2V, 0.4V and 0.5V indicating the currents transition between different dominating mechanisms [18, 21] in the devices. The n(V) behaviour over certain voltage ranges is similar for all devices. However, the QWR devices have unique trends at other voltage ranges. This suggests that some mechanisms are presumably enhanced or suppressed after adding QWRs, and some of the mechanisms are possibly unique to the QWR devices. It is worth pointing out that these results are in good agreement with the previous study carried out by Kunets *et al.* [7] for the same devices.

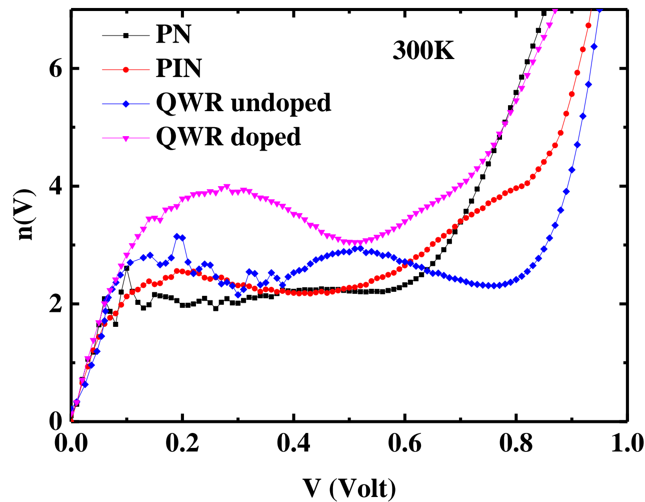

Fig. 6.7. Voltage dependence of the local ideality factor for PN, PIN, QWR undoped and QWR doped devices at 300 K.

To gain better understanding about the different conduction mechanisms occurring in the investigated devices, the local ideality factor versus voltage at different temperatures were determined for all devices as illustrated in Fig. 6.8. As can be seen, for each device there are two noticeable behaviours observed at low voltage and high voltage regions. In particular, at low voltages all devices exhibit a clear peak. However, for the QWRs devices, this peak becomes more significant (n>>1) as the temperature decreases and it shifts to higher voltages. Conversely, for PN and PIN devices this low voltage peak is almost temperature independent and has a very small amplitude as compared to the QWRs devices where n is much greater than unity. It is well-known that tunnelling or generation/ recombination processes can account for large ideality factors (n>1) [22]. These processes could also explain the large ideality factors observed in samples that incorporate QWRs in the intrinsic region and which create an additional current component that contributes to the total current of the devices. Thus the trend of the ideality factor at low voltages provides evidence of enhanced recombination via QWRs in these devices. A similar behaviour has been reported in QDs based solar cell devices [13]. Furthermore, for QWR doped samples, as a result of n-type Si δ–doping, the electrons will easily occupy the QWRs, and this leads to a strong local potential barrier around the QWRs. Thus, the electron mobility in the conduction band can be reduced as a result of variations of the local potential around the QWRs [10]. As a result, the J-V characteristics of these devices are worsened as evidenced by their larger ideality factors. It is worth pointing out that, a similar behaviour of the local ideality factor at low voltage biases was observed by Gu Tingyi *et al.* [21] in InAs/InGaAs quantum dots-in-a-well (DWELL) solar cells and by H. Kim *et al.* [23] in InAs quantum dots solar cells. As can be seen in Fig. 6.8, at higher voltages the local

ideality factor increases approximatively linearly with bias for all devices. These large values normally reflect that the series resistance effect becomes predominant [18, 21]. According to the obtained data, the local ideality factor of the PIN and QWR undoped devices is temperature dependent but the rate of change with the temperature is faster for the undoped QWR devices. However, for the PN and Doped QWR devices, the local ideality factor is practically temperature independent at high voltage.

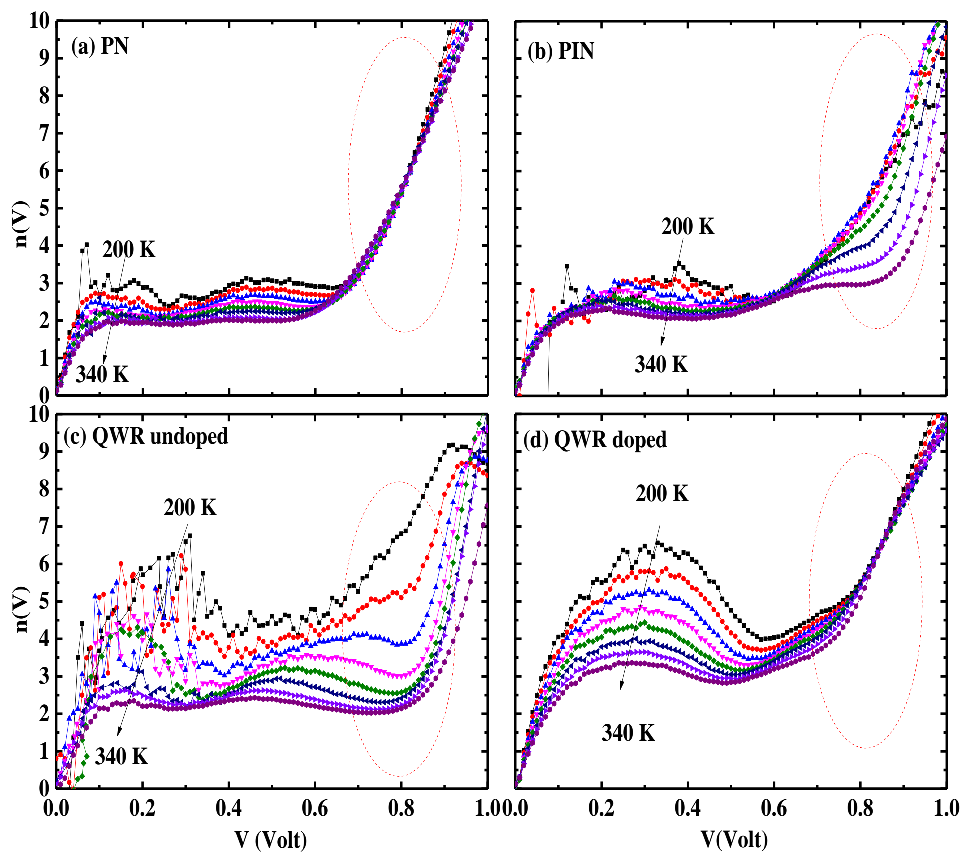

Fig. 6.8. Voltage dependence of the local ideality factor at different temperatures for (a) PN, (b) PIN, (c) QWR undoped and (d) QWR doped devices.

Fig. 6.9 displays the first derivative of the J-V characteristics of all devices at temperatures ≥ 200 K. For clarity purposes, the first derivative of the J-V

characteristics of all devices are replotted at 260 K as shown in the inset of Fig. 6.9 (d). A plateau region is only noticeable in PIN and QWR undoped devices at temperatures above 200 K and under higher forward bias regime. The appearance of the plateau is presumably due to the resonant tunnelling of electrons (or holes) through the quasi-bound levels in the QWR region [23, 24]. Clearly, Fig. 6.9 (c) shows the increase of the peak-to-valley ratio as the temperature increases. While when the temperature was reduced no plateau region was observed. In PIN and QWR undoped devices, the carriers are thermally activated to the allowed bands from which they can tunnel. Therefore, at low temperatures a few carriers are available in the band hindering the observation of resonant tunnelling, as shown in Fig. 6.9 (b) and Fig. 6.9 (c). Additionally, the thickness of the delta-doped layer is an important parameter of device design, having a direct influence on whether RIT occurs or not [25]. Indeed, as can be seen in Fig. 6.9 (d), when the delta-doped layer is incorporated in the QWR devices, the plateau disappears.

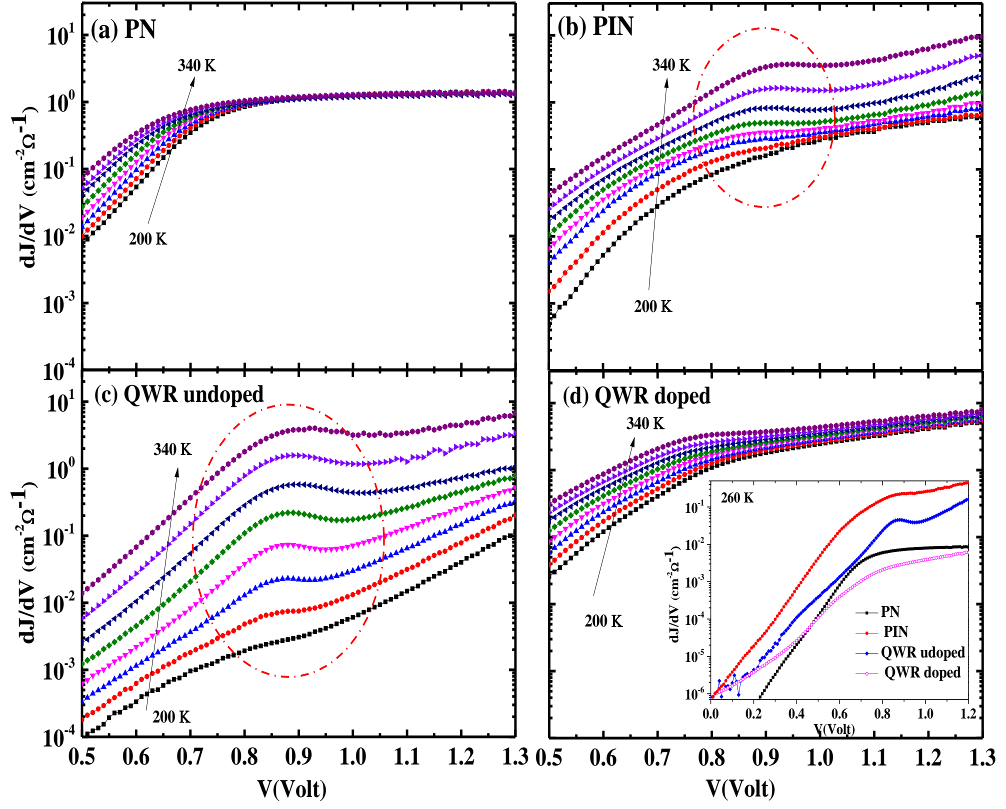

Fig. 6.9. Semi-log plots of dJ/dV versus V for (a) PN, (b) PIN, (c) QWR and (d) Doped QWR devices at temperatures ≥ 200 K. The inset in (d) shows Semi-log plots of dJ/dV versus V of all devices at 260 K.

6.3.2 C-V CHARACTERISTICS

In order to determine the apparent free carrier concentrations and to have more specific understanding of the junction structure of these devices, capacitance-voltage (C-V) measurements have been performed at a frequency of 1MHz. Fig. 6.10 depicts the dependence of the capacitance/area (C/A) as a function of bias voltage recorded at temperatures 300 K and 20 K for all devices. For a two plates capacitor the capacitance increases inversely with the separation between the plates $[C = \varepsilon_s \frac{A}{d}]$. In the p-n devices investigated in this work a maximum room temperature capacitance, C_{max}, is observed in forward biases as shown in Fig. 6.10

(a). C_{max} increases in the following sequence: C_{max1} (PN) < C_{max2} (PIN) < C_{max3} (QWR undoped) < C_{max4} (QWR doped). The same behaviours were also observed by Gunawan *at al.* [26] in p-n wire-array solar cells with different microsphere diameters fabricated by lithography technique. They observed an increase of C_{max} as the wire diameter increased. They suggested that this increase of C_{max} is due to the extra cylindrical sheath surface of the wires. It is worth pointing out that in the devices investigated by Gunawan *at al.* [26] the wires were vertical, while in this study the devices incorporated lateral wires (QWRs).

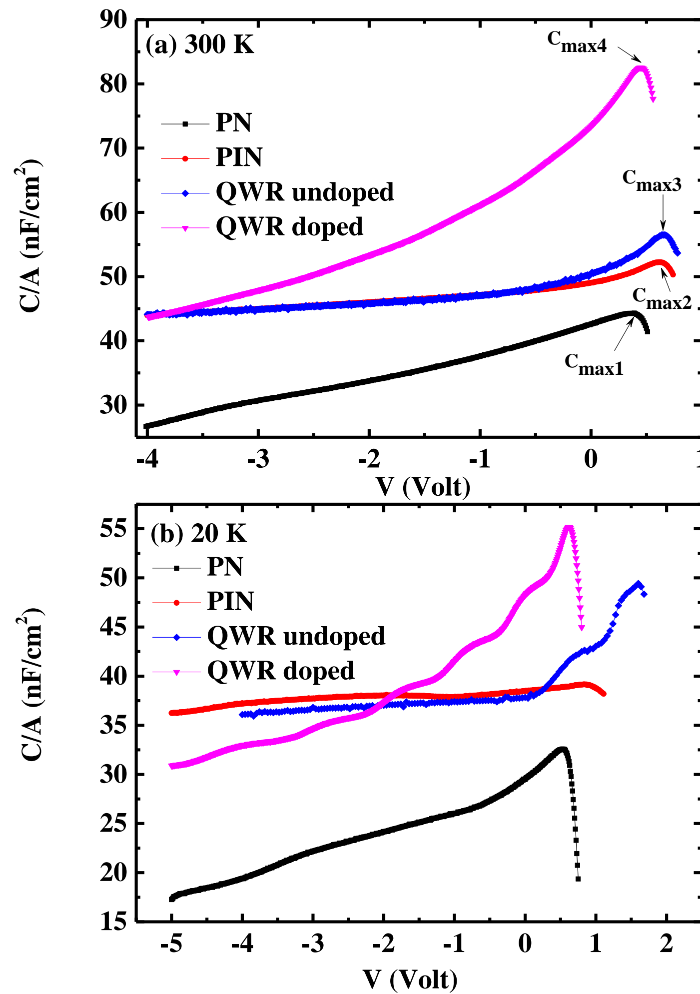

Fig. 6.10. Variation of capacitance/area with voltage for PN, PIN, Undoped QWR and Doped QWR devices at (a) 300 K and (b) 20K.

As the structure of the devices investigated are p-i-n junctions the capacitance is expressed by the following equation:

$$\frac{1}{C} = \frac{d}{\varepsilon_s \varepsilon_0 A} + \frac{x_n}{\varepsilon_s \varepsilon_0 A} + \frac{x_p}{\varepsilon_s \varepsilon_0 A} \qquad (6.2)$$

where d represents the thickness of the intrinsic region (cm), $x_{n,p}$ the depletion regions in both n and p sides (cm), respectively, and ε_s is the permittivity (F·cm^{-1}) of GaAs (12.9 ε_0 [22]) . As the doping levels of the n and p layers are fairly high, it is very likely that the intrinsic region dominates the overall capacitance because d is considered to be >> $x_{n,p}$. As a consequence, the capacitance should vary only slightly with bias in reverse conditions. As shown in Fig. 6.10 the capacitance change as function of reverse bias in PIN and QWR Undoped devices is very slow as expected by Equation (6.2). However, for the QWR Doped samples this behaviour deviates considerably from the one described by Equation (6.2) and it follows the same trend as the PN devices. The reason is very likely due to the effect of introducing n-type Si δ–doping which makes the QWR doped junction behaving as a PN junction.

Fig. 6.10 (b) shows that the capacitance/area (C/A) at T = 20 K decreases with increasing reverse bias, a behaviour which is frequently observed in this kind of device due to the increase of the depletion layer width. However, the most interesting features observed in the C-V characteristics are the plateaux or multiple steps detected in the QWR samples. For the QWR undoped devices the plateau appears only in the forward bias (0.24 – 1.0 V), while the steps are present in the QWR doped devices over the whole bias range. The distinct behaviours of the capacitance in QWR undoped devices can be related to a two dimensional electron gas (2DEG) formation as a result of electron localization in InGaAs 2D wetting layer (WL). Chiquito *et al.* [27] observed a plateau like dependence in their C-V

measurements at the bias range 0.5 to 1.5 V in InAs/GaAs self-assembled quantum dots system. They related this behaviour to the formation of 2DEG at the $(GaAs)_4/(AlAs)_{11}/GaAs$ top interface rather than at the WL because their PL and Raman scattering measurements proved that there is no contribution of the WL. In fact, the capacitance increase and the plateau features that are observed in the capacitance measurements for a bias range of 0.24 -1.0 V as shown in Fig. 6.10 (b) for QWR undoped samples could be attributed to the confinement of electrons at the InGaAs WL. Recent photoluminescence (PL) measurements performed by Kunets *et al.* [7] provided a strong evidence of the contribution of the 2D WL in QWR devices. Therefore, one could conclude that a 2DEG is created in the InGaAs WL when a forward bias is applied in the QWR undoped devices investigated here and would account for the plateaux observed in the C-V characteristics. When a sufficiently high forward voltage is applied the capacitance decreases as shown in Fig 6.9 (b) because the 2DEG layer is fully depleted of electrons. Babinski *et al.* [28] reported a similar behaviour at V= 0.7 V in $In_{0.6}Ga_{0.4}As/GaAs$ QDs grown by metalorganic vapour phase epitaxy. They explained the plateaux formation in the forward bias voltage by the QDs excited states filled by electrons or a DEG formed in InGaAs WL. It is, however, worthwhile mentioning that Kim et *al.* [29] observed a hump shape at a forward voltage near 0.4 V in InAs/GaAs QDs Schottky diodes grown by MBE. They related this hump to the carrier accumulation in the QDs layer.

In order to investigate further the behaviour of C-V characteristics, C-V measurements were performed at low frequencies for both doped (100 kHz) and undoped (10 kHz) QWR devices. The apparent carrier concentration profile as function of depth is also calculated by using the following relations [30]:

$$N_{CV}(W) = \frac{2}{A^2 q \varepsilon_s \varepsilon_0}\left[\frac{d}{dV}\left(\frac{1}{C^2}\right)\right]^{-1} \text{ and } W = A\frac{\varepsilon_s \varepsilon_0}{C} \qquad (6.3)$$

where W is the length of the depletion region and $N_{CV}(W)$ is the apparent carrier concentration for semiconductors with quantum confinement [31]. Fig. 6.11 shows the C-V and N_{CV} of doped and undoped QWR devices at 100 K at low and high frequency. It can be seen from the C-V plots that there is no significant capacitance difference between the C-V measurements at low and high frequency. Similarly, the N_{CV} plot at both frequencies in undoped and doped samples is unchanged. The C-V and N_{CV} have no frequency dependence, which confirms that the emission of electrons from quantum wires is very fast.

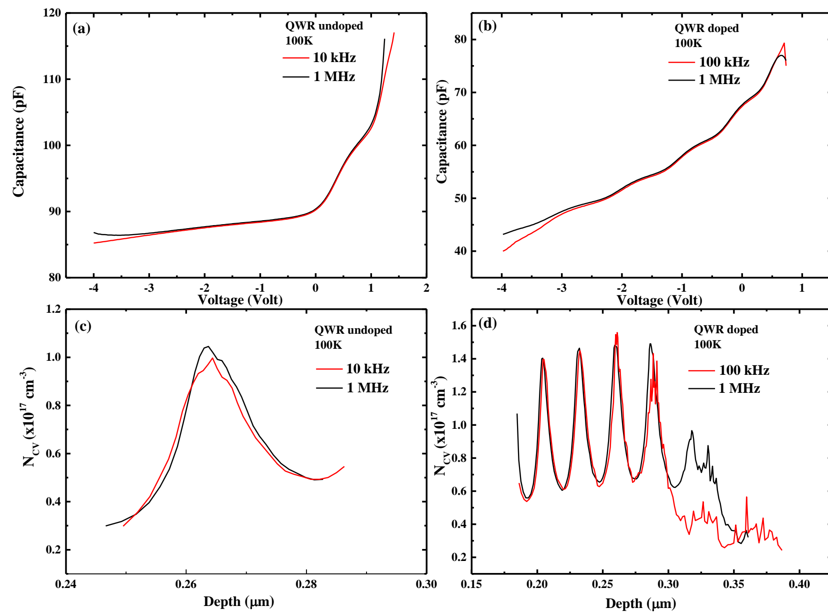

Fig. 6.11. Low/high frequencies C-V characteristics of (a) undoped and (b) doped QWR samples at 100 K. Concentration versus depth profiling of (c) undoped and (d) doped QWR samples at 100 K.

In order to determine the distance between the steps observed in Fig. 6.10 (b) for the QWR devices the derivative of capacitance (dC/dV) were calculated as shown

in Fig. 6.12. One could approximate the number of charge carriers accumulated in the QWR doped layers by using $Q=C_p \Delta V$, where C_p represents the capacitance at the plateau and ΔV represent the width of the plateau region [32]. The accumulation charge in the first, second, third, fourth and fifth QWRs layers of the QWR doped samples are calculated to be $Q_1= 4.02 \times 10^{-11}$ C, $Q_2= 4.72 \times 10^{-11}$ C, $Q_3= 4.73 \times 10^{-11}$ C, $Q_4= 4.94 \times 10^{-11}$ C and $Q_5= 5.43 \times 10^{-11}$ C, respectively. These values are associated with the fact that as the step is wider, the carrier concentration confined in the QWRs layer is higher [33, 34]. For the undoped QWR devices there is only one accumulation layer with a charge $Q= 8.56 \times 10^{-11}$ C. As shown in Fig. 6.12, for the QWR doped samples the width of the steps (ΔV) increases as the reverse bias increases. This increase could be attributed to the increase of the electrical field in the space charge region [35, 36]. As a result of this, for small reverse biases the first QWR layer is depleted of electrons while all the other QWRs layers in the device remain electrically neutral. When the reverse voltage is increased further, the conduction electrons are depleted to the second QWR layer, and therefore the boundary of the space charge region moves to the second QWR. This process will carry on until all the QWR are depleted. Thus, the number of steps in the capacitance curve is related to the number of depleted QWR layers in the device.

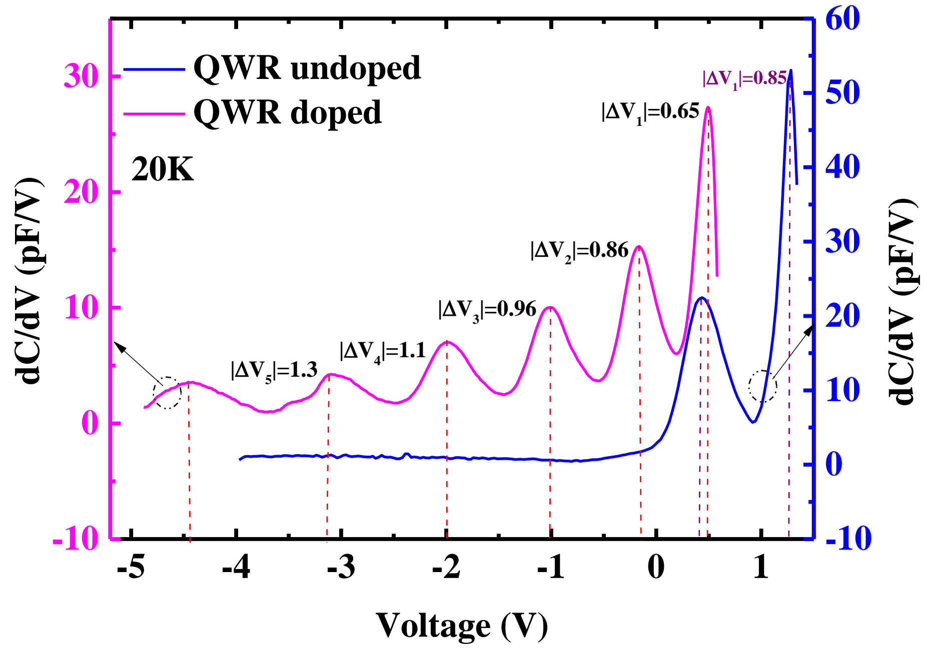

Fig. 6.12. dC/dV characteristics of the undoped and doped QWR devices measured at a frequency of 1MHz and temperature of 20K.

The free carrier concentration profile shown in Fig. 6.11 reflects clearly the charge carriers accumulated in the QWR layers. The estimated free carrier sheet densities [28, 36] for the first, second, third, fourth and fifth QWRs layers in Doped QWR devices are 7.96 x 10^{11} cm^{-2}, 1.00 x 10^{11} cm^{-2}, 1.00 x 10^{11} cm^{-2}, 8.66x 10^{10} cm^{-2}, 1.13 x 10^{11} cm^{-2}, respectively. While the free carrier sheet density for the QWRs layer in QWR undoped devices is 9.29 x 10^{10} cm^{-2}. Additionally, the distances between the N_{CV} peaks shown in Fig. 6.11 for QWRs layers was approximately 28 nm, which is nearly consistent with the designed QWR doped device structure (30nm).

6.3.3 DLTS AND LAPLACE DLTS CHARACTERISTICS

In order to explore the effect of the electrically active defects on the solar cell efficiency in GaAs (311)A solar cell devices, DLTS experiments [37] were carried out at biasing conditions of a reverse bias V_R = -0.25 V with filling pulse height V_P= 0 V, and a filling pulse duration, t_p =1 msec. The samples temperature was scanned from 10 K up to 450 K. Fig. 6.13 shows normalized DLTS spectra for all devices. DLTS measurements reveal a distinct broad minority electron trap peak (negative peak) over a wide range of temperatures in all devices which can be resolved by Laplace DLTS measurements [38]. In PN devices, in addition to the broad electron peak, a hole trap is also detected (positive peak).

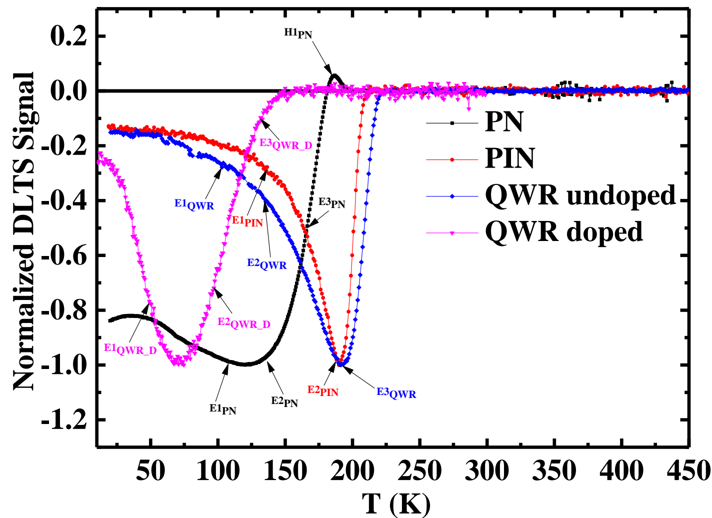

Fig. 6.13. Normalized DLTS spectra of PN, PIN, QWR undoped and QWR doped devices obtained with the following conditions: reverse bias V_R= -0.25 V, filling pulse V_p = 0 V and pulse duration t_p= 1 msec at rate window of 500 s^{-1}.

Laplace DLTS was used in order to resolve the broad electron trap peak detected in all samples. Fig. 6.14 shows that the broad DLTS peak observed for QWR doped

devices over the temperature range ~14-144 K (see Fig. 6.13) splits in three clear peaks as detected by the high resolution Laplace DLTS at T=53 K . In summary, the Laplace DLTS revealed the presence of the following traps: (i) PN: three electron traps ($E1_{PN}$ to $E3_{PN}$) and one hole trap ($H1_{PN}$); (ii) PIN: two electron traps ($E1_{PIN}$ & $E2_{PIN}$); (iii) QWR undoped: three electron traps ($E1_{QWR}$ to $E3_{QWR}$); (iv) QWR doped: three electron traps ($E1_{QWR_D}$ to $E3_{QWR_D}$).

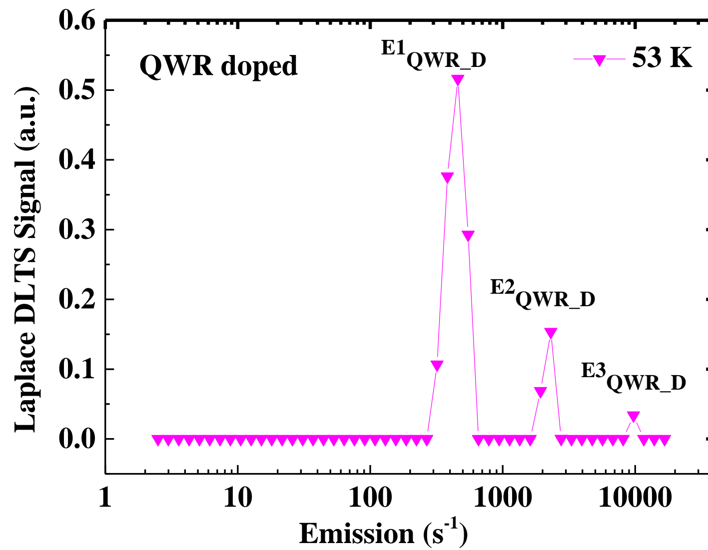

Fig. 6.14. Laplace DLTS of QWR doped devices at 53 K under biasing condition V_R=-0.25V, V_p= 0 V and t_p= 1 msec.

The Arrhenius plots of the emission rates as a function of temperature (ln (e_n /T^2) versus (1000/T)) for each defect level detected by Laplace DLTS are shown in Fig. 6.15. The traps activation energies and capture cross-sections are calculated from the slope and the intercept of the above plots, respectively. These are summarized in Table 6.1 with the concentrations of each trap. It is worth to mention that the traps concentrations are calculated from the peaks of Laplace DLTS signal and C-V measurements as explained in Chapter 4.

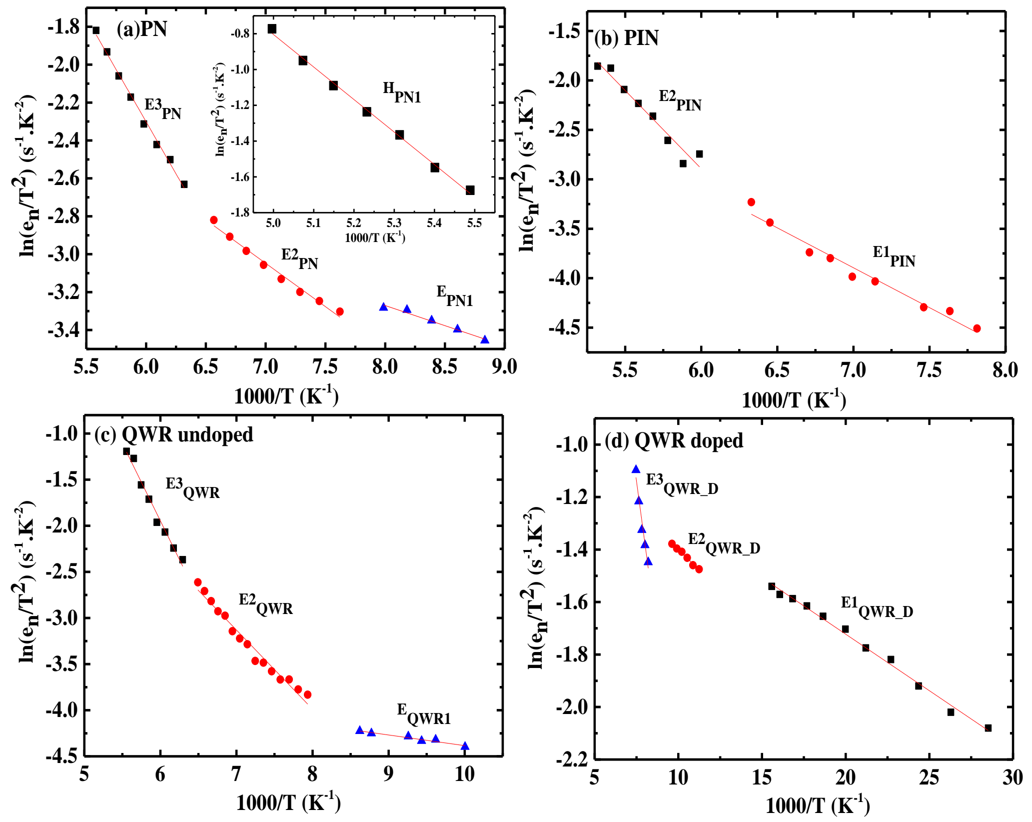

Fig. 6.15. Arrhenius plots of (a) PN, (b) PIN, (c) QWR undoped and (d) QWR doped devices at biasing condition V_R=-0.25 V, V_p= 0 V and t_p= 1 msec obtained from Laplace DLTS measurements.

Table 6.1. Summary of traps activation energies, capture cross-sections and concentrations for PN, PIN, QWR undoped and QWR doped devices.

Device	Trap Label	Activation energy (eV)	Apparent capture cross-section (cm^2)	Trap concentration (cm^{-3})
PN	$H1_{PN}$	(0.157±0.004)	1.96×10^{-18}	6.16×10^{15}
	$E1_{PN}$	(0.018±0.002)	1.01×10^{-21}	6.55×10^{14}
	$E2_{PN}$	(0.039±0.002)	5.68×10^{-21}	2.20×10^{13}
	$E3_{PN}$	(0.095±0.003)	3.54×10^{-19}	7.04×10^{15}
PIN	$E1_{PIN}$	(0.070±0.004)	2.81×10^{-20}	1.86×10^{14}
	$E2_{PIN}$	(0.14±0.01)	3.58×10^{-18}	2.93×10^{15}
QWR undoped	$E1_{QWR}$	(0.010±0.001)	1.93×10^{-22}	2.09×10^{15}
	$E2_{QWR}$	(0.074±0.003)	8.64×10^{-20}	4.03×10^{13}
	$E3_{QWR}$	(0.145±0.008)	1.63×10^{-17}	1.62×10^{15}
QWR doped	$E1_{QWR_D}$	(0.0037±0.0009)	2.06×10^{-21}	3.93×10^{15}
	$E2_{QWR_D}$	(0.0053±0.0001)	2.22×10^{-21}	5.99×10^{14}
	$E3_{QWR_D}$	(0.041±0.004)	5.38×10^{-20}	6.96×10^{13}

As seen in Table 6.1 only one hole trap, $H1_{PN}$, is detected in PN devices. It has an energy close to the one measured from Laplace DLTS by Boumaraf *et al.* [39] in p-type Si-doped GaAs Schottky diode. Although the origin of this defect is not yet clear, they suggested that it could be related to complexes involving silicon atoms, background impurities, and defects originating from the growth conditions used. $E1_{PN}$ has an activation energy comparable to the trap reported in GaAs [40]. However, the origin of $E1_{PN}$ is still not known.

It can be seen from Table 6.1 that the shallow trap, $E2_{PN}$ in PN reference device has approximately the same activation energy as trap, $E3_{QWR_D}$ detected in the QWR doped devices, and could possibly originate from the same defect. This trap might be assigned to an arsenic vacancy v_{As} introduced in electron-irradiated GaAs (labelled E_1) and whose activation energy was found to be 32–45 meV [41-44] below the conduction band. It is worth pointing out that this is the only trap which is common in the QWR doped and PN devices. In the earlier analysis of the C-V characteristics it was concluded that the QWR doped junction acts as PN junction as a result of introducing n-type Si δ–doping. This common shallow trap might justify this assumption in C-V. However, the capture cross-section and concentration of this trap in QWR doped devices are higher than those of the PN devices. According to the previous study [7] for this QWR doped device, the fitting of PL spectra at a high excitation intensity of 3000 W/cm^2 shows an energy difference between the wires and the 2D wetting layer transition to be 46 meV. This energy difference is nearly equal to the trap $E3_{QWR_D}$ activation energy. Thus another possibility that $E3_{QWR_D}$ could be related to the inter-band energy transition between the InGaAs wire and the 2D WL where tunnelling to the conduction band

could occur. $E3_{PN}$ trap with an activation energy of ~ 0.095 eV can be related to the well-known electron trap in GaAs grown by MBE, M0 (E_c-0.10 eV), that originated from chemical impurities during growth [45].

It can be seen from Table 6.1 that the electron traps $E1_{PIN}$ and $E2_{PIN}$ in the PIN devices have similar activation energies as the electron traps $E2_{QWR}$ and $E3_{QWR}$ in the QWR undoped devices, respectively. These traps in both PIN and QWR undoped devices may originate from the intrinsic GaAs region since these were not observed in PN devices. One can therefore infer that by introducing n-type Si δ–doping in QWR doped samples, $E2_{QWR}$ and $E3_{QWR}$ traps were annihilated. Additionally, it is found that the trap densities and apparent capture cross-sections of $E1_{PIN}$ and $E2_{PIN}$ are affected by the introduction of the InGaAs QWRs intermediate band. From DLTS measurements Lee *et al.* [46] detected an electron trap with activation energy of 0.14 eV in InAs/GaAs δ–doped QD solar cell structures grown by MBE and they identified this trap to M1 defect which is commonly observed in GaAs layers grown by MBE [45]. Furthermore, $E2_{PIN}$ and $E3_{QWR}$ have comparable activation energies as trap F (0.14 eV) reported by Asano *et al.* [47] in GaAs (001) /InAs/InGaAs/GaAs self-assembled QD structures. In their study, they inferred that the increase of the density of this trap and others traps around the QDs is due to the growth conditions of InGaAs/GaAs QD structures. In particular, the density of these defects were reduced by a factor of 20 when they used migration enhanced epitaxy (MEE) to grow the GaAs capping layer at 400 or 500 °C as compared to using MBE for a growth temperature of 500 °C. Also Fang *et al.* [34] detected the M1 defect in $In_{0.5}Ga_{0.5}As$/GaAs QDs structures grown by MBE and they attributed this defect to point defects instead of defect-impurity

complexes. Moreover, Kunets *et al.* [48] observed the M1 trap in $In_{0.35}Ga_{0.65}As/GaAs$ QDs structures grown by MBE using noise spectroscopy measurements, and they related the increase of its density to strain in the vicinity of $In_{0.35}Ga_{0.65}As$ QDs. Thus there is a consensus that $E2_{PIN}$ and $E3_{QWR}$ are related to M1 defect which could be assigned to defect-impurity complexes or/and point defects [34, 45, 48, 49]. The shallow trap $E1_{QWR}$ with energy of ~10 meV is only observed in QWR undoped devices. Thus, in this work it is believed that the $E1_{QWR}$ level is created due to the incorporation of InGaAs QWRs. From a rectangular potential well calculation using the Nextnano software, Vakulenko *et al.* [50] found that the quantum energy of the ground state in InGaAs/GaAs QD structures is approximately about 10 meV. This finding provides further evidence that $E1_{QWR}$ trap could be related to the incorporation of the QWRs.

For QWR doped devices the traps $E1_{QWR_D}$ to $E3_{QWR_D}$ are directly or indirectly related to the introduction of the n-type Si δ–doping since these traps were not observed in PIN and QWR undoped devices. The shallow trap $E2_{QWR_D}$ has an activation energy of ~5.3 meV which is comparable to the ionization energy of silicon donors in GaAs (5.8 meV) [51]. Furthermore, Teh *et al.* [52] found a similar trap level with concentration of ~ 10^{15} cm^{-3} using the temperature dependence of the double exponential decay measurements. They assigned this trap to silicon substituting for a gallium centre, Si_{Ga}, with binding energy of 5.85 meV.

It is relevant to note that some of the traps detected in the devices investigated in this work are reported here for the first time. Their origins are not clear and further investigations are needed.

These DLTS measurements for PIN, QWR undoped and QWR doped devices are correlated with the earlier solar conversion efficiency measurements done by Kunets *et al.* [14] at different temperatures (83 K-300 K). In their measurements they found that the efficiency increases as the temperature decreases in all devices until the temperature reached down to between 180 and 160 K, then the trend changed. In particular, in the PIN devices, the efficiency showed very small increments as the temperature decreased. While for the QWR undoped samples the efficiency increased considerably as the temperature decreased down ~120 K, then the efficiency decreased for lower temperatures. For the QWR doped devices, the efficiency tended to decrease as the temperature decreased. The dramatic changes in the efficiency in the temperature range below 160-180 K can be correlated to the peaks observed in the DLTS spectra over the same temperature ranges (see Fig. 6.13). Moreover, the above analysis of the DLTS and Laplace DLTS spectra demonstrates as well a reasonable correlation with the external quantum efficiency (EQE) study done by Kunets *et al.* [14] on these devices at different temperatures. In their work, they correlated the lower solar conversion efficiency values in the QWR undoped devices compared to the PIN and QWR doped samples in the temperature range 160-240 K to their lower integrated EQE over the same temperature. This behaviour has been explained by measuring the GaAs EQE. The integrated GaAs EQE measurements showed an obvious U-shape trend as a function of temperature for QWR undoped devices, however, for the reference PIN devices the GaAs EQE characteristics were almost temperature independent. In this study [14], this behaviour can be associated to the electrically active traps $E2_{QWR}$ and $E3_{QWR}$ since they were detected within the temperature ranges where the solar conversion efficiencies were low. Although the PIN and QWR undoped devices

have similar defects in terms of activation energy, the capture cross-sections of the QWR undoped devices are higher. Therefore, these higher cross-sections of these defects could have more influence on the solar conversion efficiencies. However, a rapid increase of solar conversion efficiency and associated increase of the integrated EQE signal at low temperatures (T<~120K) observed in InGaAs QWR undoped devices [14] could be attributed to the incorporation of QWRs which introduce an intermediate energy band for enhanced energy harvesting and therefore enhanced efficiency. This level/band, $E1_{QWR}$, was indeed detected by DLTS in the InGaAs QWR undoped samples. In the QWR doped devices, however, it was reported that the solar conversion efficiencies and integrated InGaAs EQE decrease at low temperatures (T<~120K). This behaviour could be attributed to the three traps $E1_{QWR_D}$ to $E3_{QWR_D}$ detected by DLTS. $E2_{QWR_D}$ has an energy comparable to the ionisation energy of Si as discussed above. $E1_{QWR_D}$ and $E3_{QWR_D}$, which were not observed in the PIN or QWR undoped samples, could be also assigned to complexes involving Si atoms via delta-doping.

6.4 CONCLUSION

I-V, C-V, DLTS and Laplace-DLTS techniques were used to investigate the existence of defects in GaAs p-i-n solar cells incorporating undoped and doped intermediate band QWRs in the intrinsic region of the device junction.

Analysis of the J-V dependence showed that the QWRs-containing devices exhibited a clear peak of the local ideality factor at small forward biases at all temperature conditions, which might be caused by the charges captured at the QWRs-induced defect states. While under large forward biases, the temperature dependence of the ideality factor for all devices was well related to the effect of the

series resistance. In addition, the C-V measurements at T=20 K revealed plateaux in QWR undoped devices which were related to 2DEG or/and the carrier accumulation in the QWRs layer, and for the QWR doped devices the ith steps observed in the C-V plots were related to the depletion of the ith QWR layers in the devices. The efficiency and EQE characteristics obtained by Kunets *et al.* [14] at different temperatures correlated with the appearance of trap peaks observed in the DLTS and Laplace DLTS spectra at almost the same temperature ranges. An IB level/band with energy of ~10 meV detected by Laplace DLTS in QWR undoped devices was related to the ground state energy of InGaAs QWRs. From these results, it is concluded that the observed defects play an important role in the efficiency of QWRs IBSC. They also provide an essential understanding of the properties of these solar cell structures in order to enhance further their efficiencies.

REFERENCES

[1] G. Conibeer, Materials Today **10** (11), 42 (2007).

[2] W. Shockley and H. J. Queisser, Journal of Applied Physics **32** (3), 510 (1961).

[3] A. Nozik, Physica E: Low-dimensional Systems and Nanostructures **14** (1), 115 (2002).

[4] A. Luque and A. Martí, Physical Review Letters **78** (26), 5014 (1997).

[5] A. Marti, N. Lopez, E. Antolin, E. Canovas, A. Luque, C. Stanley, C. Farmer and P. Diaz, Applied Physics Letters **90** (23), 233510 (2007).

[6] A. Luque, A. Martí and C. Stanley, Nature Photonics **6** (3), 146 (2012).

[7] V. Kunets, C. Furrow, T. A. Morgan, Y. Hirono, M. Ware, V. Dorogan, Y. I. Mazur, V. Kunets and G. Salamo, Applied Physics Letters **101** (4), 041106 (2012).

[8] P. Linares, A. Marti, E. Antolin and A. Luque, Journal of Applied Physics **109** (1), 014313 (2011).

[9] A. Luque and A. Martí, Advanced Materials **22** (2), 160 (2010).

[10] X. Shang, J. He, H. Wang, M. Li, Y. Zhu, Z. Niu and Y. Fu, Applied Physics A **103** (2), 335 (2011).

[11] A. Marti, N. Lopez, E. Antolin, E. Canovas, A. Luque, C. Stanley, C. Farmer and P. Diaz, Applied Physics Letters **90** (23), 233510 (2007).

[12] K. A. Sablon, J. W. Little, V. Mitin, A. Sergeev, N. Vagidov and K. Reinhardt, Nano letters **11** (6), 2311 (2011).

[13] K. A. Sablon, J. W. Little, A. Sergeev, N. Vagidov and V. Mitin, Journal of Vacuum Science & Technology A **30** (4), 04D104 (2012).

[14] V. P. Kunets, C. Furrow, M. Ware, L. de Souza, M. Benamara, M. Mortazavi and G. Salamo, Journal of Applied Physics **116** (8), 083102 (2014).

[15] V. P. Kunets, M. Teodoro, V. Dorogan, P. Lytvyn, G. Tarasov, R. Sleezer, M. Ware, Y. I. Mazur, J. Krasinski and G. Salamo, Applied Physics Letters **97** (26), 262103 (2010).

[16] V. P. Kunets, S. Prosandeev, Y. I. Mazur, M. Ware, M. Teodoro, V. Dorogan, P. Lytvyn and G. Salamo, Journal of Applied Physics **110** (8), 083714 (2011).

[17] P. Vaccaro, M. Hosoda, K. Fujita and T. Watanabe, Jpn. J. Appl. Phys. Part **1** (35), 1292 (1996).

[18] H. F. Lu, L. Fu, G. Jolley, H. H. Tan, S. R. Tatavarti and C. Jagadish, Applied Physics Letters **98** (18), 183509 (2011).

[19] E. Radziemska, International Journal of Energy Research **30** (2), 127 (2006).

[20] R. Kachare, B. Anspaugh and G. Garlick, Solid-state electronics **31** (2), 159 (1988).

[21] T. Gu, M. A. El-Emawy, K. Yang, A. Stintz and L. F. Lester, Applied Physics Letters **95** (26), 261106 (2009).

[22] S. M. Sze and K. K. Ng, *Physics of semiconductor devices*. (John Wiley & Sons, 2006).

[23] H. Kim, M. H. Park, S. J. Park, H.-S. Kim, J. D. Song, S.-H. Kim, H. Kim, W. J. Choi and D.-W. Kim, Current Applied Physics **14** (2), 192 (2014).

[24] A. Sellai, M. Henini and Z. Ouennoughi, physica status solidi (a) **208** (1), 210 (2011).

[25] M. Houng, Y. Wang, H. Chen, H. Wei and Y. Lee, Journal of Applied Physics **71** (2), 780 (1992).

[26] O. Gunawan, K. Wang, B. Fallahazad, Y. Zhang, E. Tutuc and S. Guha, Progress in Photovoltaics: Research and Applications **19** (3), 307 (2011).

[27] A. Chiquito, Y. A. Pusep, S. Mergulhão and J. Galzerani, Brazilian Journal of Physics **32** (3), 784 (2002).

[28] A. Babiński, A. Wysmołek, T. Tomaszewicz, J. Baranowski, R. Leon, C. Lobo and C. Jagadish, Applied Physics Letters **73** (19), 2811 (1998).

[29] J. S. Kim, E. K. Kim, J. O. Kim, S. J. Lee and S. K. Noh, Superlattices and Microstructures **46** (1), 312 (2009).

[30] M. Kaniewska and O. Engström, Materials Science and Engineering: C **27** (5), 1069 (2007).

[31] E. F. Schubert, *Doping in III-V semiconductors*. (Cambridge University Press, 2005).

[32] M. Geller, E. Stock, C. Kapteyn, R. Sellin and D. Bimberg, Physical Review B **73** (20), 205331 (2006).

[33] Y. M. Park, Y. J. Park, K. M. Kim, J. C. Shin, J. D. Song, J. I. Lee and K.-H. Yoo, Journal of Applied Physics **95** (1), 123 (2004).

[34] Z. Fang, Q. Xie, D. C. Look, J. Ehret and J. Van Nostrand, Journal of Electronic Materials **28** (8), L13 (1999).

[35] M. Ershov, V. Ryzhii and K. Saito, Journal of Physics D: Applied Physics **28** (10), 2118 (1995).

[36] C. Moon, B.-D. Choe, S. Kwon, H. Shin and H. Lim, Journal of Applied Physics **84** (5), 2673 (1998).

[37] D. Lang, Journal of Applied Physics **45** (7), 3023 (1974).

[38] L. Dobaczewski, A. Peaker and K. B. Nielsen, Journal of Applied Physics **96** (9), 4689 (2004).

[39] R. Boumaraf, N. Sengouga, R. Mari, A. Meftah, M. Aziz, D. Jameel, N. Al Saqri, D. Taylor and M. Henini, Superlattices and Microstructures **65**, 319 (2014).

[40] M. Aziz, P. Ferrandis, A. Mesli, R. H. Mari, J. F. Felix, A. Sellai, D. Jameel, N. Al Saqri, A. Khatab and D. Taylor, Journal of Applied Physics **114** (13), 134507 (2013).

[41] D. Pons and J. Bourgoin, Journal of Physics C: Solid State Physics **18** (20), 3839 (1985).

[42] C. Corbel, M. Stucky, P. Hautojärvi, K. Saarinen and P. Moser, Physical Review B **38** (12), 8192 (1988).

[43] S. Loualiche, A. Nouailhat, G. Guillot and M. Lannoo, Physical Review B **30** (10), 5822 (1984).

[44] S. Lai and B. Nener, Journal of Applied Physics **75** (5), 2354 (1994).

[45] D. V. Lang, A. Y. Cho, A. Gossard, M. Ilegems and W. Wiegmann, Journal of Applied Physics **47** (6), 2558 (1976).

[46] K. S. Lee, D. U. Lee, E. K. Kim and W. J. Choi, Applied Physics Letters **107** (20), 203503 (2015).

[47] T. Asano, Z. Fang and A. Madhukar, Journal of Applied Physics **107** (7), 073111 (2010).

[48] V. P. Kunets, T. A. Morgan, Y. I. Mazur, V. Dorogan, P. Lytvyn, M. Ware, D. Guzun, J. Shultz and G. Salamo, Journal of Applied Physics **104** (10), 103709 (2008).

[49] S. Lin, C. Balocco, M. Missous, A. Peaker and A. Song, Physical Review B **72** (16), 165302 (2005).

[50] O. Vakulenko, S. Golovynskyi and S. Kondratenko, Journal of Applied Physics **110** (4), 043717 (2011).

[51] S. Krishnamurthy, M. Van Schilfgaarde and N. Newman, Applied Physics Letters **83** (9), 1761 (2003).

[52] C. Teh, J. Tuszyński and F. Weichman, Journal of Materials Research **5** (02), 365 (1990).

CHAPTER 7: INVESTIGATION OF THE EFFECTS OF GAMMA RADIATION ON THE ELECTRICAL PROPERTIES OF DILUTE $GaAs_{1-x}N_x$ LAYERS GROWN BY MOLECULAR BEAM EPITAXY

This Chapter reports the effect of gamma (γ-) irradiation on the electrical properties of dilute GaAsN epilayers having nitrogen concentrations ranging from 0.2 to 1.2% using Current - Voltage (I-V), Capacitance - Voltage (C-V), Deep Level Transient Spectroscopy (DLTS) and Laplace DLTS measurements in the temperature range from 10 K to 450 K. It is worth pointing out that these measurements are carried out a long time after the irradiation was preformed to ensure that post irradiation stability has been reached. The DLTS measurements revealed that after irradiation the number of traps is either decreased, remained constant, or new traps are created depending on the concentration of nitrogen. The origin of the defects present before and after irradiation are discussed and correlated.

7.1 INTRODUCTION

Dilute III-V nitride semiconductors present substantial reduction in their band gap when only a small number of nitrogen atoms is incorporated in their lattice. This band gap engineering, which allow the electronic and optical properties to be tailored [1], makes GaAsN a very attractive material for several applications such as multi-junction solar cells [2, 3], laser diodes [4, 5], and heterojunction bipolar transistors [6]. On the other hand, the presence of new nitrogen-related deep defects and shallow defects due the incorporation of nitrogen in GaAs has been observed

[7]. Nonetheless, a complete understanding of the origin of these defects has not yet been fully achieved [8].

Recently, DLTS and Laplace DLTS techniques have been used to provide information about electron traps in dilute GaAsN layers grown by Molecular Beam Epitaxy (MBE) on n+ GaAs substrates [9]. It was observed that few shallow and deep levels with activation energies ranging from 0.036 to 0.13 eV are introduced in samples containing nitrogen with concentration of 0.2% to 0.4%. More recently, B. Bouzazi *et al.* [8] employed DLTS to investigate the effect of electron irradiation and hydrogenation of GaAsN grown by chemical beam epitaxy on the main nitrogen-related nonradiative recombination center E1, with activation energy of 0.33 eV below the bottom edge of the conduction band. Additionally, they suggested that the origin of this defect is related to the compensation of the tensile strain in the film caused by the small atomic size of N atom compared to that of As. They found that the density of E1 increases with increasing the fluency doses of electron irradiation. T. Hashizume and H. Hasegawa [10] reported the effect of gamma irradiation on the electron traps present in as-grown liquid encapsulated Czochralski GaAs. In this study, they found that after irradiation the concentration of EL6 trap was reduced by a factor of 3-5, whereas the density of EL3 was increased about one order of magnitude.

From the applications viewpoint, it is of importance to study the effect of irradiation on semiconductor-based devices such as metal-insulator/oxide-semiconductor, Schottky barrier diodes, solar cells and heterostructures, because they are used in satellites. Thus due to the radiation in space, considerable amount of lattice defects are induced in semiconductors and these defects cause degradation of the devices performance [11]. Additionally, the study of defects created by irradiation can

provide practical data to fabricate radiation-resistant devices. However, there are relatively few reports on the effects of gamma irradiation on the electrically active defects in GaAsN-based devices. Therefore, the intentional introduction of deep defects by gamma irradiation in dilute GaAsN layers can be useful for a better understanding of the behavior of nitrogen atoms in GaAs and their role in the traps formation and/or in the traps passivation. In this work we present experimental confirmation on the effect of gamma irradiation on post-irradiation stability (i.e. a long time after the exposure to radiation was preformed) using I-V, C-V, DLTS and Laplace DLTS measurements of dilute GaAsN epitaxial layers containing different nitrogen concentrations over a long period of time after the exposure of the devices to the high radiation dose.

7.2 SAMPLE DETAILS

In this study, GaAsN samples were grown on n^+ GaAs substrates with nitrogen concentrations of 0.2%, 0.4%, 0.8% and 1.2% using MBE as reported in ref. [9]. The main growth parameters are: growth rate is 1 μm per hour and growth temperature is 500°C. As shown in Fig. 7.1 (a), the epitaxial layers consisted of 0.1 μm of a thick buffer layer of GaAs heavily doped with Si (n = 2x10^{18} cm^{-3}), followed by a 1 μm silicon doped GaAsN epilayer (n = 3x10^{16} cm^{-3}).

The samples were irradiated with a gamma cell Cobalt Irradiator (dose rate of 5.143 KGy/hour) at a high dose of 50 kGy. After gamma irradiation the devices are processed in the form of circular mesas with different diameters for the electrical characterization as shown in Fig. 7.1 (b). Thermal evaporation of Ge/Au/Ni/Au is used to fabricate an Ohmic contact to the back side of the n^+ GaAs substrates. This was followed by a thermal treatment at 370 °C for 60 sec in a rapid thermal

annealing system under a gas flow of 1% Hydrogen in Argon. Ti/Au circular Schottky contacts were then deposited by thermal evaporation on top of the doped epilayer.

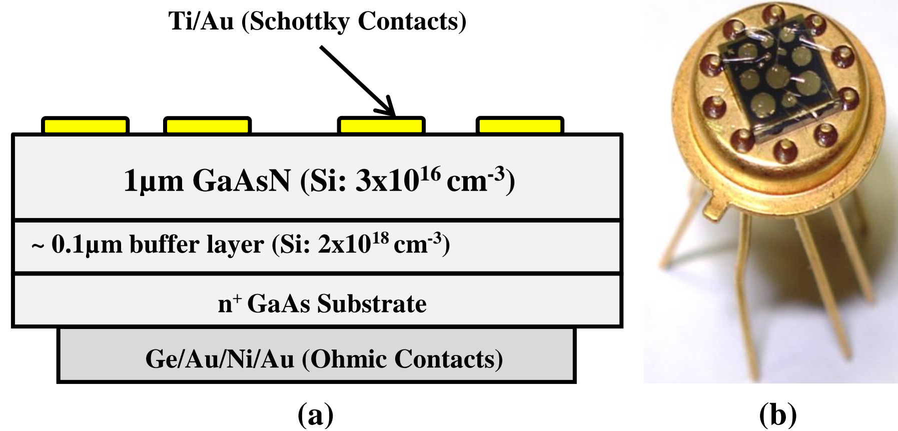

Fig. 7.1. (a) Devices structure of n-type MBE-grown GaAsN with different nitrogen compositions and (b) Photograph of samples mounted on TO5 header.

7.3 RESULTS AND DISCUSSION

In order to study the effect of gamma (γ-) irradiation on the electrical properties of dilute GaAsN with Nitrogen concentrations ranging from 0.2 to 1.2 %, I-V, C-V, DLTS and Laplace DLTS measurements were performed.

7.3.1 I-V CHARACTERISTICS

In order to investigate the effect of Gamma irradiation on the electrical properties of dilute GaAsN as a function of nitrogen concentration, I-V measurements at different temperatures were performed. Fig. 7.2 shows the current density–voltage (J–V) characteristics at room temperature of as-grown and irradiated GaAsN. All diodes exhibited a relatively low leakage current density.

It is worth pointing out that all as-grown samples exhibit lower values of the reverse current density compared to the irradiated samples, except for the sample with 0.8% nitrogen concentration (See Fig. 7.2 (c)). On the other hand, the irradiation effect was more pronounced in the sample with nitrogen content of 0.4%, as can be seen in Fig. 7.2 (b), where the leakage current increased by approximately four orders of magnitude. The I-V results indicate that there are two possibilities of such higher reverse current in the irradiated devices: (i) the radiation introduces extra defects which act as generation-recombination centers; (ii) radiation increases the concentration of major defects which contribute to the increase of the leakage current. The same observation of the increment of the leakage current due to irradiation dose has been already reported by Shailesh K. Khamari *et al.* [12] for GaAs p–i–n diodes subjected to different irradiation doses up to 50 kGy. They attributed these increments due to the increase of generation recombination centers. In the following section a detailed analysis will be presented to shed some light on the possibilities which are responsible for the increase of the leakage current when the samples are irradiated.

As these devices are Schottky diodes, then their I-V curves may be described by the thermionic emission model with a series resistance (R_s) [13]:

$$I = I_s \left[exp\left(\frac{q(V - IR_s)}{nkT} \right) - 1 \right] \qquad (7.1)$$

where q is the electronic charge, V is the applied voltage, k is the Boltzmann constant, n is the ideality factor, I_s is the saturation current, and T is the absolute temperature in Kelvin. The values of n and I_s are determined from the experimental data. The saturation current I_s is given by:

$$I_s = AA^{**}T^2 exp\left(\frac{-q\phi_B}{kT} \right) \qquad (7.2)$$

where A is the diode area and $A^{**} = 8.16$ Acm^{-2} K^{-2} is the effective Richardson's constant for n-GaAs, and ϕ_B is the barrier height [14].

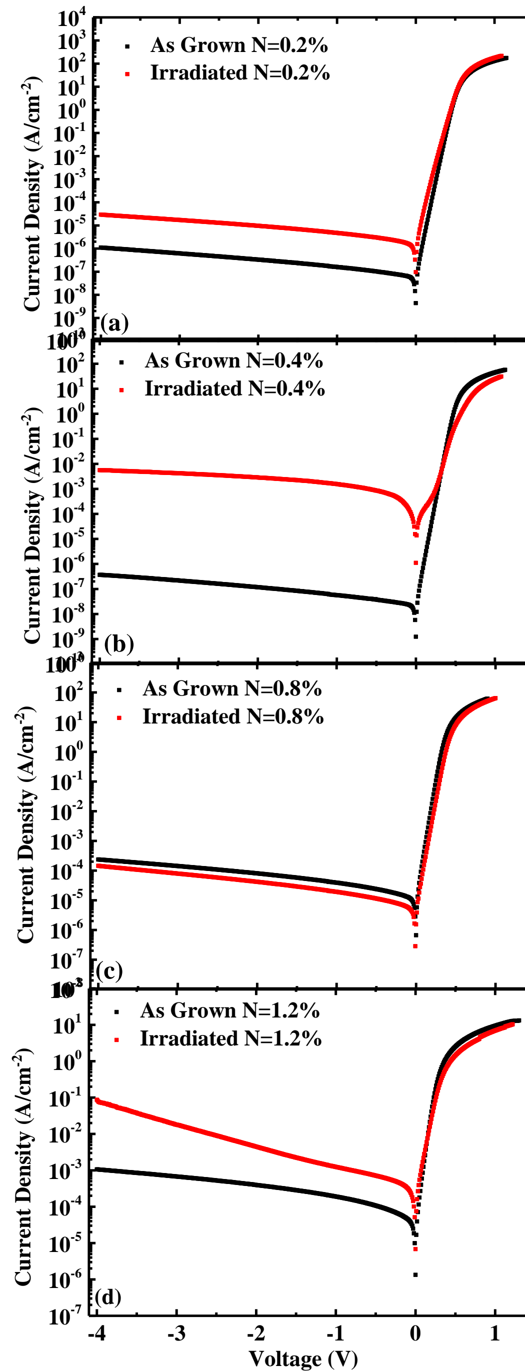

Fig. 7.2. Room temperature semi-logarithmic plots of dark J-V characteristics of as-grown and irradiated samples (a) N = 0.2%, (b) N = 0.4%, (c) N = 0.8% and (d) N = 1.2%.

In order to improve the accuracy of the characteristics parameters (R_S, I_S, ϕ_B and n) of the devices, the method developed by Werner was used [15]. This method as explained in Chapter 4 involves plotting the conductance divided by current (G/I) versus conductance (G) as shown in Fig. 7.3 for the as-grown sample with N= 0.2% at room temperature. The Werner's plot provides also important information about the interfacial oxide layers and/or pinning of the Fermi level. The linearity of the plots in our devices is an indication that they are not being affected by these two quantities, as can be seen in Fig. 7.3.

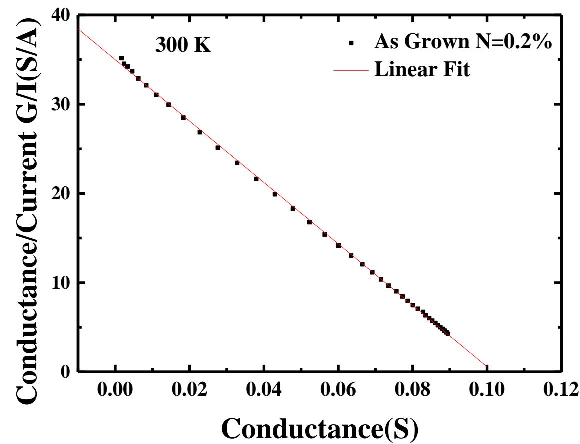

Fig. 7.3. G/I-G plot obtained from the I-V curve at room temperature for forward voltages for the as-grown sample with N= 0.2% (this plot was used to obtain the ideality factor n and series resistance R_s).

Series resistance, barrier height, and ideality factors for all samples are extracted from the room temperature forward *I-V* characteristics, and these are summarized in Table 7.1. Figures 7.4 and 7.5 display the temperature dependence of the ideality factor and barrier height, respectively, as determined from the I–V characteristics for as-grown and irradiated samples with 0.2%, 0.4%, 0.8% and 1.2% nitrogen concentration over a temperature range from 205 K to 340 K.

Table 7.1. Room temperature experimental barrier height, series resistance (R_s) and ideality factor determined from *I–V* characteristics of as-grown and 50kGy gamma irradiated *n*-type MBE-grown GaAsN containing different nitrogen.

Sample	0.2% N		0.4% N		0.8% N		1.2% N	
	As-grown	Irradiated	As-grown	Irradiated	As-grown	Irradiated	As-grown	Irradiated
n	1.12	1.4	1.05	2.1	1.1	1.2	1.1	1.45
ϕ_B (eV)	0.81	0.72	0.79	0.61	0.63	0.65	0.63	0.60
R_s (Ω)	10	6.7	7.7	16.3	8.7	27.38	35	200

All as-grown samples have room temperature ideality factors near unity as compared to the irradiated samples where *n* deviates from unity. Such a deviation of *n* from the unity usually indicates that the current mechanism is not only controlled by the thermionic emission effect but there are other effects that contribute to the conduction mechanism. Inhomogeneity of zero bias Schottky barrier height, series resistance, interface states, generation-recombination mechanism, image force Schottky barrier lowering, and the interfacial charges distributed non-uniformly are examples that cause the deviation from the thermionic emission theory [16-19]. In addition, as can be seen in Fig.7.4 and Fig. 7.5, for all irradiated and as-grown samples with N = 0.2 %, 0.8 % and 1.2 % the experimental values of ϕ_B increase with an increase of temperature, while the experimental values of *n* decrease. However, all irradiated diodes still have larger ideality factors at all temperatures compared to as-grown diodes. Also, the irradiated devices with N=0.2% have lower ideality factor compared to the

irradiated diodes with N=1.2%. Besides, the irradiated diodes with N = 0.8% have lower ideality factor compared to the irradiated diode with N = 0.4%.

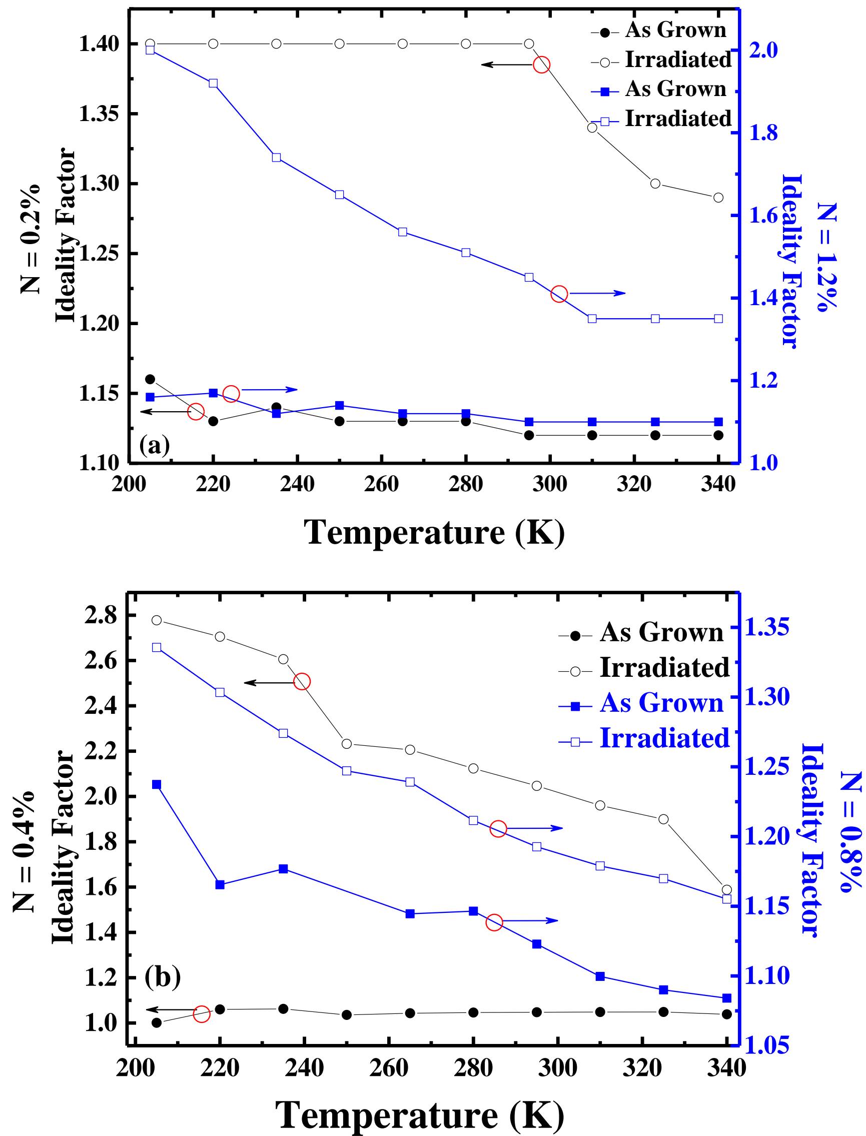

Fig. 7.4. Temperature dependence of the experimental: ideality factor determined from I–V characteristics of as-grown and 50kGy gamma irradiated *n*-type MBE-grown GaAsN with nitrogen concentrations of (a) 0.2% and 1.2%. and (b) 0.4% and 0.8%.

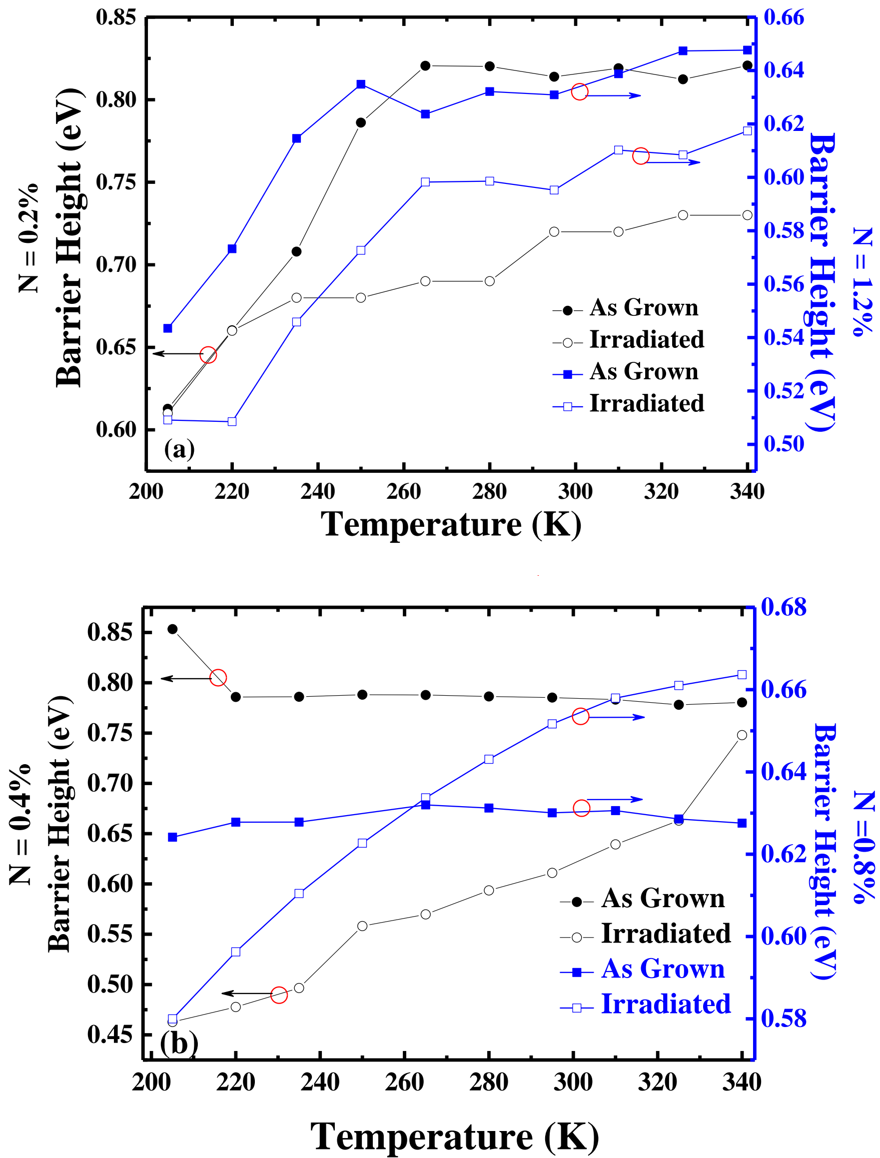

Fig. 7.5. Temperature dependence of the experimental barrier height determined from I–V characteristics of as-grown and 50kGy gamma irradiated *n*-type MBE-grown GaAsN with nitrogen concentrations of (a) 0.2% and 1.2%. and (b) 0.4% and 0.8%.

Further, from Table 7.1 it can be seen that at room temperature the barrier height decreases as the nitrogen concentration increases for both as-grown and irradiated samples. This reduction in barrier height was observed also by Narayanamurti *et al.* [20] in their study using the ballistic electron emission microscopy (BEEM)

technique. They attributed this drop to the reduction of the bandgap due to the incorporation of nitrogen. Similar behavior of the reduction of the barrier height due to the irradiation effect is also observed in all our samples. The decrease of the barrier height for the irradiated samples with nitrogen concentrations of 0.2, 0.4, and 1.2% are 11, 23, and 5%, respectively (see Table 7.1). However, the barrier height for the irradiated samples with nitrogen concentration of 0.8% increased to about 6%. The relative change in the barrier height before and after irradiation is smaller for samples with N= 0.8 and 1.2% compared to samples with lower N%. This gives an indication that the devices with 0.8 % and 1.2 % of nitrogen are more resistant to radiation than devices with lower N concentration. Recent studies have shown that after ionizing irradiation the barrier height decreases, and this behavior can be correlated with the modification of the density of free carriers at the device interface induced by the gamma irradiation [21, 22].

Fig. 7.5 (a) clearly depicts that the barrier height firstly increases with temperature up to ~270 K and then it varies slightly up to 340 K for both as grown and irradiated samples with N =0.2% and 1.2% concentrations. Besides Fig. 7.5 (b) shows that for the temperature range from 265 K up to 340 K, the as-grown samples with N = 0.8% have lower barrier height when compared to the irradiated diodes with N = 0.8%. It is worth to mention that the reason of the increase of the barrier height after irradiation will be explained in DLTS section (7.3.3). Also from Fig. 7.5 (a-b), it can be seen that the gamma irradiation reduces the barrier height for samples with nitrogen concentrations of 0.2%, 0.4%, and 1.2 % at all temperature ranges. This temperature variation of the barrier height and the ideality factor, the so-called the T_0 anomaly [23], is usually observed in semiconductors-metal diodes. In general, to investigate this effect, nT versus T plot is established. If the slope of

such a graph is unity but the line does not go through the origin, then this provides a proof that the temperature dependence of the ideality factor has a T_0 anomaly [23, 24].

Fig. 7.6 (b) shows the experimental nT versus T plot of as-grown GaAsN diodes with N=0.4%. From this plot a value of T_0 of 7.74 K was obtained with a single slope of 1.02, and this suggests that the conduction mechanism may be governed by thermionic emission [25]. But after gamma ray irradiation, the experimental nT versus T plot, shown in Fig. 7.6 (b), displays two slopes and consequently two set of values for T_0. In particular, (i) a slope of 1.4 (larger than unity) and T_0 = 277.6 K are obtained in the temperature range ≤200 K, which means that the ideality factor becomes temperature dependent while T_0 is temperature independent and constant [23, 26], and (ii) a slope of 0.5 (smaller than unity) and T_0 = 447.2 K are obtained in the temperature range >200 K, which means that T_0 is temperature dependent [26]. Also, Fig. 7.6 (a) and Fig. 7.6 (d) show that, as-grown GaAsN diodes have T_0 =63.50K with slope of 1.07 and T_0 = 35.24 K with slope of 0.99 for N = 0.2% and N = 1.2%, respectively. But for irradiated diodes with N = 0.2% the slope is larger than unity (1.4) and goes through the origin, which infers that the ideality factor becomes temperature independent [23, 26] when the samples are irradiated. Furthermore, Fig. 7.6 (c) shows that both as-grown and irradiated diodes with N=0.8% have the same slope of 0.88 with T_0 =69.16 K and T_0 =92.27 K, respectively. This effect is an indication of non-ideal thermionic emission [27]. For Au/n-GaAs Schottky diodes A. Tataroğlu *et al.* [28] observed an increase in ideality factor and a decrease in the barrier height when the temperature is reduced and they attributed this effect to inhomogeneities of the Schottky barrier with Gaussian distribution at the metal/semiconductor interface.

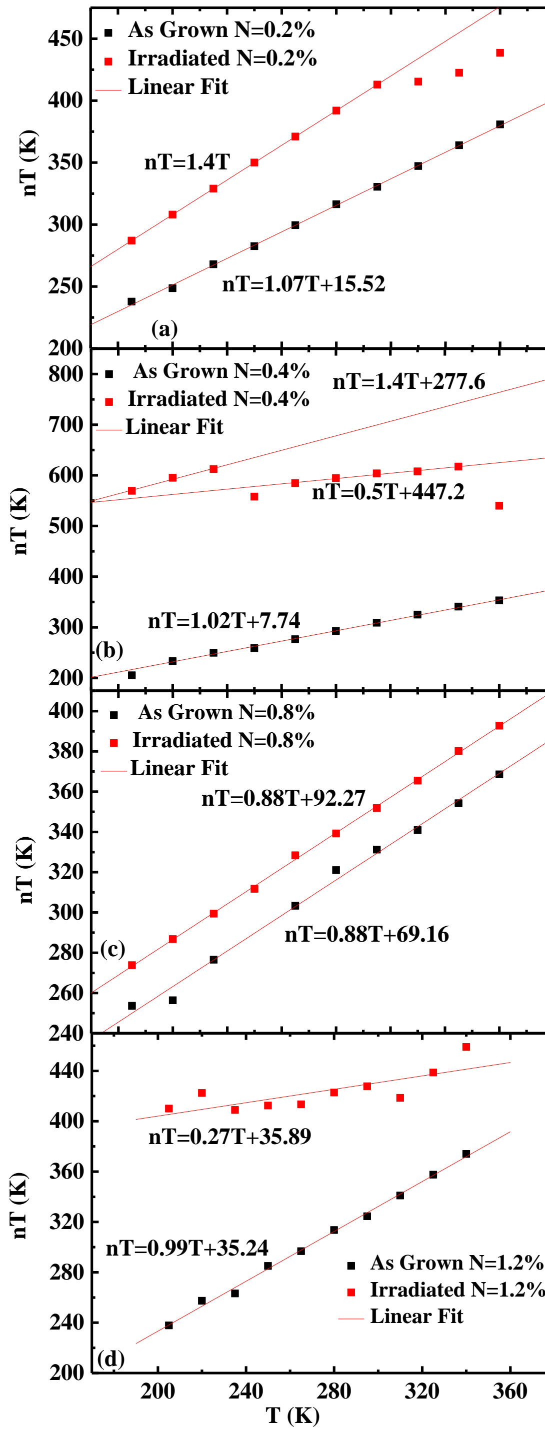

Fig. 7.6. Experimental *nT* versus *T* plot of as-grown and 50kGy gamma irradiated n-type MBE-grown GaAsN with nitrogen concentrations of (a) 0.2%, (b) 0.4%, (c) 0.8% and (d) 1.2% in the temperature range of 205–345 K.

Fig. 7.7 shows a linear relation between the experimental barrier height and the ideality factor at temperatures from 205 K to 295 K for irradiated samples with N=0.2% and from 205 K to 345 K for irradiated samples with N=0.4, 0.8 and 1.2%, respectively. This behavior is related to the lateral inhomogeneities of the barrier heights of the Schottky diodes [28]. This behavior is observed in all samples, although the curves are not perfectly linear. Normally, the incorporation of nitrogen into GaAs reduces the electron mobility and consequently increases barrier height inhomogeneities [29]. It is worth pointing out that the ideality factor for N= 0.8% is lower than the sample with N=0.2%. This could be due to the quality of device processing.

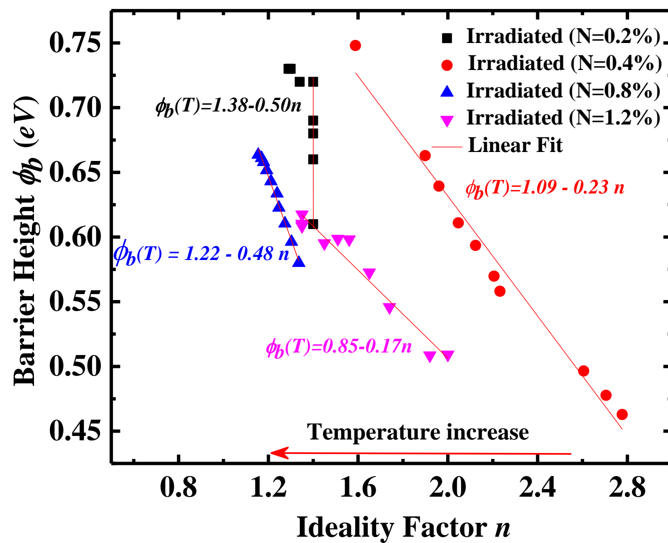

Fig. 7.7. Variation of the barrier height versus ideality factor of irradiated GaAsN (N = 0.2-1.2%) for temperatures ranging from 205 K to 345 K (The arrow indicates the direction of increasing temperature).

Fig. 7.8 illustrates the temperature dependence of the series resistance as determined from the I–V characteristics for as-grown and irradiated samples with 0.2%, 0.4%, 0.8% and 1.2% nitrogen concentrations over a temperature range from 205 K to 340 K. Normally, the series resistance affects the linearity of the *ln(I)-V* curve at adequately large applied voltages by significantly curving downwards the forward *I-V* plot. The diode series resistance is found to increase due to irradiation for samples with N=0.4, 0.8 and 1.2% as can be observed in Fig. 7.8. On the other hand, a decrease of the series resistance is observed for samples with N= 0.2%. This behaviour has only been reported for p-type GaAs [30]. Furthermore, R_s for both as-grown and irradiated samples with large nitrogen concentration (N ≥ 0.8%) decreases with the increase of temperature. This could be explained by the fact that both n and the free charge carriers decrease with increasing temperature [23].

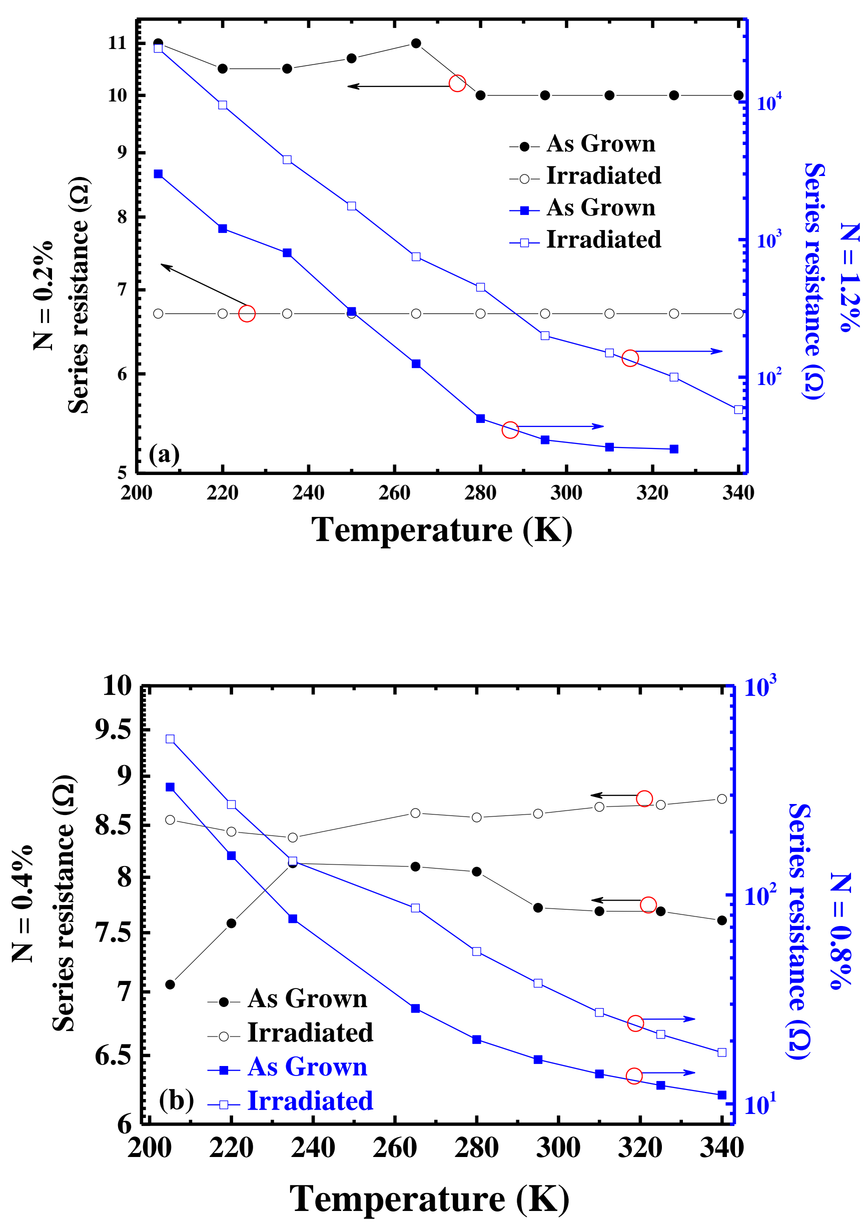

Fig. 7.8. Temperature dependence of the experimental series resistance (R_s), determined from I–V characteristics of as-grown and 50kGy gamma irradiated *n*-type MBE-grown GaAsN with nitrogen concentrations of (a) 0.2% and 1.2% and (b) 0.4% and 0.8%.

7.3.2 C-V CHARACTERISTICS

In order to determine the background doping concentration of dilute GaAsN samples with different nitrogen concentrations, the capacitance-voltage (C-V) measurements have been carried out at 300 K using the Boonton 7200 capacitance meter which operates at a frequency of 1 MHz as shown in Fig. 7.9. It can be seen from this figure that after irradiation the capacitance values decreased in all samples which could possibly be attributed to two main factors associated with irradiation; (i) the change in dielectric constant at the metal semiconductor interface or/and (ii) the reduction of net ionized dopant concentration [31-33].

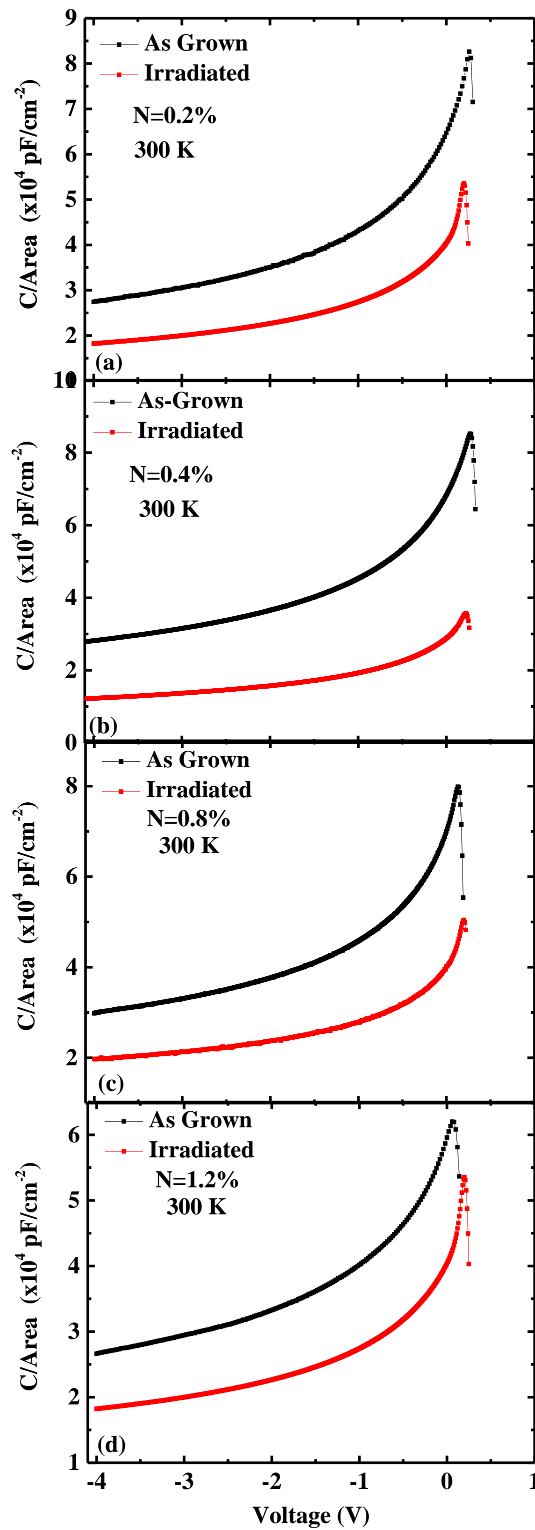

Fig. 7.9. C/Area–V characteristics of as-grown and irradiated samples with different nitrogen compositions at a frequency of 1MHz.

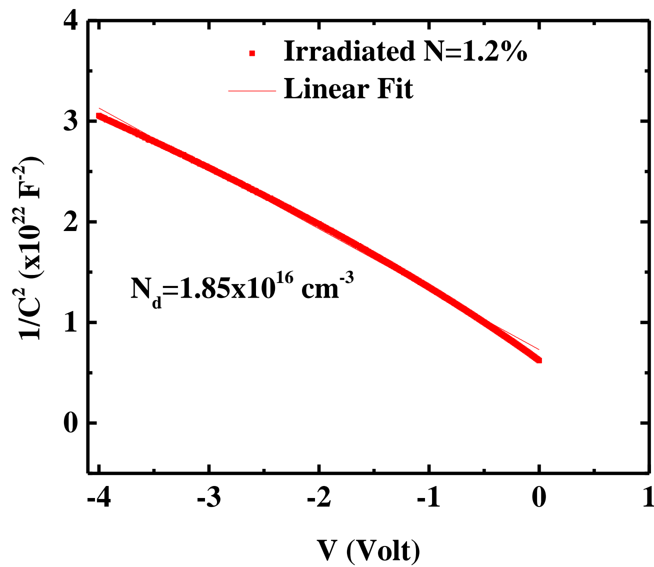

Fig. 7.10. The plot of the capacitance of irradiated GaAsN (N = 1.2%) samples in the form of $1/C^2$ as a function of reverse bias voltage.

Fig. 7.10 shows a typical $1/C^2$ versus reverse bias voltage plot obtained from the (C-V) data of an irradiated GaAsN sample with nitrogen concentration of N=1.2%. The doping concentrations for all samples were extracted from the slope of best fit of the plot of $1/C^2$ versus V at room temperature as described in Chapter 4 using Equation (4.26). The linear best-fit of the plot of $1/C^2$ versus V indicates the doping is uniform [13] over the bias range of -4V to 0V. The value of the doping concentration determined from the C-V measurements are used to calculate the trap concentration as described in Chapter 4 (Equation (4.42)). Fig. 7.11 shows the doping concentration variation with N content before and after irradiation. This figure indicates that the doping concentration for all samples decreases as a result of gamma irradiation. This reduction is normally related to the creation of defects upon irradiation. Thus, these defects trap conduction electrons and reduce the carrier concentration as well the capacitance values.

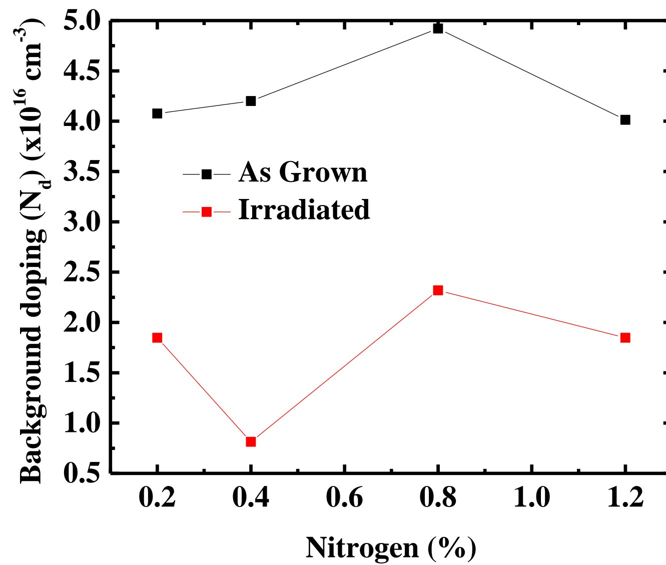

Fig. 7.11. The background concentration obtained from samples having different nitrogen contents.

7.3.3 DLTS AND LAPLACE DLTS CHARACTERISTICS

The DLTS measurements [34] were carried out on Schottky diodes to identify the electrically active defects created as a result of gamma irradiation. In addition, Laplace DLTS was used to separate the DLTS signals due to defects with closely spaced energy levels. The following experimental DLTS parameters are used: reverse bias $V_R = -4\ V$, filling pulse characteristics $V_p = -0.5\ V$, filling pulse duration $t_p = 1\ msec$. The samples were scanned from 10 K up to 450 K. In Fig. 7.12 we present the DLTS spectra, before and after irradiation, for samples with different nitrogen concentrations.

In a previous study, Shafi *et al*. [35] found for the same as-grown Schottky diodes that the number of electron defects decreases with increasing nitrogen content. In particular, they observed seven electron traps (A_1 to A_7) for diodes with N = 0.2%, four electron traps for both diodes with N = 0.4% (B_1 to B_4) and N = 0.8% (C_1 to

C_4) and three electron traps (D_1 to D_3) for diodes with N=1.2%, as listed in Table 7.2.

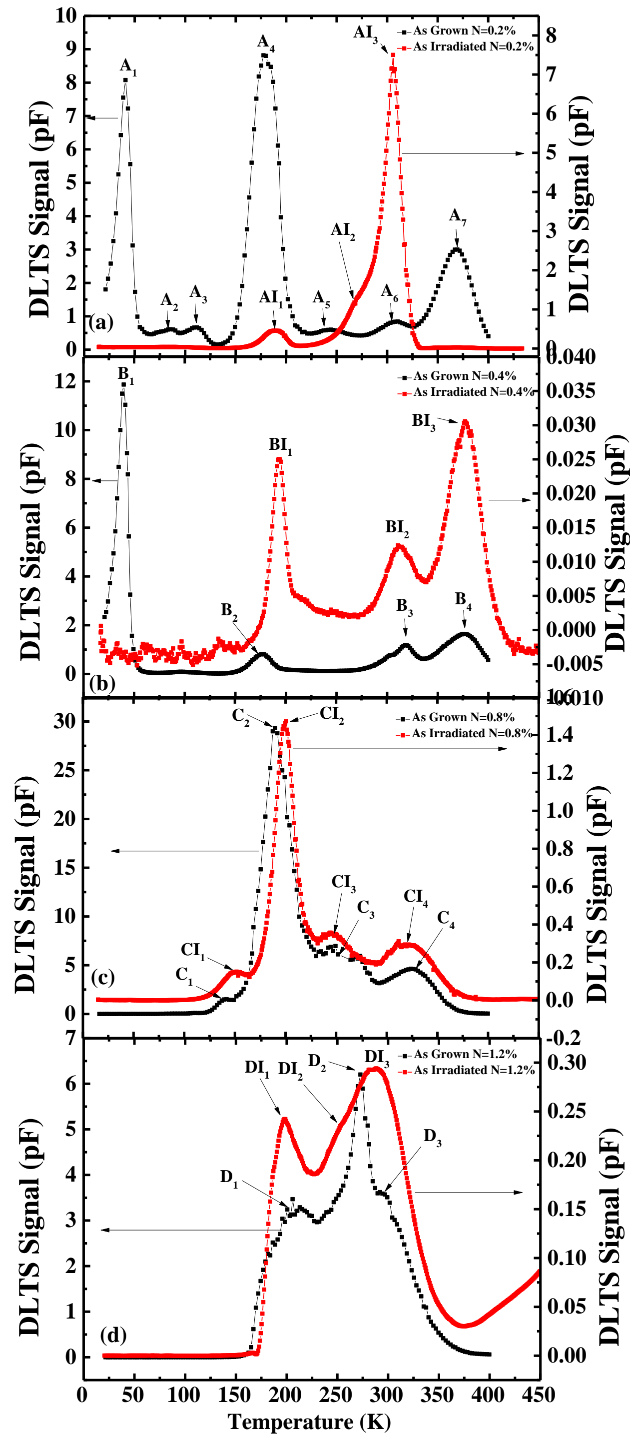

Fig. 7.12. Characteristic DLTS spectra of as-grown and irradiated samples with different nitrogen compositions obtained with reverse bias of -4V, filling pulse duration of *1 msec*, V_p of -0.5V, and rate window of $50s^{-1}$.

After irradiation, it is clear from Fig. 7.12 that, depending on the concentration of nitrogen, the number of traps decreases, remain constant or new traps have been created. Fig. 7.13 shows the Laplace DLTS spectra for the irradiated samples with the highest nitrogen composition (N = 1.2%), which was resolved from a very broad peak detected by conventional DLTS over the temperature range ~170-340K. In fact, the Laplace DLTS in the irradiated samples revealed the presence of three electron traps for both diodes with N = 0.2% (AI_1 to AI_3) and N=0.4% (BI_1 to BI_3), four electron traps for N=0.8% (CI_1 to CI_4) and three electron traps for N=1.2% (DI_1 to DI_3). Their activation energies, capture cross-sections, and concentrations were obtained from Arrhenius plots as shown in Fig. 7.14 and are summarized in Table 7.2. It is worth pointing out that for samples with N= 0.2% and N= 0.4% we observed a decrease in the number of traps after irradiation, whereas for samples with N = 0.8% and N= 1.2 % the number of traps did not change. However, the capture cross-sections and concentrations of some defects changed by about two orders of magnitude. Thus one should consider both the capture cross-sections and concentrations of the traps before coming to real conclusion.

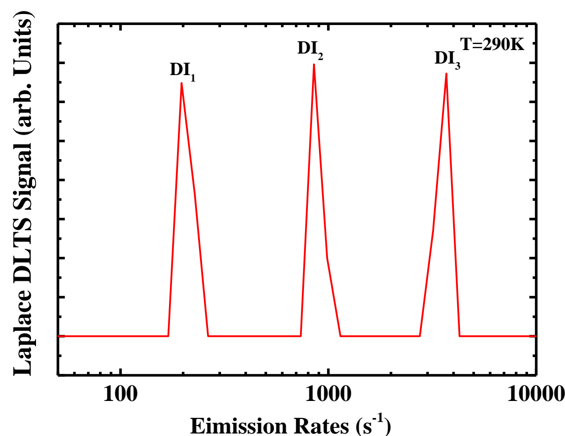

Fig. 7.13. Laplace DLTS spectra of the irradiated samples with N=1.2% taken at 290K. The experimental conditions used were similar to those used for the standard DLTS scans.

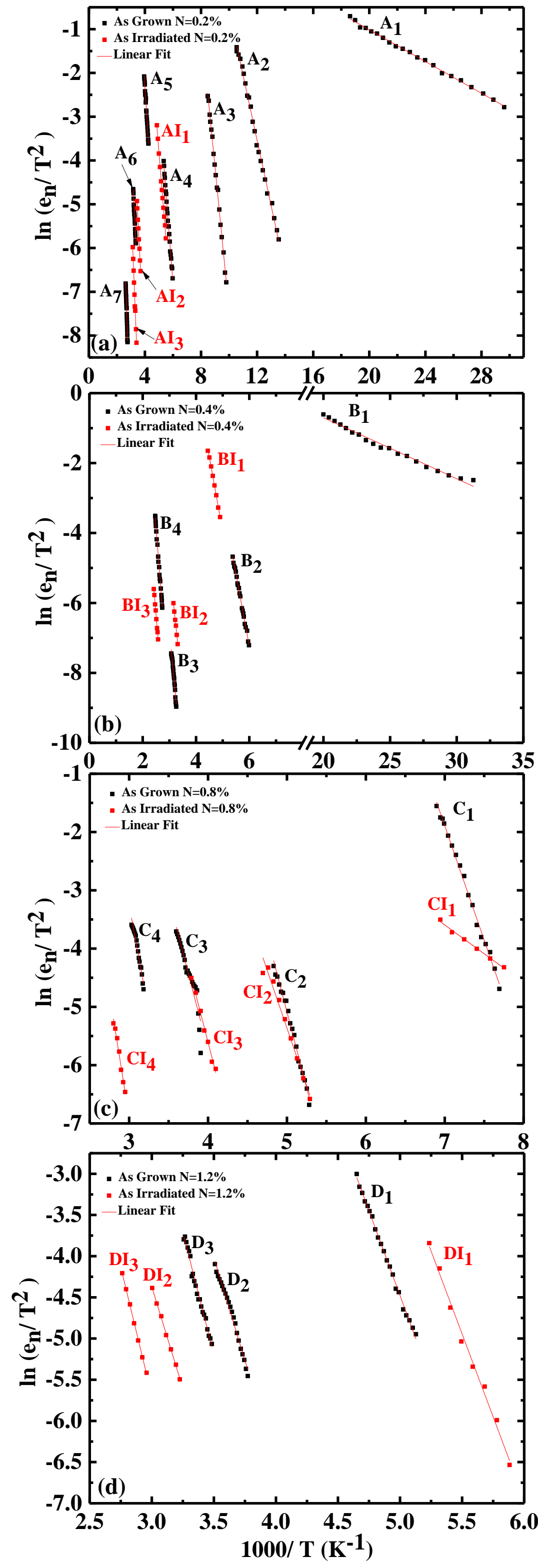

Fig. 7.14. Arrhenius plots for as-grown and irradiated samples with different nitrogen compositions obtained with reverse bias of -4V, filling pulse duration of *1 msec*, V_p of -0.5V, and rate window of $50 s^{-1}$.

Table 7.2. Summary of traps activation energies, capture cross-sections and concentrations for as-grown and irradiated samples.

X (%)	Trap label	E_T (eV)	σ_n (cm^2)	N_t (cm^{-3})
As-grown 0.2 %	A_1	0.036 ± 0.024	5.89×10^{-19}	2.03×10^{15}
	A_2	0.13 ± 0.03	1.07×10^{-18}	1.53×10^{14}
	A_3	0.28 ± 0.02	5.61×10^{-17}	1.68×10^{14}
	A_4	0.35 ± 0.01	8.21×10^{-16}	2.22×10^{15}
	A_5	0.43 ± 0.01	4.52×10^{-16}	1.50×10^{14}
	A_6	0.51 ± 0.03	5.28×10^{-16}	2.10×10^{14}
	A_7	0.81 ± 0.01	3.64×10^{-14}	7.56×10^{14}
Irradiated 0.2 %	AI_1	0.340 ± 0.003	5.37×10^{-14}	1.19×10^{15}
	AI_2	0.530 ± 0.002	9.93×10^{-14}	3.44×10^{15}
	AI_3	0.700 ± 0.005	1.52×10^{-12}	1.95×10^{16}
As-grown 0.4 %	B_1	0.045 ± 0.031	2.80×10^{-18}	3.60×10^{15}
	B_2	0.37 ± 0.03	5.75×10^{-16}	2.44×10^{14}
	B_3	0.53 ± 0.02	6.36×10^{-16}	3.52×10^{14}
	B_4	0.82 ±0.02	1.02×10^{-14}	5.07×10^{14}
Irradiated 0.4 %	BI_1	0.360 ± 0.003	1.74×10^{-14}	1.25×10^{14}
	BI_2	0.640 ± 0.003	1.57×10^{-14}	6.11×10^{13}
	BI_3	0.770 ± 0.003	5.45×10^{-15}	1.53×10^{14}
As-grown 0.8 %	C_1	0.34 ± 0.07	2.63×10^{-16}	1.86×10^{14}
	C_2	0.38 ± 0.03	4.24×10^{-16}	3.51×10^{15}
	C_3	0.44 ± 0.09	7.41×10^{-16}	6.97×10^{14}
	C_4	0.55 ± 0.01	5.51×10^{-16}	5.82×10^{14}
Irradiated 0.8 %	CI_1	0.085 ± 0.003	1.76×10^{-20}	1.83×10^{15}
	CI_2	0.35 ± 0.005	2.63×10^{-15}	1.78×10^{16}
	CI_3	0.43 ± 0.008	1.21×10^{-15}	4.30×10^{15}
	CI_4	0.72 ± 0.009	6.89×10^{-14}	3.55×10^{15}
As-grown 1.2 %	D_1	0.35	2.01×10^{-17}	1.69×10^{15}
	D_2	0.43	4.84×10^{-17}	3.02×10^{15}
	D_3	0.50	6.73×10^{-17}	1.74×10^{15}
Irradiated 1.2 %	DI_1	0.340 ± 0.007	1.29×10^{-14}	1.44×10^{15}
	DI_2	0.430 ± 0.002	2.72×10^{-17}	1.40×10^{15}
	DI_3	0.540 ± 0.001	2.86×10^{-16}	1.75×10^{15}

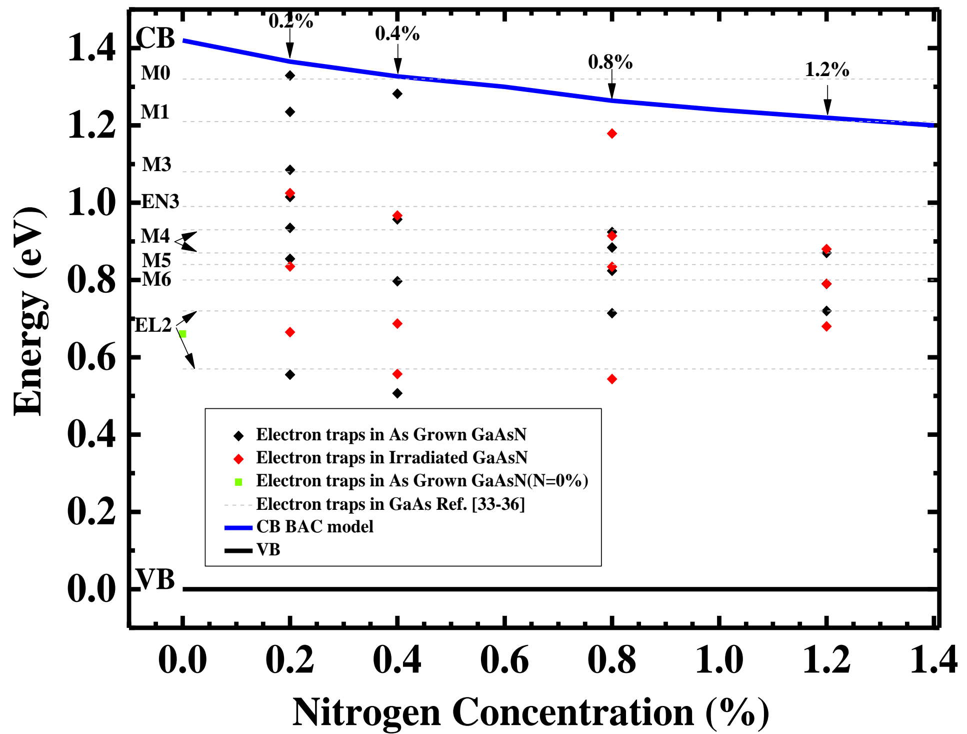

Fig. 7.15. Diagram showing the GaAsN bandgap as a function of nitrogen concentration. The electron traps energies, before and after irradiation as determined from the DLTS measurements, are also shown for each N composition. GaAs-like traps grown by MBE [36-39] is represented by the grey horizontal dashed lines.

The identification of the origin of these deep level traps is slightly difficult because when incorporating different nitrogen concentrations into the GaAs host crystal, the energies of these traps are considerably modified. However, Kudrawiec *et al.* [36] suggested an assumption based on the band anti-crossing (BAC) model [37] in order to reduce such effect. They assumed that the downward shift of the conduction band edge with no change of the energy of the valence band edge, creates a reduction of the band gap when the N concentration increases. Such assumption can be also used for defects in GaAsN alloys with low nitrogen

concentration (e.g., N < 1.25%). In fact, as explained by Kudrawiec *et al.*, the energy of the same defect in both GaAs and GaAsN alloys does not change relative to the valence band edge. Thus, as shown in Fig. 7.15, this supposition can be applied in this study to correlate the activation energies of the electron traps extracted from DLTS measurements for both as-grown and irradiated samples with different N percentages. Therefore, as the nitrogen concentration increases the activation energy of a specified electron trap should decreases with same amount of the reduction in the conduction band of GaAsN. This means that the energetic positions of the traps with the same origin should be located near a certain horizontal line.

As illustrated in Fig. 7.15, the solid blue line represents the conduction band (CB) minimum for GaAsN alloys which was estimated by the BAC model as a function of nitrogen concentration and redrawn from Fig. 2 in Ref. [38]. The valence band (VB) maximum of this alloy is adjusted to zero and illustrated as a black solid line. Also in Fig. 7.15 are included the activation energies of electron traps of as-grown and irradiated diodes relative to the edge of the CB. Trap parameters for a control sample with N=0% is also shown with an activation energy of 0.76 eV, capture cross section of 5.15×10^{-14} cm^2 and trap concentration of 2.85×10^{15} cm^{-3} [9]. Furthermore, the estimated energetic positions in GaNAs band gap of well-known GaAs-like traps reported previously in n-type GaAs grown by MBE [39-43] are plotted in Fig. 7.15 as horizontal dashed grey lines. These lines are illustrated to identify the relation between these traps and the electron traps in GaAsN. It is clear that the shallow traps (A_1 and B_1) that exist only in as-grown diodes with low N concentration (N $\leq$ 0.4 %) can be related to the well-known electron trap in GaAs, M0 (E_c-0.10 eV) [39]. After irradiation this trap was annihilated in both samples.

The A_2 trap in the diode with N = 0.2%, has energy similar to the well-known M1 (E_C-0.21 eV) trap in n-GaAs trap [39], but under irradiation this trap was also annihilated. However, the M1 trap was observed in irradiated samples with higher nitrogen concentration (N=0.8%, CI_1 trap) but with a concentration one order of magnitude higher than A_2 trap concentration. Additionally, the M1 trap is comparable to the low-energy EL10 trap in GaAs MBE grown samples [43] which was assigned to an arsenic vacancy (V_{As}) complex defect involving an impurity [39, 44]. The trap A_3 is observed solely in as-grown samples with the lowest N concentration and as a result of irradiation it is annihilated. This trap can be assigned to M3 (E_C-0.34 eV) [42] which has the same signature as trap EL6 [45]. The nature of EL6 is related to the complex defect involving arsenic antisite defect (As_{Ga}) and arsenic vacancy (V_{As}) [45]. In addition, the traps A_4, AI_1, B_2 and BI_1 (~ E_C- 0.43 eV) have the same activation energy as EN3 in GaAs [46, 47]. The EN3 trap is only detected with lower nitrogen content (N ≤ 0.4%). After irradiation, the capture cross section increases about two orders of magnitude for both samples with N = 0.2% and N = 0.4%. However, the trap concentrations decrease by a factor of two for the samples with N = 0.2% and 0.4% as a result of irradiation. Furthermore, the A_5, C_1, C_2, CI_2, D_1 and DI_1 traps are likely to correspond to the same level M4, whose activation energy varies widely in the range from E_C-0.49 eV to E_C-0.55 eV [40] and has same origin as the level EL4. The EL4 level was also attributed to an arsenic vacancy (V_{As}) complex involving an impurity [44]. It is worth to note that this trap present in structures with higher concentration of N (N =1.2%) is not affected by irradiation while for structures with lower concentration, it is annihilated by irradiation. In addition, the capture cross-section and concentration of the EL4 trap increases with irradiation. For example, the

diodes with N= 0.8% the capture cross section and concentration increase by one and two order of magnitude, respectively. But for the diodes with N= 1.2% the capture cross section increases by three orders of magnitude but its concentration remains almost unchanged. Thus the increase of the barrier height for the sample with N-concentration of 0.8% after irradiation could probably be due to the fact that traps C_1 or C_2 was annihilated, and an emerging a new defect (CI_1) with lower energy and capture cross-section. A_6, AI_2, C_3 and CI_3 traps can be related to the M5 level (E_C-0.58 eV) [39]. Also this level has similar origin to EL3. This famous trap is commonly associated to the off-center substitutional oxygen on arsenic sites (oc-O_{As}) [48]. It is worth taking into consideration that the capture cross section and concentration of this trap increased by one order of magnitude after irradiation. The deep level electron traps B_3, D_2 and DI_2 are detected only in as-grown diodes with N = 0.4% and as-grown and irradiated samples with N=1.2%, respectively. These traps have approximately their activation energies close to the trap M6 (E_C-0.62 eV) [39]. M6 trap is typically observed in GaAs layers grown by MBE. In this study, M6 trap resists to irradiation in samples with higher nitrogen concentration (N= 1.2%) while for lower nitrogen concentration (N= 0.8%) this defect is annihilated when subjected to irradiation. Furthermore, the D_2 and DI_2 traps have lower capture cross section and higher concentrations (samples with N = 1.2%) compared to B_3 (samples with N=0.4%). A_7, AI_3, B_4, BI_2, BI_3, C_4, CI_4, D_3 and DI_3 are the deepest traps observed consistently in all samples. These traps could be related to the famous EL2 trap in GaAs layers. This defect typically has an energy in the range of 0.70 eV to 0.85 eV [49] and its origin is assigned to the isolated arsenic antisite defect (As_{Ga}) or complex defect involving As_{Ga} and arsenic interstitial [50]. B_4 defect is unique in the sense that both its capture cross section

and concentration decrease after irradiation (see BI_3 parameters in Table 7.2), which is compared to the other EL2 traps in this study. Thus this reduction is probably indicating that the origin of EL2 is related to defects which may be easily created or decomposed by various surrounding conditions. On the other hand, if we sum the capture cross-sections of B_1+B_2+B_3 ~ 9 × 10^{-16} cm^2 (before irradiation) that is about two orders of magnitude lower than BI_1 + BI_2 ~ 3.2 ×10^{-14} cm^2 (after irradiation).This behavior has strong effect on the obvious increment of the leakage current after irradiation in GaAsN with N = 0.4% (Fig. 7.2 (b)).

M0, M1, M3, EN3, M4, M5 and M6 traps that have been identified in this work can be related indirectly with the incorporation of N atoms since they are not detected in the untreated control sample (N=0%). The solely trap found in this control sample has the same origin as EL2 trap. Thus, the only trap which can be directly associated with GaAs is EL2. However, EL2, EL3, EL6 and EN3 are also experimentally detected in GaAsN or GaInNAs structures [48, 51-54].

7.4 CONCLUSION

We have used I-V, C-V, DLTS and Laplace DLTS to investigate the effect of gamma irradiation in GaAsN samples grown by MBE with different nitrogen concentrations (0.2% to 1.2%). The I-V characteristics show that the deterioration of the electrical properties of GaAsN with nitrogen concentrations of 0.2, 0.4 and 1.2% after irradiation could possibly be attributed to the increase of the concentration and/or capture cross-section values of major defects detected by DLTS and Laplace DLTS measurements. However, the samples with 0.8% nitrogen concentration exhibited higher resistance to γ-irradiation effect than other devices. Moreover, the C-V measurements at 1 MHz indicate that there is a slight

reduction in carrier concentration for all samples due to irradiation-induced defect. In addition, the DLTS and Laplace DLTS reveal close connection between the grown-in defects and the radiation-induced ones. The structures with higher concentration of N showed the best radiation resistance.

REFERENCES

[1] M. Milanova, R. Kakanakov, G. Koleva, B. Arnaudov, S. Evtimova, P. Vitanov, E. Goranova, V. Bakardjieva and Z. Alexieva, J. of Optoelectronics and Adv.anced Mater. **11** (10), 1471 (2009).

[2] K. Ryczko, G. Sęk, J. Misiewicz, F. Langer, S. Höfling and M. Kamp, J. Appl. Phys. **111** (12), 123503 (2012).

[3] S. R. Kurtz, A. Allerman, E. Jones, J. Gee, J. Banas and B. Hammons, Appl. Phys. Lett. **74** (5), 729 (1999).

[4] N. Tansu, N. J. Kirsch and L. J. Mawst, Appl. Phys. Lett. **81** (14), 2523 (2002).

[5] J. Harris Jr, Semicond. Sci. Technol. **17** (8), 880 (2002).

[6] S. Pearton, F. Ren, A. Zhang and K. Lee, Mater. Sci. Eng: R: Reports **30** (3), 55 (2000).

[7] S. Zhang and S.-H. Wei, Phys. Rev. Lett. **86** (9), 1789 (2001).

[8] B. Bouzazi, N. Kojima, Y. Ohshita and M. Yamaguchi, Curr. appl. Phys. **13** (7), 1269 (2013).

[9] M. Shafi, R. Mari, M. Henini, D. Taylor and M. Hopkinson, Phys. Status Solidi (c) **6** (12), 2652 (2009).

[10] T. Hashizume and H. Hasegawa, J. of Appl. Phys. **68** (9), 4598 (1990).

[11] G. Umana-Membreno, J. Dell, G. Parish, B. Nener, L. Faraone and U. Mishra, Electron Devices, IEEE Transactions on **50** (12), 2326 (2003).

[12] S. K. Khamari, V. Dixit, T. Ganguli, S. Porwal, S. Singh, S. Kher, R. Sharma and S. Oak, Nucl. Instrum. and Methods in Phys. Res. Sect. B: Beam Interact. with Mater. and Atoms **269** (3), 272 (2011).

[13] S. M. Sze and K. K. Ng, *Physics of semiconductor devices*. (Wiley. com, 2006).

[14] M. Biber, C. Coşkun and A. Türüt, The Eur. Phys. J. Appl. Phys. **31** (02), 79 (2005).

[15] J. H. Werner, Applied physics A **47** (3), 291 (1988).

[16] B. Şahin, H. Çetin and E. Ayyildiz, Solid State Commun. **135** (8), 490 (2005).

[17] M. A. Ebeoglu, F. Temurtas and Z. Z. Ozturk, Solid-State Electron. **42** (1998).

[18] R. Tung, J. Sullivan and F. Schrey, Mater. Sci. Eng., B **14** (3), 266 (1992).

[19] E. H. Rhoderick and R. Williams, (1988).

[20] V. Narayanamurti, M. Kozhevnikov, H. Xin, C. Tu, A. Mascarenhas and Y. Zhang, Add. to The Proc. NCPV Program Rev. Meet., Denver Colo., (2000).

[21] M. Mamor, A. Sellai, K. Bouziane, S. Al Harthi, M. Al Busaidi and F. Gard, J. Phys. D: Appl. Phys. **40** (5), 1351 (2007).

[22] Ö. Güllü, F. Demir, F. Cimilli and M. Biber, Vac. **82** (8), 789 (2008).

[23] R. Tung, Phys. Rev. B **45** (23), 13509 (1992).

[24] K. Ejderha, A. Zengin, İ. Orak, B. Tasyurek, T. Kilinç and A. Turut, Mater. Sci. Semicond. Process. **14** (1), 5 (2011).

[25] D. Korucu, A. Turut and H. Efeoglu, Phys. B: Condens. Matter **414**, 35 (2013).

[26] N. Yildirim, H. Korkut and A. Türüt, The Eur. Phys. J. Appl. Phys. **45** (01), 10302 (2009).

[27] M. Hudait, P. Venkateswarlu and S. Krupanidhi, Solid-State Electron. **45** (1), 133 (2001).

[28] A. Tataroglu, S. Altindal, F. Pur, T. Ataseven and S. Sezgin, Optoelectronics and Adv. Materials-Rapid Commun. **5** (3-4), 438 (2011).

[29] O. Donmez, F. Sarcan, S. Lisesivdin, M. Vaughan, A. Erol, M. Gunes, M. Arikan, J. Puustinen and M. Guina, Semicond. Sci. Technol. **29** (12), 125009 (2014).

[30] F. Auret, S. Goodman, G. Myburg and W. Meyer, J. Vac. Sci. Technol., B **10** (6), 2366 (1992).

[31] P. Żukowski, J. Partyka and P. Węgierek, physica status solidi (a) **159** (2), 509 (1997).

[32] Ş. Karataş, A. Türüt and Ş. Altındal, Nuclear Instruments and Methods in Physics Research Section A: Accelerators, Spectrometers, Detectors and Associated Equipment **555** (1), 260 (2005).

[33] M. Nishiguchi, T. Hashinaga, H. Nishizawa, H. Hayashi, N. Okazaki, M. Kitagawa and T. Fujino, Nuclear Science, IEEE Transactions on **37** (6), 2071 (1990).

[34] D. Lang, Journal of Applied Physics **45** (7), 3023 (1974).

[35] M. Shafi, R. Mari, A. Khatab, M. Henini, A. Polimeni, M. Capizzi and M. Hopkinson, J. Appl. Phys. **110** (12), 124508 (2011).

[36] R. Kudrawiec, M. Latkowska, M. Welna, J. Misiewicz, M. Shafi, R. Mari, M. Henini and W. Walukiewicz, Appl. Phys. Lett. **101** (8), 082109 (2012).

[37] W. Shan, W. Walukiewicz, J. Ager III, E. Haller, J. Geisz, D. Friedman, J. Olson and S. R. Kurtz, Phys. Rev. Lett. **82** (6), 1221 (1999).

[38] J. Wu, W. Shan and W. Walukiewicz, Semicond. Sci. Technol. **17** (8), 860 (2002).

[39] D. V. Lang, A. Y. Cho, A. Gossard, M. Ilegems and W. Wiegmann, Journal of Applied Physics **47** (6), 2558 (1976).

[40] R. DeJule, M. Haase, G. Stillman, S. Palmateer and J. Hwang, J. Appl. Phys. **57** (12), 5287 (1985).

[41] A. Kitagawa, A. Usami, T. Wada, Y. Tokuda and H. Kano, J. of Appl. Phys. **65** (2), 606 (1989).

[42] R. F. Farrow, *Molecular beam epitaxy: applications to key materials*. (Elsevier, 1995).

[43] G. Martin, A. Mitonneau and A. Mircea, Electronics Letters **13** (7), 191 (1977).

[44] P. Blood and J. Harris, Journal of Applied Physics **56** (4), 993 (1984).

[45] K. Yokota, H. Kuchii, K. Nakamura, M. Sakaguchi, H. Takano and Y. Ando, Journal of Applied Physics **88** (9), 5017 (2000).

[46] E. K. Kim, H. Y. Cho, H. S. Kim, S.-k. Min and T. Kim, Semicond. Sci. Technol. **7** (5), 695 (1992).

[47] H. Y. Cho, E. K. Kim, S. K. Min, J. B. Kim and J. Jang, Appl. Phys. Lett. **53** (10), 856 (1988).

[48] A. Polyakov, N. Smirnov, A. Govorkov, A. E. Botchkarev, N. N. Nelson, M. Fahmi, J. A. Griffin, A. Khan, S. Noor Mohammad and D. Johnstone, Solid-State Electron. **46** (12), 2155 (2002).

[49] J. Bourgoin and T. Neffati, Solid-State Electron. **43** (1), 153 (1999).

[50] M. Kaminska and E. R. Weber, Semiconductors and Semimetals **38**, 59 (1993).

[51] M. Shafi, R. Mari, A. Khatab, M. Henini, A. Polimeni, M. Capizzi and M. Hopkinson, J. Appl. Phys. **110** (12), 124508 (2011).

[52] Ł. Gelczuk, R. Kudrawiec and M. Henini, J. Appl. Phys. **116** (1), 013705 (2014).

[53] S. Tanaka, A. Moto, M. Takahashi, T. Tanabe and S. Takagishi, J. Cryst. Growth **221** (1), 467 (2000).

[54] I. Buyanova, W. Chen and C. Tu, J. Phys.: Condens. Matter **16** (31), S3027 (2004).

CHAPTER 8: ANALYSIS OF DEEP LEVEL DEFECTS IN GaN P-I-N DIODES AFTER BETA PARTICLE IRRADIATION GROWN BY METAL ORGANIC VAPOUR PHASE EPITAXY

This Chapter reports the effect of beta particle irradiation (electron energy 0.54 MeV) on the electrical properties of betavoltaic microbattery based on a GaN p–i–n homojunction structure with the undoped layer (i-GaN) having thicknesses of 200 nm and 600 nm. In addition, the impact of the irradiation on the formation of both shallow and deep energy level defects will be described. Current-Voltage (I-V), Capacitance-Voltage (C-V) and Deep Level Transient Spectroscopy (DLTS) measurements were performed on both as-grown and irradiated devices.

8.1 INTRODUCTION

In the last few decades, the micro-electro-mechanical system (MEMS) technology has been rapidly developed for use in the majority of electrical and mechanical devices such as sensors, actuators and biomedical devices in the size of millimeter to micrometer and even nanometer scale [1, 2]. MEMS technology requires small size and higher energy density power supplies to drive these devices. However, when the size of the power is reduced, the amount of stored energy goes down exponentially. Thus, the trade-off between size and power density of power supplies [2] is considered as a big challenge in MEMS technology to be employed for portable and durable devices in both normal and extreme environments (i.e. high temperature and pressure, and in space and harsh environments). Consequently it is becoming very essential to develop power sources with high

energy density, light weight, insensitive to climate and temperature, and long life time compatible (for long-term applications) for use in MEMS technology [1]. Betavoltaic microbattery is one type of nuclear microbatteries that is considered to be a promising technology to satisfy these requirements [3].

The operation principle of a betavoltaic microbattery is similar to that of a photovoltaic cell. In a photovoltaic cell, electron-hole pairs (EHPs) are generated when photons strike the semiconductor p-n junction causing an electrical current to flow. In betavoltaic cells, EHPs are generated when energetic beta electrons emitted from the radioactive source strike the p-n junction diode instead of photons causing an electrical current to flow. In comparison with a photon exciting an EHP, a beta particle can generate tens of thousands of EHPs. Along the beta particles moving trajectory, the carriers generated in the depletion region and the n or p region near the depletion boundary with a width less than the carrier diffusion length can be collected. As a result, the kinetic energy of the beta particles is harvested and converted into electrical energy.

In 1954, Rappaport [4] reported the first semiconductor p-n betavoltaic cell for conversion of nuclear radiation into electricity. Subsequently, a series of semiconductor materials such as silicon (Si), porous silicon, and silicon carbide (SiC) [4-8] have been investigated for betavoltaic microbatteries. However, most of these fabricated devices have low current densities and energy conversion efficiencies, which are much lower than the expected ones. For example, Sun *et al.* [9] did not achieve a high enough current density in their betavoltaic cell diodes which consisted of a three-dimensional porous silicon irradiated with tritium sources. In 2006, Eiting *et al.* [8] achieved high energy conversion efficiency in SiC-based betavoltaic cells irradiated with krypton-85 source. However, their

diodes degraded due to the creation of large amounts of defects in SiC. Theoretical analysis show that, when the band gap of a semiconductor increases, the efficiency of betavoltaic conversion increases [10]. Thus, the semiconductor GaN could be a more attractive material for betavoltaic microbattery owing to its wide band gap (3.4 eV) compared to Si (band gap of 1.12 eV) and SiC (band gap of 2.3–3.3 eV) [11].

It is well known that both optically and electrically active defects are introduced when semiconductor surfaces are exposed to energetic particles [12]. Thus, the effect of high energy radiation on the material properties of GaN has been studied by different groups. Linde et *al.* [13] found that, two broad photoluminescence bands were introduced in a 1 µm thick GaN/Al_2O_3 layer as a result of 2.5 MeV electrons irradiation. In Look et *al.* [14] experiment, GaN was irradiated with 0.7–1.0 MeV electrons and from Hall measurements they detected a nitrogen vacancy at 0.07 eV below the conduction band of GaN. The charge trapping characteristics of electron irradiation induced defects have been reported by Fang et *al.* [15] using DLTS measurements. They found the creation of an electron defect labelled E, with a thermal activation energy of 0.18 eV.

In this work, an experimental study is presented to examine the radiation damage of β-particles (electrons with energies less than ~1 MeV) in GaN p-i-n diodes grown by metal-organic vapour phase epitaxy (MOVPE) technique and their effect in the creation of both shallow and deep energy level defects. The defects induced in the devices can create deep level recombination centers in the depletion region and therefore decrease the collection rate of generated EHPs, reducing thereby the efficiency of betavoltaic battery. Moreover, the energy levels of the defect states in the bandgap were measured by using DLTS, a powerful tool for probing the defect

states of p-i-n junction diode structures [16] together with I-V and C-V measurements.

8.2 SAMPLE DETAILS

In this work, two GaN p-i-n structures with different thicknesses of the (i-GaN) undoped layer were investigated. The main motivation to use these structures is to investigate the change of efficiency of betavoltaic conversion as a result of changing the thickness of the i-GaN region. When the thickness of the i-GaN layer is varied, the amount of EHPs generation is expected also to change. Hence, the efficiency of betavoltaic conversion is affected [3]. Moreover, by changing the thickness of the i-GaN will allow us to study the depletion region of the GaN p-i-n junction in both i-side and p-side using DLTS measurements.

An MOVPE system was used to grow the p-i-n GaN samples on 2 inch c-plane sapphire (Al_2O_3) substrates. Firstly, a 2 µm GaN nucleation layer was grown on sapphire substrate as a buffer layer to stop the propagation of defects arising from the lattice mismatch between sapphire and GaN epitaxial layers. This was followed by a 0.15 µm-thick Si heavily doped n-GaN layer with a doping concentration of 3×10^{18} cm^{-3}. Then, an intrinsic region of undoped GaN layer was grown with thickness of 0.2 µm and 0.6 µm for sample S1 and S2, respectively. Finally a 0.15 µm thick Mg-doped p-GaN with a doping concentration of ~ 5×10^{17} cm^{-3} was grown to form the p-i-n device.

The samples were irradiated by a 1 MBq ^{90}Sr-^{90}Y radioisotope (1 cm^3 liquid source) contained into a flamed sealed glass ampoule (a maximum beta decay energy of 546 keV) for one week. For the radioactive isotope ^{90}Sr (electron energy 546 keV), the electron penetrates the whole layer of GaN (thickness < 1 µm). At this energy,

the path should be several mm into the GaN. The decay products ^{90}Y at the balance with its parents (^{90}Sr) will have a maximum energy of 2.28 MeV. The path will therefore be more even important. Fig. 8.1 shows the typical structure of the devices investigated in this work including details of the epitaxial layers. All device processing was carried out using standard semiconductor fabrication techniques that include photolithography, dry etching process to form the mesa structure, and metallization to fabricate the Ohmic contacts to the p and n-type layers of the GaN p-i-n diodes. The mesa etching was performed using an inductively coupled plasma (ICP) etching method. Prior to metal deposition, the samples were cleaned in HCl: HNO_3 (3: 1) for 10 mins to remove the native gallium oxide. The p- and n-type Ohmic contact electrodes were Pd/Au (20 nm/120 nm) and Ti/Al/Au (10 nm/30 nm/300 nm), respectively. These Ohmic contact electrodes were deposited by using an electron beam evaporation system with a base pressure lower than 1 x 10^{-7} Torr. Fig. 8.1 (c) shows a photograph of different-diameter mesa after processing. It is worth to mention that the samples growth and processing were done by S. Belahsene (National Centre for Scientific Research, France).

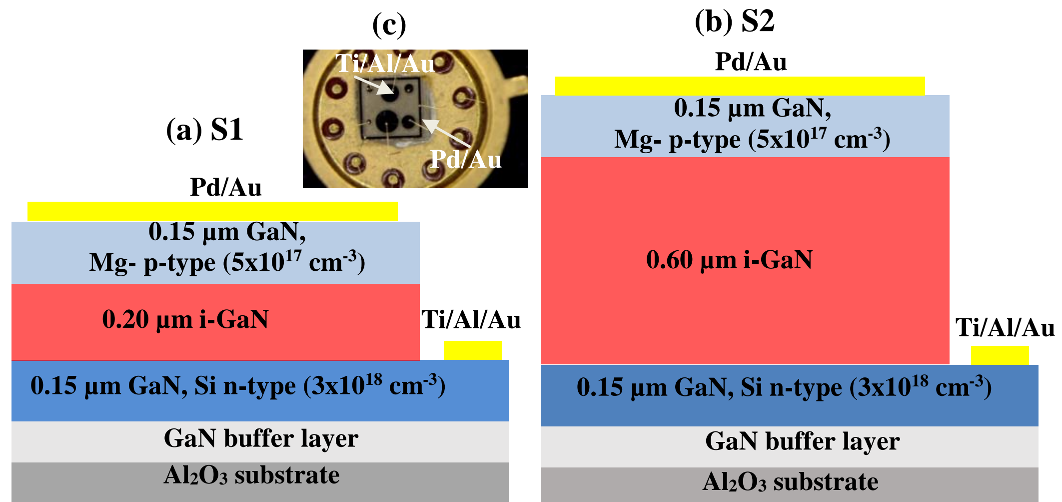

Fig. 8.1. Schematic diagram of the GaN p-i-n junction diode with (a) 0.2 µm undoped GaN layer (S1), (b) 0.6 µm undoped GaN layer (S2) and (c) Photograph of different-diameter mesa p-i-n diodes after processing.

8.3 RESULTS AND DISCUSSION

In order to study the effect of beta particle irradiation (electron energy 0.54 MeV) on the electrical properties of GaN p-i-n diodes I-V, C-V and DLTS measurements were performed.

8.3.1 I-V MEASUREMENTS

The room temperature dark current density (J)–voltage characteristics were measured for as-grown and irradiated S1 and S2 samples as illustrated in Fig. 8.2. From the *J-V* characteristics at room temperature, it is absolutely clear that the decrease of the thickness of the i-GaN region enhances the forward current density. However, the reverse current density is not affected by the change of the thickness. The reverse-bias leakage current at – 4 V is 0.09 A/cm^2 for both samples S1 and S2. It was reported that the leakage current occurs through the volume of the device [17, 18].

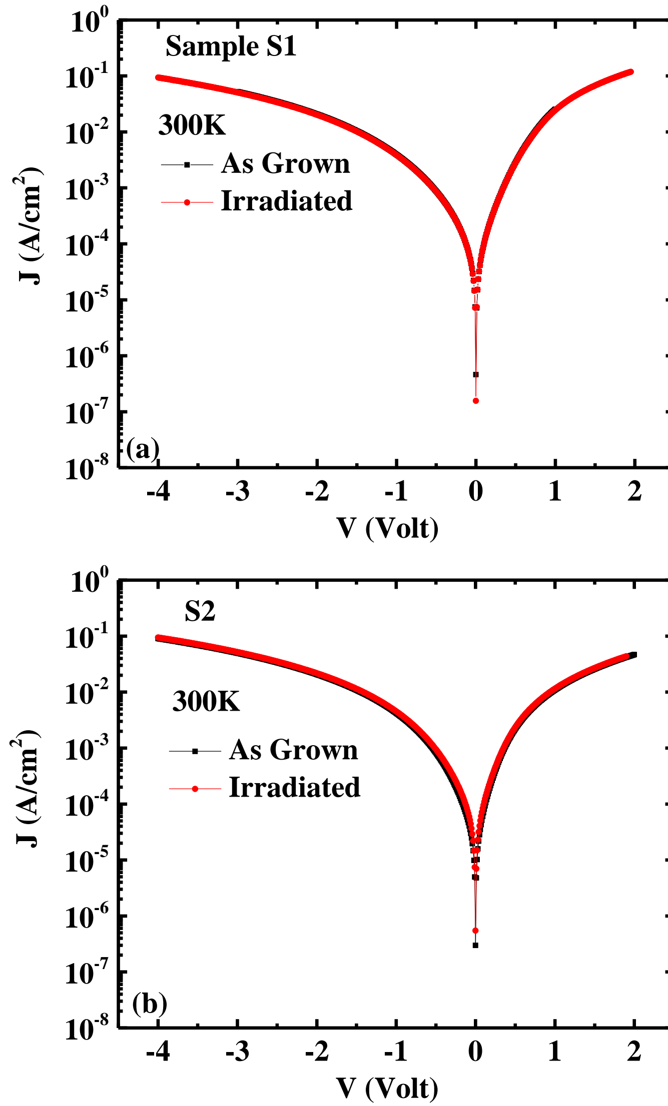

Fig. 8.2. Semi-logarithmic plots of dark J–V characteristics of as-grown and irradiated GaN p–i–n junction diodes with thicknesses of undoped layer of (a) 200 nm (S1) and (b) 600 nm (S2) at room temperature. The diameter of the diodes is 1000µm.

The I–V characteristics of ideal diodes is normally described by the thermionic emission of conduction electrons [19]:

$$I = I_0 \left[exp\left(\frac{q(V - IR_S)}{nk_B T} \right) - 1 \right] \qquad (8.1)$$

where q is the electronic charge, V is the applied voltage, R_s is series resistance, k_B is the Boltzmann constant, n is the ideality factor, I_0 is the saturation current, and T is the absolute temperature in Kelvin. The values of n and I_0 are determined from the experimental data. The saturation current I_0 is given by:

$$I_0 = AA^{**}T^2 exp\left(\frac{-q\phi_B}{k_B T}\right) \qquad (8.2)$$

where A is the diode area and A^{**} is the effective Richardson's constant for the semiconductor, and ϕ_B is the barrier height.

The electrical properties of the diodes were determined by the method developed by Werner [20] as described in Chapter 4. This method includes plotting the conductance divided by current (G/I) versus conductance (G) as shown in Fig. 8.3 for both S1 and S2 samples.

The value of the ideality factor of S1 and S2 samples is n = 5.5 and n=5.4, respectively. These values are the same for both as-grown and irradiated samples. These fairly high ideality factors indicate that besides thermionic emission other mechanisms such as recombination, and tunnelling also contribute to the carriers transport.

From the electrical point of view, the n values not altering much is an indication that β-particles irradiation is not causing the formation of recombination centres in GaN p-i-n samples.

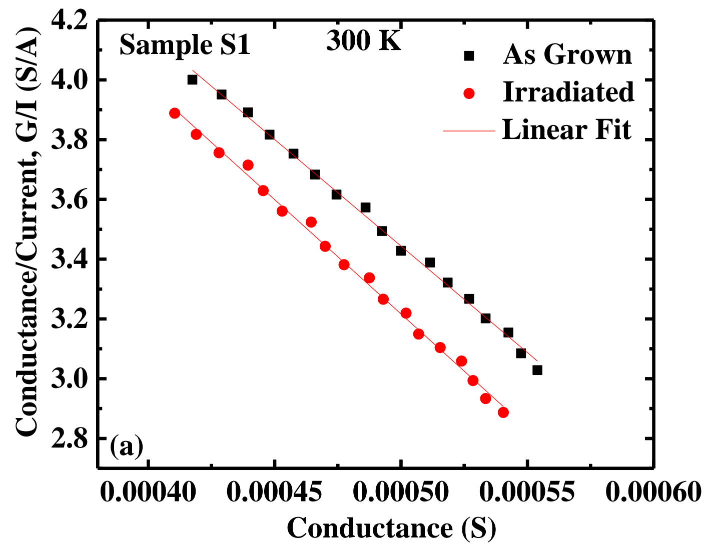

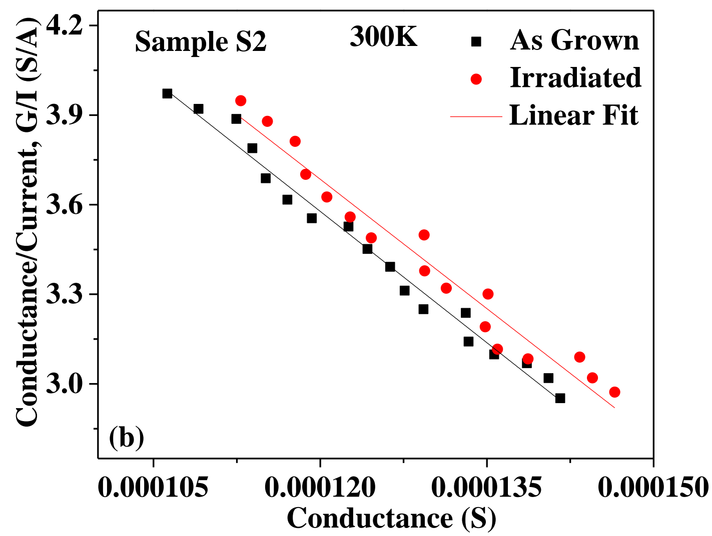

Fig. 8.3. G/I-G plot obtained from the room temperature I-V curves at forward bias voltages for as-grown and irradiated GaN p–i–n diodes with the i-GaN layer having a thickness of (a) 200 nm (S1 samples) and (b) 600 nm (S2 samples).

8.3.2 C-V MEASUREMENTS

The C-V measurements were performed at room temperature with a frequency of 1 MHz for all GaN diodes as shown in Fig. 8.4. From this figure, it can been seen that the value of the capacitance for sample S2 reveales a small reduction as a result of the irradiation. On the other hand, the measurements of the capacitance for sample S1 exhibits a significant effect because of β-particles as clearly seen in Fig. 8.4 (a). In particular, in the investigated bias range, a large variation of capacitance, in the order of 30 pF, is observed in the irradiated sample S1 compared with the as-grown sample S1 where the variation is only 10 pF. The reduction of the capacitance values for samples S1 and S2 after irradiation could be attributed to the effects of carrier removal by the traps created in the depletion region. These traps reduce the concentration of free carriers by capturing them.

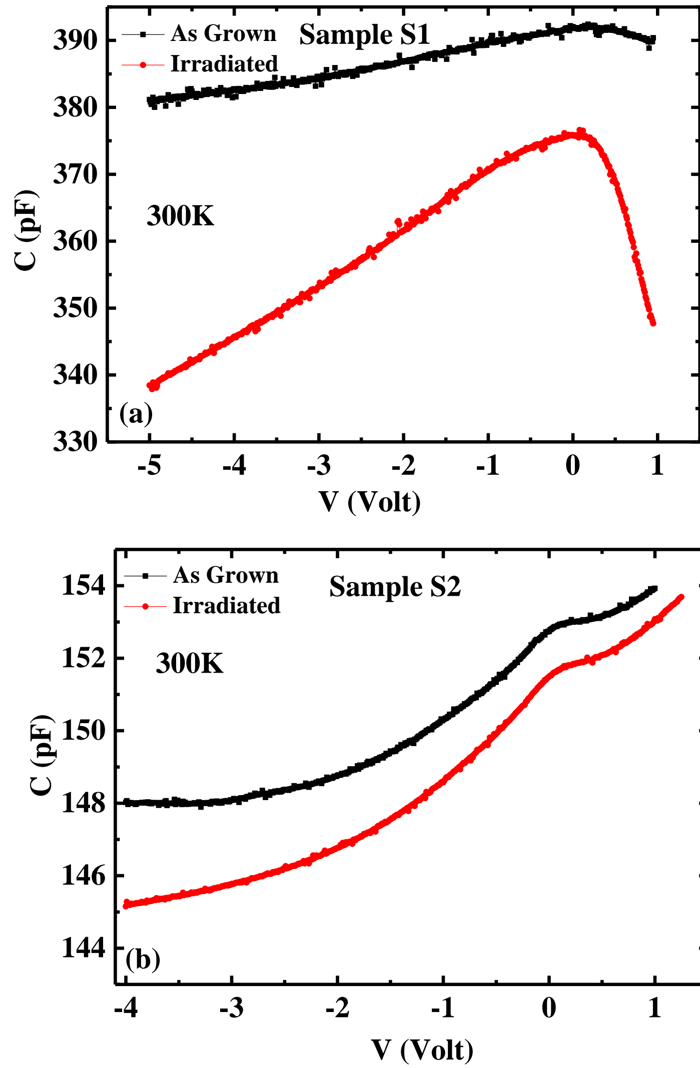

Fig. 8.4. Typical C-V characteristics at 1 MHz for as-grown and irradiated (a) S1 and (b) S2 samples.

Fig. 8.5 illustrates typical 1 /C^2 versus bias voltage obtained from the (C-V) data of as-grown and irradiated S1samples. The relation between capacitance and voltage is given by equation (8.3) [21]:

$$\frac{1}{C^2} = \frac{d^2}{(\varepsilon_s \varepsilon_0 A)^2} + \frac{2}{q\varepsilon_s \varepsilon_0 A} \frac{N_d + N_a}{N_d N_a} (V_{bi} - V_r) \qquad (8.3)$$

where A is the diode area (cm^2), d is the thickness of the undoped layer (cm), V_r is the applied bias (V), q is the electronic charge (C), ε_s is the permittivity ($F.cm^{-1}$) of

GaN (9.5ε_0), V_{bi} is the built-in voltage (V). N_d and N_a represent the free electron and hole concentration (cm^{-3}), respectively. The ratio of ($N_a.N_d/N_a+N_d$) was used to estimate the net free carrier concentrations which were extracted from the slope of best fit of the plot of $1/C^2$ versus V at room temperature and the values are used to calculate the trap concentration as described in Chapter 4 (Equation (4.26)). It is worth pointing out that the linear best fit of the plot of $1/C^2$ versus V indicates that the doping is uniform [22] over the bias range of -4V to 0V. Based on the C-V data of Fig. 8.4 and Equation (8.3), the thickness of the undoped layer (i-GaN) of the p-i-n junction is calculated for both as-grown and irradiated samples S1, and found to be 172 nm and 188 nm, respectively. These values agree well with the 200 nm i-GaN thickness of sample S1 given in Fig. 8.1.

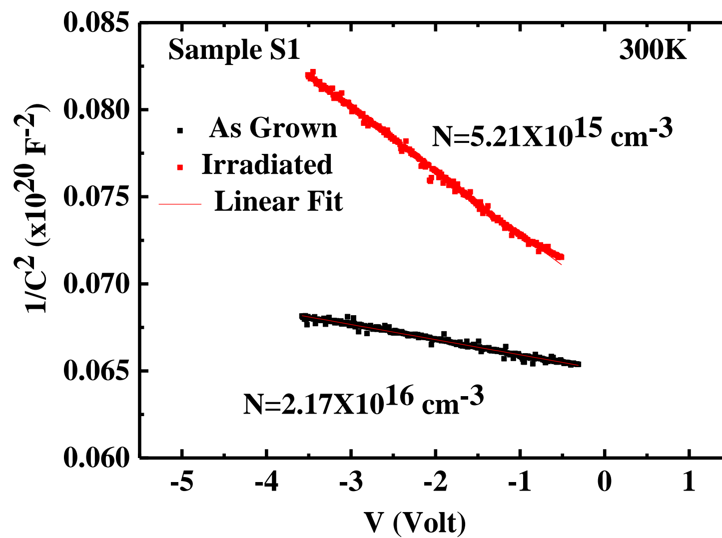

Fig. 8.5. Room temperature plot of $1/C^2$ as a function of reverse bias voltage for as-grown and irradiated S1 samples.

8.3.3 DLTS CHARACTERISTICS

In order to elaborate further on the role of beta particle irradiation on the electrically active defects in betavoltaic microbattery based on a GaN p–i–n homojunction, DLTS experiments [23] were carried out at basing conditions of a reverse bias, V_R = -0.5 V, with filling pulse height , V_P= 0 V, and a filling pulse duration, t_p =1 msec. Rate windows ranging from 5 to 2000 s^{-1} were used in these measurements. The samples were scanned from 10 K up to 450 K.

Fig. 8.6 shows the DLTS spectra at a rate window of 500 s^{-1}, before and after irradiation, for sample S2. From this spectra it can be seen that no minority trap is observed in these samples but two majority traps E_1 and E_2, and E_{1i} and E_{2i} are detected at temperatures 300 K and 400 K for as-grown and irradiated samples, respectively. Their activation energies, capture cross-sections, and concentrations were obtained from Arrhenius plots of ln (e/T^2) versus 1000/T as shown in Fig. 8.7 and are summarized in Table 6.1.

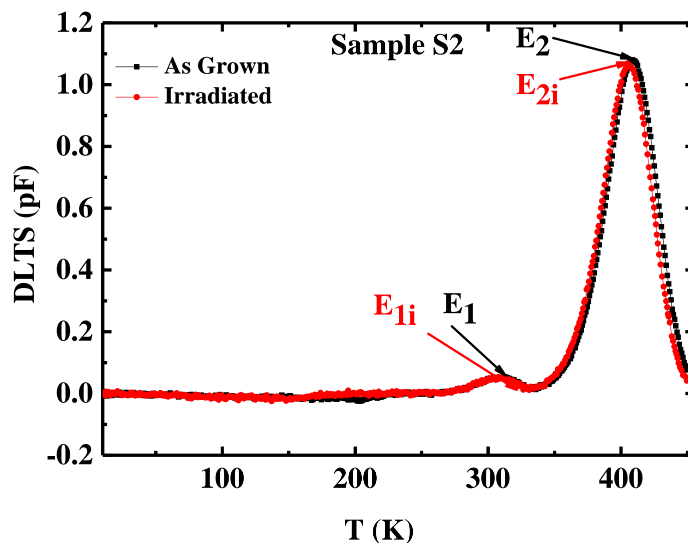

Fig. 8.6. DLTS spectra of as-grown and irradiated S2 samples obtained with reverse bias of -0.5V, V_p of 0V, filling pulse duration of 1 msec, and rate window of 500 s^{-1}.

In the case of sample S2, where the thickness of the undoped layer is 600nm, the i-region layer of the p-i-n junction is not completely depleted. Although this layer is not intentionally doped, it contains excess free electrons. Thus, the positive signal indicates that the peaks are correlated with the emission of majority carriers (electron traps).

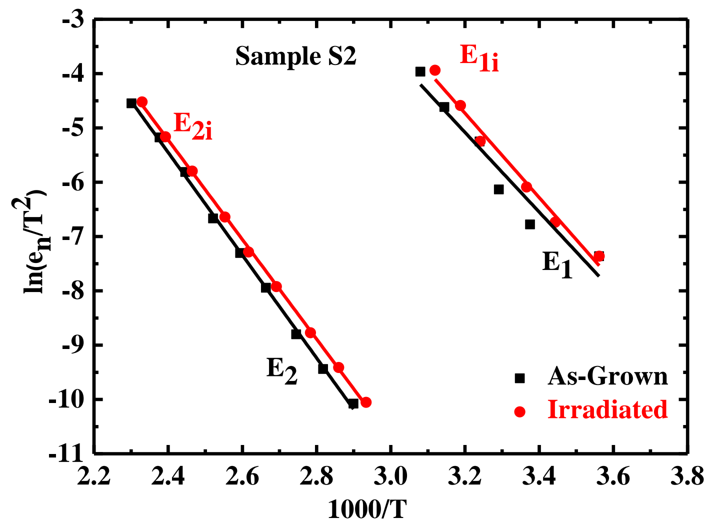

Fig. 8.7. Arrhenius plots of the electron traps depicted in Fig. 8.6 where the DLTS spectra were recorded for sample S2 with the following parameters: V_R =- 0.5 V, V_P = 0V and the duration of the filling pulse was t_p= 1ms at rate window 500 s^{-1}.

From the electrical parameters of the traps of as-grown and irradiated S2 samples, displayed in Table 8.1, one can conclude that the similar activation energies derived from these plots confirm that they correspond to the same defect level. In particular, it can be seen that the electron trap E_1 with thermal activation energy 0.63 eV in as-grown S2 sample is approximately the same as electron trap E_{1i} with thermal activation energy 0.66 eV recorded in the irradiated S2 sample, and has possibly the same origin. These traps have signatures very close to the traps

commonly observed in undoped and Si doped GaN. The origin of this deep level is not clear and remains controversial [24, 25]. Generally, authors ascribed the nature of this trap either to a single defect (vacancy) or to V_{Ga}–O_N complex [24-27]. Hasse *et al.* [28] have proposed that this level could be correlated to a native defect in GaN that is generated as a result of N implantation. Traps E_2 and E_{2i}, are comparable to the defect levels with activation energy of 0.76 eV reported by Asghar *et. al*. [26] and 0.78 eV reported by Auret *et al.* [29]. These defects were induced after the epitaxial n-GaN was irradiated by He ions with 5.4MeV. The nature of these defects is related to nitrogen-interstitials (N_i) formed as a result of the He-bombardment that creates a collisional cascade by displacement of nitrogen atoms from their original crystalline sites to interstitial position. In addition to that, these traps are also found in GaN grown under Ga-rich conditions [30] and not subjected to any irradiation. Above all, the observed traps E_2 and E_{2i} in the as-grown and irradiated samples which are identical in terms of activation energy (~ 0.8 eV) could tentatively be attributed to nitrogen-interstitial (N_i). Moreover, according to capture cross sections and concentrations values of traps detected in samples S2 shown in Table 8.1, one could infer that these traps are not modified by the relatively low energy irradiation used in our samples (0.54 MeV). Thus, there is weak effect of β-particle irradiation on S2 samples.

Table 8.1. Apparent activation energy, E_T, capture cross section, σ_n, and trap concentration of the defects, N_t, observed in S1 and S2 as-grown and irradiated samples. The DLTS experimental conditions were: V_R=-0.5V, V_P=0V, and t_p= 1msec.

Sample	Trap label	E_T (eV)	σ_n (cm^2)	N_t (cm^{-3})
As-grown S1	H_1	0.83 ± 0.07	7.29 x 10^{-15}	8.09 x 10^{14}
Irradiated S1	H_{1i}	0.89 ± 0.09	5.22 x 10^{-14}	2.25 x 10^{14}
As-grown S2	E_1	0.63 ± 0.02	1.47 x 10^{-13}	1.21 x 10^{14}
	E_2	0.81 ± 0.05	4.72 x 10^{-14}	2.82 x 10^{15}
Irradiated S2	E_{1i}	0.66 ± 0.08	8.13 x 10^{-13}	1.20 x 10^{14}
	E_{2i}	0.78 ± 0.09	2.95 x 10^{-14}	2.40 x 10^{15}

Fig. 8.8 displays DLTS spectra of as-grown and irradiated S1 samples using similar DLTS experimental conditions as for S2 samples. In fact, the DLTS measurements in these samples revealed the presence of one positive and one negative peak before and after irradiation. It is worth taking into consideration that, the positive signal does not seem to be affected by the irradiation, whereas the negative signal is clearly modified and shift to lower temperature after irradiation. The majority traps labelled H_1 and H_{1i} are detected at high temperature (~ 400 K). However, the minority E_3 and E_{3i} traps are detected at low temperature (~ 150 K). In the case of S1 samples, the i-region of the p-i-n junction is completely depleted at - 0.5 V. Therefore, the active depletion region studied here is mainly on the p-type side. Thus, the positive peaks in DLTS correspond to hole traps (majority carriers), while the negative peaks correspond to electron traps (minority carriers) in S1 samples.

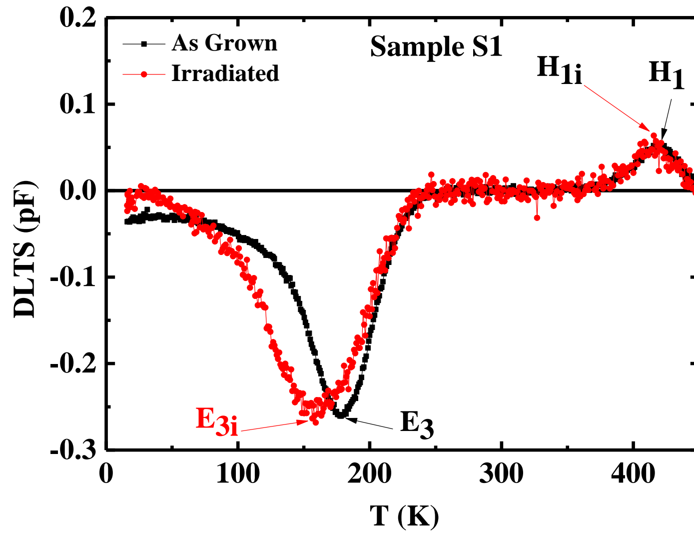

Fig. 8.8. DLTS spectra of as-grown and irradiated S1 samples obtained with reverse bias of -0.5V, V_p of 0V, t_p=*1 msec*, and rate window of 500 s^{-1}.

The hole traps activation energies, capture cross-sections, and concentrations were obtained from Arrhenius plots of ln (e/T^2) versus 1000/T as shown in Fig. 8.9 and summarized in Table 8.1.

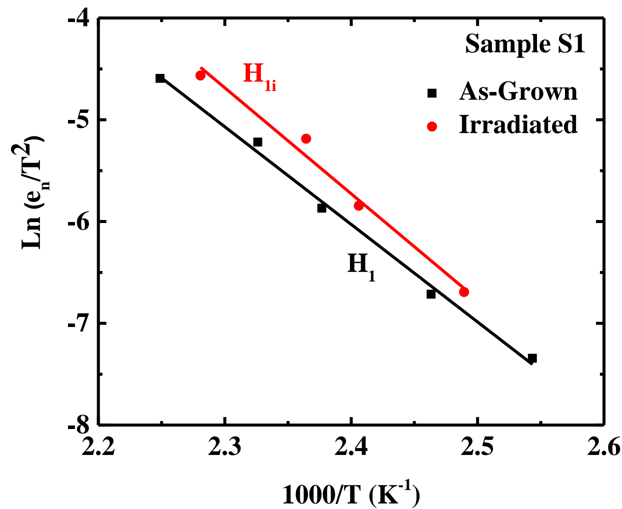

Fig. 8.9. Arrhenius plots of the hole traps depicted in Fig. 8.8 where the DLTS spectra were recorded for S1 samples with the following parameters: V_R =- 0.5 V, V_P = 0V, and filling pulse t_p= 1ms.

The hole traps of energy $H_1 \approx 0.83$ eV and $H_{1i} \approx 0.89$ eV are likely to correspond to the same trap reported by Emiroglu *et al.* [31] with energy of 0.87 eV. They assigned this trap to the $[V_{Ga}\text{-}(O_N)_3]$ complex which involves gallium vacancies and oxygen impurity atoms. After irradiation, the capture cross section of this hole trap increases about one order of magnitude. However, the concentration of this trap decreases about three times as a result of irradiation. Palmer *et al.* [32] stated that in order to displace gallium atoms, an electron beam energy higher than 0.7MeV is needed. In our study the samples were exposed to an electron beam energy of only 0.54 MeV. This amount of energy should not generate more gallium vacancies.

Regarding the negative peaks shown in Fig. 8.8 for both as-grown and irradiated samples, it can be clearly seen that these peaks are broad which is normally attributed to the existence of defect states spreading over a larger energy range [33]. Moreover, the Full Width at Half Maximum (FWHM) of these peaks are much larger than $0.1T_m$ (where T_m is the maximum peak intensity temperature) evidencing that multilevels are present rather than just a single defect [34]. The irradiated samples exhibit both a shift of the peak position and an increase of FWHM suggesting the creation of a defect with an activation energy very close to the one observed in the as-grown samples. Thus the characteristics of the defects E_3 and E_{3i} are difficult to determine. One way of avoiding this difficulty is to increase their signal to noise ratio by recording DLTS spectra with the lowest rate windows at different reverse biases. Normally the depletion region where trapping and de-trapping of charge carriers processes occur is controlled by applying different reverse biases. Fig. 8.10 displays DLTS spectra for irradiated S1 samples recorded with 200 s^{-1} at various reverse biases.

From Fig. 8.10, it can be seen that as the | V_R | increases, the DLTS signal starts to show the presence of additional peaks confirming the existence of more than a single electron level. Since the peaks are very broad and not well-defined, high resolution Laplace DLTS [31] measurements are needed in order to shed some light on the analysis of these peaks. At this stage, a range of activation energies is estimated from the DLTS envelopes (in Fig. 8.10), rather than from the peaks shown in Fig. 8.8. The levels appearing between this envelop are very likely located in the energy range 0.06 - 0.08 eV below the conduction band. This range of activation energies is commonly observed in n-GaN grown by MBE and MOCVD. Normally these levels correspond to N vacancies (V_N) [14, 35]. The theoretical study done by Van de Walle and Neugebauer [36] concluded that V_N is a shallow donor. After β-particle irradiation for S1 samples, other unknown defects are created with activation energies in the range mentioned above. These new defects seem to be specific to the p-side of the structure.

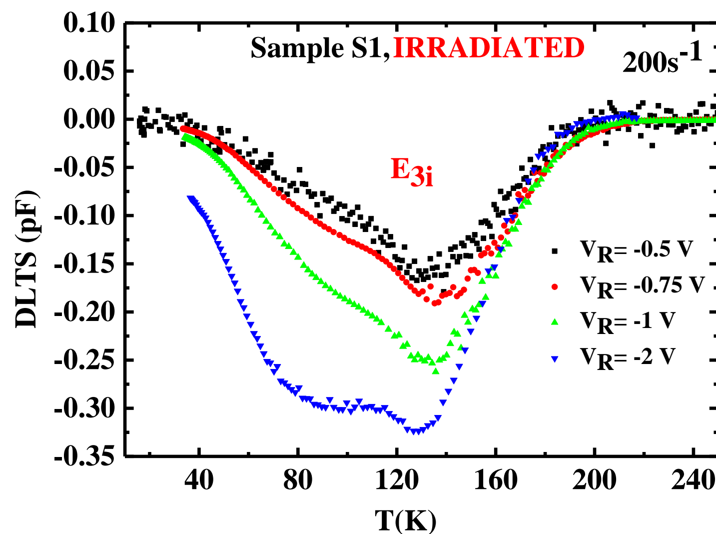

Fig. 8.10. DLTS spectra recorded for irradiated S1 samples with the following parameters: V_R= [-0.5 V; - 0.75 V; -1 V; - 2 V], V_P = 0 V, and duration of the filling pulse t_p= 1ms at rate window 200 s^{-1}.

8.4 CONCLUSION

In summary, the effect of 0.54 MeV electron irradiation is studied in GaN p-i-n diodes grown by MOVPE technique with the i-GaN region having thicknesses of 200 and 600 nm using I-V, C-V and DLTS measurement techniques. From the I-V characteristics, although the reverse current density did not change when the thickness of i-GaN region increases, the forward current density decreases. Additionally, the β-particles irradiation has no effect on the measured I-V parameters for the tested samples. The C-V measurement indicated that the samples with lower thickness (S1) are affected noticeably by irradiation due to the creation of defects which capture the free carriers. The main finding of DLTS study is that the irradiation of GaN has no effect on the deep electron traps with activation energies ranging from 0.6 to 0.8 eV and deep hole trap at 0.8 eV. However, the DLTS measurements for irradiated samples with thinner iGaN layer (S1 samples) have shown that new shallow donor traps are created with activation energies ranging from 0.06 to 0.08 eV distributed very closely to each other making their analysis difficult.

REFERENCES

[1] P. B. Koeneman, I. J. Busch-Vishniac and K. L. Wood, Journal of Microelectromechanical Systems **6** (4), 355 (1997).

[2] C. Chen, Y. Chang and J. Zhang, Micro Electro Mechanical Systems (MEMS), 2012 IEEE 25th International Conference, (2012).

[3] Z. Cheng, Z. Zhao, H. San and X. Chen, Nano/Micro Engineered and Molecular Systems (NEMS), 2011 IEEE International Conference (IEEE), 1036 (2011).

[4] P. Rappaport, Physical Review **93** (1), 246 (1954).

[5] H. Guo, H. Yang and Y. Zhang, Micro Electro Mechanical Systems, 2007. MEMS. IEEE 20th International Conference, (2007).

[6] R. Duggirala, S. Tin and A. Lai, TRANSDUCERS 2007-2007 International Solid-State Sensors, Actuators and Microsystems Conference, (2007).

[7] M. Chandrashekhar, C. I. Thomas, H. Li, M. G. Spencer and A. Lal, Materials Science Forum, (2006).

[8] C. Eiting, V. Krishnamoorthy, S. Rodgers, T. George, J. D. Robertson and J. Brockman, Applied Physics Letters **88** (6), 4101 (2006).

[9] W. Sun, N. P. Kherani, K. D. Hirschman, L. L. Gadeken and P. M. Fauchet, Advanced Materials **17** (10), 1230 (2005).

[10] V. Andreev, Polymers, Phosphors, and Voltaics for Radioisotope Microbatteries, 289 (2002).

[11] C. Zai-Jun, S. Hai-Sheng, C. Xu-Yuan, L. Bo and F. Zhi-Hong, Chinese Physics Letters **28** (7), 078401 (2011).

[12] S. Goodman, F. Auret, F. Koschnick, J.-M. Spaeth, B. Beaumont and P. Gibart, Materials Science and Engineering: B **71** (1), 100 (2000).

[13] M. Linde, S. Uftring, G. Watkins, V. Härle and F. Scholz, Physical Review B **55** (16), R10177 (1997).

[14] D. C. Look, D. Reynolds, J. W. Hemsky, J. Sizelove, R. Jones and R. J. Molnar, Physical Review Letters **79** (12), 2273 (1997).

[15] Z. Fang, D. C. Look, W. Kim, Z. Fan, A. Botchkarev and H. Morkoç, Applied Physics Letters **72** (18) (1998).

[16] D. Lang, Journal of Applied Physics **45** (7), 3023 (1974).

[17] C. Pernot, A. Hirano, H. Amano and I. Akasaki, Japanese Journal of Applied Physics **37** (10B), L1202 (1998).

[18] A. Osinsky, S. Gangopadhyay, R. Gaska, B. Williams, M. Khan, D. Kuksenkov and H. Temkin, Applied Physics Letters **71** (16), 2334 (1997).

[19] D. K. Schroder, *Semiconductor material and device characterization*. (John Wiley & Sons, 2006).

[20] J. H. Werner, Applied physics A **47** (3), 291 (1988).

[21] L. Dobaczewski, A. Peaker and K. B. Nielsen, Journal of Applied Physics **96** (9), 4689 (2004).

[22] S. M. Sze and K. K. Ng, *Physics of semiconductor devices*. (John Wiley & Sons, 2006).

[23] D. Lang, Journal of Applied Physics **45** (7), 3023 (1974).

[24] C. Wang, L. Yu, S. Lau, E. Yu, W. Kim, A. Botchkarev and H. Morkoç, Applied Physics Letters **72** (10) (1998).

[25] D. Bisi, M. Meneghini, C. De Santi, A. Chini, M. Dammann, P. Bruckner, M. Mikulla, G. Meneghesso and E. Zanoni, Electron Devices, IEEE Transactions on **60** (10), 3166 (2013).

[26] M. Asghar, P. Muret, B. Beaumont and P. Gibart, Materials Science and Engineering: B **113** (3), 248 (2004).

[27] P. Hacke, T. Detchprohm, K. Hiramatsu, N. Sawaki, K. Tadatomo and K. Miyake, Journal of Applied Physics **76** (1), 304 (1994).

[28] D. Haase, M. Schmid, W. Kürner, A. Dörnen, V. Härle, F. Scholz, M. Burkard and H. Schweizer, Applied Physics Letters **69** (17), 2525 (1996).

[29] F. Auret, S. Goodman, F. Koschnick, J.-M. Spaeth, B. Beaumont and P. Gibart, Applied Physics Letters **73**, 3745 (1998).

[30] M. A. Reshchikov and H. Morkoc, Journal of Applied Physics **97** (6), 061301 (2005).

[31] D. Emiroglu, J. Evans-Freeman, M. Kappers, C. McAleese and C. Humphreys, physica status solidi (c) **5** (6), 1482 (2008).

[32] D. Palmer, *Electronic energy levels in group-III nitrides*. (2011).

[33] D. Cavalcoli, A. Cavallini and E. Gombia, Physical Review B **56** (16), 10208 (1997).

[34] R. Kaplar, S. Ringel, S. R. Kurtz, J. Klem and A. Allerman, Applied Physics Letters **80** (25), 4777 (2002).

[35] L. Polenta, Z. Fang and D. C. Look, Applied Physics Letters **76** (15), 2086 (2000).

[36] J. Neugebauer and C. G. Van de Walle, Physical Review B **50** (11), 8067 (1994).

CHAPTER 9: CONCLUSION AND FUTURE WORK

This chapter summarises the research work carried out on the electrical active defects present in a variety of advanced semiconductor systems and devices, namely, GaAs-based intermediate band solar cells, GaAsN epilayers, and GaN-based betavoltaic microbattery. I-V, C-V, DLTS and Laplace DLTS characterization techniques were used to investigate these heterostructures. Future work suggestions also are covered in this chapter.

9.1 CONCLUSION

The existence of defects in a set of (311)A GaAs solar cell structures grown by MBE namely p-n (labelled PN, first reference sample), p-i-n (labelled PIN, second reference), undoped p-i-n with InGaAs quantum wires (labelled QWR undoped) and Si δ- doped p-i-n with InGaAs quantum wires (labelled QWR doped) have been investigated. In addition, trap states affecting the solar cell performance were probed by DLTS and Laplace DLTS. These measurements demonstrated a reasonable correlation with the efficiency and external quantum efficiency characteristics of the solar cells at different temperatures obtained by Kunets *et al.* [1], since they showed that the trap peaks are at almost the same temperature ranges where the efficiency and EQE characteristics changed as a function of temperature.

Also in this thesis, the effect of gamma (γ-) irradiation on MBE grown dilute GaAsN epilayers containing nitrogen concentration in the range 0.2 – 1.2% have been studied. After irradiation DLTS measurements indicated that the number of traps either decreased, eradicated, remained constant, or new traps were created depending on the concentration of nitrogen. Furthermore, this investigation showed that the irradiation effect was more noticeable in the samples with nitrogen concentration of 0.2 and 0.4%. In addition, I-V, C-V and DLTS measurement techniques were used to investigate the effect of beta (β-) particle irradiation on the electrical

properties of betavoltaic microbatteries based on a GaN p–i–n homojunction with the undoped layer (i-GaN) having thicknesses of 200 nm and 600 nm. This study showed a noticeable effect of irradiation on the samples with lower thickness and was correlated to the creation of new defects. Overall, the results of this study showed that the defects affected significantly the electrical properties of different advanced semiconductor structures and devices.

9.2 FUTURE WORK SUGGESTIONS

According to the experimental results obtained in this thesis work, suggestions for further investigations are proposed in the following:

(i) In order to understand further the effects of δ- doping in InGaAs QWr IBSCs based nanostructures and as well as to study the IR-induced transition and capture processes, it would be more promising to fabricate and investigate this structure with various δ- dopants levels. Thus this will help determine the best δ- dopants levels for the enhancement of the efficiency of QWr IBSCs.

(ii) In case of γ-irradiated dilute GaAsN samples it will be worth to carry out a systematic study to investigate the effect of thermal annealing. This heat treatment process is well known to reduce the concentration of defects and/or annihilate completely defects. Therefore the electrical, optical and structural properties of the materials and devices will be improved.

(iii) ^{63}Ni could be a very interesting irradiation source to irradiate GaN samples. In view of device applications, a long term stability will be reached with the use of ^{63}Ni irradiation source which is more suitable to betavoltaic applications, owing to its relatively benign radiation of 0.017 MeV and its long half-life of 100 years. It is worth pointing out that the reason behind the use of lower-energy of beta emitting materials is to minimize long-term damage to the energy collection device.

(iv) For the InGaAs QWr IBSCs and GaN betavoltaic microbattery p-i-n structures, it is worth performing further studies on simpler test structures such as Schottky diodes and p-n junctions, which provide easier identification of defects. Also this analysis will help to improve the quality of the material and understand the role of deep states on the performance of future devices based on these material systems.

(v) Development of a new physical model to analyse the devices with fairly high ideality factors.

REFERENCES

[1] V. P. Kunets, C. Furrow, M. Ware, L. de Souza, M. Benamara, M. Mortazavi and G. Salamo, Journal of Applied Physics **116** (8), 083102 (2014).